Ultrasound Imaging without Gel for Clinical Application

A Major Qualifying Project

Submitted to the faculty of
WORCESTER POLYTECHNIC INSTITUTE
in partial fulfillment of the requirements for the
Degree of Bachelor of Science

By:

Bilguun Duulal

Kyla Egenberger

Mary Rego

Julisse Sabater

Advisors: Professor Lammert (WPI), Professor Zhang (WPI)
Sponsor: Dr. Robert Meislin (NYU Langone Health)

Completed on:
Thursday, May 6th, 2021

ABSTRACT

Ultrasound (US) imaging is a diverse technology that can visualize internal structures through the propagation and reflection of high frequency US waves. This project functioned to produce a method for US imaging that would operate without the use of conventional topical gel for clinical application. The project was inspired by National Aeronautics and Space Administration's aeronautical application of a floating point US transducer (U.S. Patent No. 9,354,206 in 2016). The system consisted of a Clarius linear array US transducer attached to a ball screw linear actuator. The actuator allowed the US transducer to tap on the surface being imaged to reduce the friction associated with gliding across a gel-free surface. Actuation of the US transducer was at a frequency of either 6 or 14 Hz, where one "cycle" consisted of lifting by 0.5 mm and then lowering by 0.5 mm. To replace topical gel, several solid materials were considered: nitrile rubber, neoprene, polydimethylsiloxane (PDMS), and PDMS with titanium dioxide. Image quality was quantitatively assessed with signal processing metrics (mean squared error, peak signal to noise ratio, and structural similarity index) and statistical analysis (Wilcoxon Rank Sum test, Kruskall Wallis test, and Pairwise Comparison). From the results, it was determined that PDMS (with no titanium dioxide) was the most promising replacement for gel, as it showed the best image quality compared to the other materials. The effectiveness of PDMS in US was the most significant when imaging without gel and without the actuation mechanism. Lastly, it was lastly found that actuation did not have significant effects on image quality in this experimental configuration.

EXECUTIVE SUMMARY

Throughout the academic year, the team ideated, prototyped, developed, and tested a clinical ultrasound (US) imaging system that could operate without conventional topical gel. The project was inspired by a National Aeronautics and Space Administration (NASA) patent invented by Zalameda and Johnson (2016), titled "Floating Point US Transducer". While US imaging is vital to detect microfractures in aerospace applications, the conventional gel would erode the materials being imaged, thus leading to a need for a gel-free system. The mechanism for this system focused primarily on oscillating the US probe vertically to reduce frictional forces associated with gliding the probe across a gel-free surface in a single motion. While NASA's system was found to be effective within its aerospace and industrial setting, our team was tasked to translate such technology to a biomedical and clinical setting.

The development of a gel-free US system for clinical application began with an extensive literature review. Topics of interest included the physics and electronics of US, alternative imaging techniques, alternatives to US gels/mediums, electrical components to produce linear motion (i.e., actuators), image quality, and signal processing. One research finding most significant to the success of the project was regarding acoustic impedance, which is a material's resistance to an US wave. In order to achieve a quality image that can accurately represent the internal structures, the acoustic properties of the materials in which the wave passes through should be similar. For example, the acoustic impedance of air is drastically different from that of tissues, so taking an image of the skin when there is air between the skin and the probe would provide a very low-quality image—nothing would be visible. Therefore, to achieve a gel-free US imaging system, air barriers should be eliminated, and the acoustic impedance of tissues should be considered.

Once adequate background was obtained, the team began to ideate several design concepts to fulfil the input requirements and satisfy the client statement. During the preliminary design process, methods for testing were determined in a way that aligns with a "fail fast" methodology that encourages incremental developments and frequent experimentation to provide a positive feedback loop for the design process. Four designs were ideated, and an analysis of the input requirements concluded with one design to proceed with. The design iteration selected consisted of three major components: a solid couplant to replace US gel, an electrical system to oscillate the US transducer with 3D-printed components to hold it together, and a method of signal processing to quantify image quality.

To replace US gel, nitrile rubber (MATNIKS Rubber), neoprene rubber (MATNIKS Rubber), and polydimethylsiloxane (PDMS) (Sigma-Aldrich) were considered. The neoprene and nitrile rubber materials were purchased, while the PDMS samples were manufactured by the team in a laboratory setting. A study done by Guillermic, Lanoy, and Strybulevych (2019) found that PDMS mixed with titanium dioxide (TiO_2) particles was an effective medium for underwater US imaging, as submersion into water would be an environment where US gel would not be feasible. The particles act as structures for US waves to reflect from, increasing acoustic impedance as the wave attenuates; less of the US wave successfully propagates through the material. With the consideration of this research, TiO_2 particles (Fisher Scientific) were purchased and incorporated into PDMS samples during the manufacturing process, with the goal of refining acoustic properties. The elastomer base used was the Sigma-Aldrich Sylgard 184, which solidifies with the addition of a curing agent. All samples were cured at a ratio of 1:20 for the curing agent. The

finalized PDMS-TiO$_2$ samples were 25 mL in total volume and had TiO$_2$ concentrations of 0%, 1.0%, 3.0%, 5.0%, 7.5%, 10.0%, 12.5% 15.0%, 17.5%, 20.0%, 22.5%, and 25.0% TiO$_2$ (by total volume).

As for the electrical components, the materials used were a Ball Screw Linear Stage Actuator with a Nema23 Stepper Motor (RATTM Motor), 3 kg Load Cell (Calt), HX711 Load Cell Amplifier (SparkFun), TB6560 Stepper Motor Driver Board (HiLetgo), and an Arduino UNO Rev3 microcontroller board (Arduino). The mechanism for the actuator is characterized by the turning of a screw via the Nema23 Stepper Motor, which would displace a small black box fixed to the screw. Once all the necessary electrical connections were made, codes were written in the Arduino software to control the Arduino UNO board. The main function of the code was to rotate the screw on the actuator at varying accelerations, quickly switching directions, to produce a vertical oscillation motion of the small box fixed to the screw. The US transducer was attached to this box through 3D printed parts so that it could move vertically with the rotation of the screw, where one full rotation would correspond to 5 mm displacement. By inputting a value for acceleration into the code, the "sonic" frequency of the tapping was able to be controlled. The maximum frequency achieved was 14 Hz, where one "cycle" consisted of the probe raising 0.5 mm and then lowering 0.5 mm. In addition to the oscillation mechanism, the load cell was incorporated to read the forces the US transducer exerted on the sample being imaged.

Signal processing methods and quantitative analysis was performed in the program MATLAB, to determine image quality for all experimental testing. Code was written to vectorize images, calculate metrics, and perform statistical analysis on the data. All images were first vectorized into a new matrix, in which each row corresponds to each image in the dataset. Once the images were vectorized, the following metrics were calculated: mean squared error (MSE), peak signal to noise ratio (PSNR), and the structural similarity index (SSIM). The means and standard deviations of each metric were calculated as well. To draw conclusions from the data, conditions were then compared using statistical analysis. First, a Wilcoxon Rank Sum Test was performed. The Wilcoxon Rank Sum Test compared each experimental condition to the "with gel" reference condition. This comparison was made due to the "with gel" condition being the experimental equivalent to medical US imaging. The next test performed was a Kruskall Wallis test, which is a multiple comparison test. It compared experimental conditions of interest to each other to determine if they came from the same distribution. This test also produced a box plot to visually represent the results of the test. The last test performed was a Pairwise Comparison. This allowed for the conditions of interest to be directly compared, which produced metrics and visual plots to show the conditions' comparability.

Experimental testing for the project occurred in three phases. The First Experimentation Phase utilized an alternative US imaging system since ours had not been fully designed by that point. This system was a pneumatic actuated US transducer device built by Dhirajsinh Deshmukh, a WPI Master's Student in Robotics Engineering, advised by Professor Zhang. During this phase, a CIRS Thyroid US Training Phantom was imaged both with and without gel, to test the signal processing code and provide quantitative proof that a gel-free condition was of worse quality compared to one with gel. The testing procedure was then improved so that *With Gel Versus Without Gel* testing could occur, where final conclusions were later drawn. The *With Gel Versus Without Gel* testing imaged the CIRS General Purpose US Phantom at a depth of 7 cm. This phantom had five gray scale targets, which appeared in quality US images as small circles of

varying darkness organized horizontally. The result of this testing was a positive control image (with gel; best quality) and a negative control image (without gel; worst quality), which provided the bounds for image quality.

In the Second Experimentation Phase, Dhirajsinh Deshmukh's system was used once more to perform *Material* testing. Neoprene, nitrile rubber, PDMS, and all the TiO_2-PDMS samples were imaged. The experimental set-up for the *Material* testing consisted of the couplant material lying flat on the CIRS General Purpose US Phantom with gel above and below it. The aim of the gel was to isolate acoustic properties of the material alone, without any air interference. The US transducer was lowered to exert 5 N of force then images were taken, processed, and analyzed. The images taken with the TiO_2-PDMS samples were worse image quality than originally hypothesized. This resulted in the team manufacturing additional PDMS samples with lower concentration of TiO_2. The new samples were imaged and analyzed using the same process as the initial phase of *Material* testing.

For the third and final phase of testing, the final experimental system was completed and utilized. This phase was *Frequency* testing. In this phase a large amount of the project's final results was obtained. The experimental system consisted of the Clarius linear array US transducer attached to the shaft of the linear stage ball screw actuator through 3D printed parts (designed in CAD by Dhirajsinh Deshmukh). The actuator was fixed to a chemistry ring stand by clamps and set on a tabletop. This allowed the system to remain stationary and ensured that the US transducer remained perpendicular in orientation to the sample being imaged. PDMS without TiO_2 was used as the couplant in this testing, which laid flat on top of the CIRS General Purpose US Phantom. The actuator lowered the US transducer until 5 N was applied to the PDMS/phantom. Then, the system would oscillate by 0.5 mm at a frequency of either 0 Hz (no actuation; constant 5 N force), 6 Hz, or 14 Hz. In addition to these three frequencies, other experimental conditions included, *with gel versus without gel* and *PDMS versus no PDMS*. The twelve experimental trials are as follows:

1. No PDMS, gel **(positive control)**
2. No PDMS, no gel **(negative control)**
3. PDMS, gel
4. PDMS, no gel
5. No PDMS, no gel, 6 Hz actuation
6. No PDMS, gel, 6 Hz actuation
7. PDMS, no gel, 6 Hz actuation
8. PDMS, gel, 6 Hz actuation
9. No PDMS, no gel, 14 Hz actuation
10. No PDMS, gel, 14 Hz actuation
11. PDMS, no gel, 14 Hz actuation
12. PDMS, gel, 14 Hz actuation

In order to generate results and draw conclusions, images from *With Gel Versus Without Gel* testing, *Material* testing, and *Frequency* testing were processed and analyzed using the signal processing and statistical methods mentioned previously. After image processing and statistical analysis was completed, significant conclusions were drawn from quantitative and qualitative results. *Material* testing was performed with the aim of finding a dry couplant to replace topical

gel. Through *Material* testing, all findings concluded that there was a large difference between all materials. As a dry couplant, PDMS was found to be a viable replacement for topical gel. It was also found that PDMS with TiO_2 hindered image quality. The following test performed was *Frequency* testing to determine the effect of actuation on image quality. Out of the two frequencies tested, 6 and 14 Hz, actuation at 6 Hz was found to be better. However, it was found that actuation did not have a significant impact on image quality. This is shown by the result of the best overall experimental condition being *0% TiO_2 PDMS without gel or actuation.* It was also found through frequency testing that the use of gel in any experimental condition where the dry couplant of PDMS was present impeded image quality. Additional to *Material* and *Frequency* testing, the homogeneity of TiO_2 in the PDMS samples created was tested. This was done by imaging varying regions of the 7.5% TiO_2 PDMS sample and comparing the respective image qualities. It was found that homogeneity was not an issue due to all regions having comparable quality. However, this is still a factor that could be further explored in future experimentation.

It should be noted that all testing occurred with the fixed system previously described. While the actuator displaced the transducer vertically, all lateral motion was inhibited by fixing the system to a ring stand stationary on a tabletop. In a clinical setting, the physician might need to move the transducer across the skin being imaged to visualize a large surface area. Therefore, to be considered for clinical application, this project would need several design adjustments/ further developments. First, the system should be made more compact and lightweight. Secondly, the Arduino code should be written in a manner so that lateral movement does not need to be constant. For example, if a physician is operating the system, they might exert force on the skin, in addition to the force exerted by the actuator mechanism. Therefore, this code should have a continuous feedback loop so that it will continuously correct added forces from the human operator so that a constant force is achieved at every instant. Lastly, attaching the PDMS directly to the probe would be a desirable next step in the design process. It could be a nuisance for the physician to move the PDMS every time they want to image a different spot on the skin. Attaching it to the transducer would eliminate this step along with making it a more commercially advertised product.

AUTHORSHIP PAGE

The following report was written by the entire team—Bilguun Duulal, Kyla Egenberger, Mary Rego, and Julisse Sabater—with equal contribution from each team member. Each member had equal contribution through the entirety of the project and was able to come together to produce the research that is presented in this report.

ACKNOWLEDGEMENTS

TABLE OF CONTENTS

LIST OF EQUATIONS

LIST OF FIGURES

LIST OF TABLES

1.0 INTRODUCTION

US imaging is a diverse technology to view the internal structures within an object, and it is utilized in a variety of settings. This project explored methods for US imaging without the conventional gel typically applied to the surface being imaged. The U.S. Patent No. 9,354,206 Floating Point US Transducer (Zalameda & Johnston, 2016) that inspired this project explored aerospace applications, which led the team to pursue methods for clinical application. This section details the objective of this project as well as the inspiration from NASA.

1.1 Objective

US imaging is a useful tool in the medical field to view the internal structures of the body through the transmittance, reflection, and reception of an ultr wave against a surface being imaged. If there is an air barrier between the US transducer and the body's tissues, the US wave will reflect from the air instead of traversing through the body. This is caused by a dramatic difference in the acoustic properties between air and the tissues, ultimately preventing a quality image from being taken. Therefore, in order to get a clear image without artifacts, US gel is used to fill the air interface between the transducer and the surface being imaged. While it is evident that US gel is key for quality images, there are several benefits from a gel-free system. For example, gel may be uncomfortable for the patient; in ocular US, an intermediate material is needed to reduce the irritation associated with gel applied to the eyeball. In addition, low-income, low-resource areas might benefit from an all-encompassing device that does not necessitate a continuous supply of gel. The topical gel must also be cleaned from the surface of the skin and may cause issues regarding safety and sterilization, especially when invasive procedures are performed after imaging. Ultimately, the potential benefits of a gel-free US system indicate such as a promising area of research.

1.2 Project Inspiration

The goal of the NASA Floating Point US Transducer is to image objects without having to use a couplant or medium such as water or gel, simplifying imaging for vertical or overhead surfaces. Examples of surfaces that are used by NASA include parts that have surface roughness, such as a pipe. As stated by NASA, "Applications include material inspections that cannot be contaminated, in-situ composite structure inspections, structures in space (zero gravity), parts with special coatings, or medical" (NASA Langley's Technology Gateway, 2014). NASA further breaks down the applications of its device into five categories: aerospace, aviation, automotive, oil, and soft tissues. It should be noted that the fifth category was not the primary focus of NASA's system—rather, it was proposed more so for future applications, thus leading to this project.

While NASA uses the gel-free US system primarily on aerospace parts, this project focuses on US imaging of the human body for diagnosis and therapeutic purposes. Currently, their device is stationary as opposed to being handheld device for a clinical setting. However, NASA plans on creating a handheld version of their device for their applications instead of mechanical scanning in the future. If this technology is to be used for medical ultrasonic imaging, a handheld device would be ideal for ease of use of both the patient and the individual administrating the ultrasonic technology. Such input requirements for the gel-free US system to be used in a clinical setting led to the creation of this project.

2.0 LITERATURE REVIEW

There are many components that go into the development of an US system. This chapter will outline the fundamental principles relevant to a gel-free US project. The topics covered include alternative imaging techniques, the logistics of an US system, the functionality of an US couplant, how the imaging of an US system functions, and the logistics of the actuator system.

2.1 Overview of Ultrasound

US (US) is a term that represents sound above the frequencies heard by humans, which is about 20 kHz. US technology can be performed with two techniques: transmission and reflection. However, transmission is no longer in practice, resulting in reflection being the current medical US imaging technique. This imaging technique is made possible due to the piezoelectric effect located within the transducer, which produces a sound wave in electrical pulses at a desired frequency within the range of 2 to 18 MHz. The transmitted pulses create echoes within the body, where the sound waves reflect between tissue boundaries. This reflection occurs due to the different acoustic impedances of the bodily tissues. An acoustic impedance refers to how a medium opposes acoustic flow through it.

The quality of the image will depend on several factors such as sound wave focus and transducer selection. The sound wave focus can be affected by the acoustic lens, transducer shape, and control pulses from the machine (Carovac, Smajlovic, and Junuzovic, 2011). The selection of transducer type is dependent on the imaging's intended application. For example, a convex array transducer may be more suitable for observing guiding needle injections while a linear array transducer would be more suitable for observing tumors. This leads to the number of different applications that US technology can be used for. For example, it can be used to identify the exact site a needle should be injected for therapeutic purposes, find abnormalities within the body for diagnostic purposes, and view different anatomical structures (Berry, n.d.).

2.2 Imaging Alternatives

Imaging a patient is a vital step in the medical diagnosis process. Imaging allows for a physician to obtain additional information pertaining to a patient's condition beyond what an initial assessment can provide. The type of imaging technology used on a patient is one that is taken into great consideration. Some factors considered are location of interest, patient condition, patient physiology, desired information to be acquired, cost, and radiation exposure. Three common forms of imaging used within medical diagnostics are Ultrasonography (US), Computed Tomography (CT), Magnetic Resonance Imaging (MRI) (Brenner, 2007). Each form of imaging has advantages and disadvantages, and it is up to the physician to decide what the best course of action is.

The first form of imaging that will be discussed is CT, which is used for diagnostic purposes and the observation of asymptomatic patients. CTs are most commonly used for the imaging of bones, masses, and joints (Brendel, 2002). Spiral Computed Tomography images are a wonderful tool because they allow for a three-dimensional (3D) image to be produced of the imaged area. It requires taking several different X-rays at different angles to produce a high-quality image within seconds. For these unique diagnostic reasons, the use of CTs has and continues to increase in the medical community. Moreover, the New England Journal of Medicine published a study titled "Computed Tomography — An Increasing Source of Radiation Exposure",

highlighting why CTs are widely used for imaging and the potential hazards of their radiation exposure. Patient radiation exposure is dictated by a number of factors including: "the number of scans, the tube current and scanning time..., the size of the patient, the axial scan range, the scan pitch (the degree of overlap between adjacent CT slices), the tube voltage..., and the specific design of the scanner being used" (Brenner, 2007). However, the largest factor is the threshold for noise that the radiologist and radiology technician think are acceptable within the image.

Noise affects the clarity of the CT image, and higher radiation must be used to achieve less noise. The average range of radiation exposure dosage for a single CT is 15 mSV (for an adult) to 30 mSV (for an infant) (Brenner, 2007). It has been shown that exposure to ionization radiation from a single abdominal or chest CT may be associated with a higher risk of DNA damage and cancer formation. Typical abdominal CT exposure has a dose of 10-20 mSv (Martin & Semelka, 2006). It is important to highlight with these levels in mind, that the average person normally receives two to three scans per study. This puts the patient at a higher risk of radiation-induced carcinogenesis, meaning cancer cell development due to radiation. Therefore, the necessity of a CT should be considered before exposing a patient to radiation (Brenner, 2007).

An MRI is another imaging technique that utilizes radiation. Compared to a traditional CT, MRIs allow for multi-planar and volumetric imaging with better definition of soft tissue, generating in-depth physiological and biochemical information. It is also a great tool for radiotherapy (Khoo, 1997). MRIs function by specific atomic nuclei absorbing and emitting radio frequency (RF) energy when present in an external magnetic field, with strengths ranging from 0.2 Tesla to 9 Tesla. Pulses of RF at different parameters are applied to the area of interest to obtain quality contrasted images. The type of pulses produced and their subsequent sequence are carefully chosen to produce the best image quality with the minimal artifacts (Indik et al., 2017). MRIs are commonly used for imaging regions such as the brain due to their sensitivity to variance in tissue relaxation time. MRIs do not image bones well, due to them not having strong electron density information.

A direct comparison between the MRI and CT can be seen when imaging the spine. The MRI would provide a great image of affected areas in the posterior fossa, brainstem, and spinal cord. However, it will not depict any of the cortical bone well. The CT would intensely depict the cortical bone, but any soft tissue would appear in poor quality, producing artifacts within the image (Khoo, 1997). With the benefits of an MRI image highlighted, it is also important to state that the same risks associated with CTs also apply to MRIs—the patients will be exposed to radiation on several occasions in the diagnostic process since multiple MRIs are likely to be needed. Another potential hazard of MRIs comes with their increased availability leading to an increase in potential population exposure to Electric and Magnetic Fields (EMF), which can have genotoxic effects due to micronuclei induction. Within an MRI, there are three MFs produced to obtain 3D images; the contrast of MRI images comes from the varying magnetic properties within a person's physiology and biological tissue. The MF fields that are produced by an MRI do not only impact the patient; it also affects the people who may be present in the environment. While there are no confirmed conclusions as to whether the risk is large enough to not use the technology, these risks are important to consider when choosing the best technique of imaging for a patient (Hartwig, 2009).

In addition to CTs and MRIs, US (US) imaging is one of the most common modes of imaging. USs are both low cost, very fast (relative to other imaging techniques), and show a highly-detailed, geometrically-accurate image to the first order. These images are ideal for showing the

mechanical structures within the body. The US technology propagates high frequency waves through the body, where the waves can either continue to travel or they can be reflected. This fate of the US wave is determined based on the varying acoustic properties of the different bodily structures based on their density and elasticity. The heart is an example of an organ that is ideal to image with an US. Not only are US scans both efficient and low cost, but they also lack the negative cumulative biological side effects to the degree that CTs and MRIs do. Furthermore, the logistics of an US system are discussed in the following sections.

2.3 Ultrasound System

US technology can generate two-dimensional (2D) and three-dimensional (3D) images of internal structures due to the piezoelectric effect, where US waves are transmitted and then reflected back to the transducer as echoes. The US machine is a complex system that has a central processing unit (CPU), transducer pulse controls, display, keyboard/cursor, disk storage device, printer, and a transducer probe (Craig, n.d.). The transducer used for the probe of the device could affect the type of image result. For example, a 1D array transducer produces a 2D image while a mechanical wobbling transducer produces 3D images (Lee & Roh, 2017). The 1D array contains the following components: backing block, kerf, signal flexible printed circuit board, active layer, ground sheet, first and second matching layer, and an acoustic lens (Lee & Roh, 2017).

Each of the components play an important role in transmitting and receiving signals from the target. The purpose of the backing block is to take in the wave coming back from the target, which was originally caused by the piezoelectric effect from the active layer (Lee & Roh, 2017). In order to avoid noise, the backing block should have high attenuation (Lee & Roh, 2017). The active layer consisting of piezoelectric material produces the piezoelectric effect by generating a wave towards the desired target by an elec trical signal and receiving the reflected wave from the target by turning it into an electrical signal (Lee & Roh, 2017). Most transducers that use piezoelectric technology use ceramic as the material (Carovac et al., 2011). To protect transducer performance, a kerf is in place to isolate the elements and avoid crosstalk (Lee & Roh, 2017). The acoustic lens assists the transducer in focusing the US beam to the desired target while protecting it from external elements (Lee & Roh, 2017). Based on the type of transducer and whether the purpose is for 2D or 3D imaging, the components used may vary.

2.4 Ultrasound Couplant

Consideration of acoustic properties is vital to ensure an US image is representative of the actual structures being imaged and prevent artifacts (unrepresentative portions of the US image). Consequently, the medium between the US transducer and the sample being imaged (called the couplant) should have ideal acoustic properties. In the sections below, the physics guiding the efficiency of a couplant as well as examples of materials that operate as alternative couplants to topical US gel are discussed.

2.4.1 Physics of Couplants

US waves are a type of mechanical waves, meaning they require a medium for the wave to propagate through. The US transducer transmits US waves to a medium and then receives any parts of the wave that are reflected off of the medium. Boundaries between different types of tissues, such as between muscle and bone, disrupt the US beam and reflect the waves back to the

transducer as echoes (NIH, 2016). Other signals may be scattered by tissue irregularities. Furthermore, the cross-sectional images acquired are combined to then generate 2D and 3D images of the part of the body that was imaged. The transducer calculates the distance between the transducer and the medium at different points of image acquiring, which could then be pieced together to form complete images with accurate scaling. This is done by using the speed of sound and the time it took the signal to be transmitted then reaching the medium, as indicated in **Equation 1** below.

$$d = v*t$$

Equation 1: Distance (where d is the distance between the transducer and medium and v is the speed of sound in the medium)

As the US wave propagates through a tissue, the amplitude decreases as the distance increases. Portions of the waves are reflected or scattered at the different tissue interfaces, while others experience absorption, where the acoustic energy converts to thermal energy that is too miniscule to produce a significant change in temperature. Attenuation, typically measured in decibels per centimeter, can be characterized by the attenuation coefficient, which are standard values reported for different materials. **Equation 2** below demonstrates how attenuation can be calculated (Zagzebski, 1996).

$$\text{Attenuation (dB)} = \alpha \times d$$

Equation 2: Attenuation (where α is the attenuation coefficient (dB/cm) and d is the distance travelled (cm))

US couplants (e.g. gel and other gel-like mediums) are necessary to fill the air interface between the US probe and the surface being imaged to produce higher quality images with less artifacts. When there is a large change in acoustic impedance, Z, between two different mediums, the US wave reflects to the transducer as an echo rather than fully propagating through the body. This acoustic impedance indicates the "resistance an US beam encounters as it passes through a tissue." Acoustic impedance is proportional to the density of a material, where denser materials resist US waves more readily, as indicated in **Equation 3** (Murphy & Morgan, n.d.).

$$\text{Acoustic Impedance, } Z = \rho * v$$

Equation 3: Acoustic Impedance (where ρ is the density of the medium and v is the speed of sound) (Murphy & Morgan, n.d.)

Mediums that produce a large change in acoustic impedance when soft tissues are being imaged include dense materials, air ($Z = 0.0004 \times 10^6$ kg/(m²s)), and bone ($Z = 7.8 \times 10^6$ kg/(m²s)). Since the acoustic impedance of fat is 1.34×10^6 kg/(m²s), it is evident that the acoustic impedance of dense materials, air, and bone varies greatly from that of fat. Consequently, the change in acoustic impedance would be large; these three types of mediums are more echogenic relative to fat, meaning they have a greater ability to reflect US waves. Echogenicity is determined by the reflection fraction, where larger reflection fractions would be undesirable in US imaging, noted in **Equation 4** on the next page (Murphy & Morgan, n.d.).

$$\text{Reflection Fraction} = [(Z_2 - Z_1)/(Z_2+Z_1)]^2$$

Equation 4*: Reflection Fraction (where Z_1 corresponds to the first tissue's acoustic impedance and Z_2 corresponds to the second tissue's acoustic impedance)* (Murphy & Morgan, n.d.)

Without gel, the US waves would reflect off of the air instead of the desired surface, as the reflection fraction between the air and the tissue would be very large (Animal US Association, n.d.). Therefore, it is important to use a gel that has an acoustic impedance close in magnitude to either the surface being imaged, such as the skin. The "acoustic mismatch", characterized by the reflection fraction, between a soft tissue and a gelled transducer is so small that the US wave continues to propagate through the body and provide a quality image of a reasonable depth. Without the gel, the acoustic mismatch between the transducer and the air would be so large that the US wave would not reach into the body; it would immediately reflect. It is also important to have a uniform layer of gel between the transducer and the surface to prevent air bubbles. If air bubbles were to form, the US image may have artifacts from the acoustic mismatch within the bubbles. The artifacts are essentially images that are not representative of the real biological structures, meaning they are artificial (Garcia-Martinez et al., 2016).

The reflection fraction can be directly related to the colors seen in an US image. Areas that are dense have a high acoustic impedance and will appear white on the US image. Conversely, fluid-filled areas which are less dense have a smaller magnitude for acoustic impedance and will appear black. For example, an US of the bladder will appear white at the tissue boundary, specifically the bladder wall, and black at the urine-filled portion of the bladder. It is important to note that echoes, as previously discussed, do not occur in fluid filled regions.

2.4.2 Alternative Couplants to Standard US Gel

While US gel is the standard couplant used in medical US imaging, there are other types of couplants that can act to eliminate the air interface at a comparable acoustic impedance to that of tissues. These include alternative liquid or gel-like couplants such as water or cornstarch mixtures or solid couplants such as rubber-like materials. This section also details the basis of NASA's gel-free US system, which couples the use of a rubber couplant and an applied force to eliminate the air interface between the transducer and the sample being imaged.

2.4.2.1 Liquid or Gel-Like Mediums

As mentioned previously, US gel and other gel-like mediums are necessary to fill the air interface between the US probe and the surface being imaged to reduce the acoustic mismatch (high reflection fraction) associated with air. While there is a conventional gel on the market, there are other options that have been explored through several studies across the globe. The commercial gel used in the standard US probe sensing is expensive and can be hard to distribute to less resourceful countries. Some alternative replacements are jellies, lubricants, oils, moisturizers, hand sanitizers, and more. However, these materials may result in inaccurate diagnostics, bodily irritation, or damage to the US transducer.

One successful alternative explored was a mixture of cornstarch and water. Images acquired with this mixture were assessed by radiologists and physicians side-by-side with conventional gel images. Surprisingly, the cornstarch mixture was deemed to be adequate with no significant differences from the conventional gel (Salmon, 2015). The results from this study

demonstrated that an alternative medium is feasible. Additionally, olive oil has also been explored as a replacement for commercial gel for sonographic imaging. It was concluded that there was an insignificant difference between the two mediums. Furthermore, olive oil could function as a replacement to commercial gel, seeing as it is lower cost, pleasant smelling, and easier to handle (Luewan, 2007).

Another possible alternative to US gel was also explored by a multidisciplinary team who worked alongside clinicians from the Democratic Republic of the Congo and Ethiopia. The goal was to create a low-budget gel out of local resources and ingredients applying the Human Centered Design methodology. Cornstarch-based gel mixtures proved to work; however, cornstarch was not available due to geographical issues and inflated price from its scarcity (Aziz, 2018). The final "gel" was found to be composed of 8 parts ground cassava root flour, 1 part salt, and 32 parts of water. Its components were boiled to the desired consistency and viscosity then cooled for 2 hours. The "gel" was named Cassava Flour Slurry (CFS). Eight scans were taken for evaluation using CFS from the following locations: hepato-renal, median nerve block, and lung sliding parts. These scans were compared to scans acquired at the same locations but using commercial gel, and it was concluded that there was no variance in image quality. There was also no report of skin reactions. CFS was later used in the imaging of thirty pregnant women and compared to images taken with conventional gel. CFS was found once again to be of equal quality to commercial gel, since no significant differences were found ($p = 0.3$) (Binkowski, 2013). Judging from these results, it was noted that CFS has comparable image quality to the conventional gel and could improve access to lower resource countries.

2.4.2.2 Solid Mediums

There are other solid materials, especially rubbers, that may have acoustic impedances that mimic that of tissues. A benefit of using a solid couplant is the ability to perform testing of a sample that is submerged into a liquid, as a solid couplant will not disperse in the liquid. A solid couplant also requires less clean-up post-imaging compared to a gel.

Guillermic, Lanoy, and Strybulevych (2019) studied the creation of a solid medium couplant using various mixtures of polydimethylsiloxane (PDMS) and titanium dioxide (TiO_2). The ratio of TiO_2 particles to PDMS was explored to determine a concentration that would exemplify an acoustic impedance comparable to that of water, in attempts to facilitate underwater USing. This PDMS-TiO_2 mixture is indicative of a composite material that can scatter US waves since they would reflect off the TiO_2 particles, suggesting higher concentrations of TiO_2 would indicate greater acoustic mismatch between the tissues. This experiment tested concentrations of TiO_2 particles between 10% and 25%. Attenuation was found to increase when the prevalence of TiO_2 particles increased, demonstrating that such a method is useful in fine-tuning the acoustic impedance and desired level of attenuation by creating a composite material.

Cafarelli et al. (2016) explored the acoustic impedances of a variety of rubber-based materials, including double-component silicones (Ecoflex00-10, Dragon-Skin Medium) and double-component polyurethane rubbers. The polyurethane rubbers were manipulated to include liquid components (glycerol, commercial detergent, N-proponal) or solid components (aluminum oxide, graphene, steel, silicon powder). Acoustic impedances increased when the Ecoflex was supplemented with increasing volumes of glycerol or detergent. The acoustic impedances of

Dragon-Skin Medium decreased when N-proponol was added at increasing concentrations. The implications of this study were more relevant for the use of phantoms as opposed to a couplant.

2.4.2.3 NASA Gel-Free Ultrasound System

The key design component of NASA's ultrasonic transducer developed by Zalameda and Johnston (2016), described in the Floating Point Ultrasound Transducer U.S. Patent No. 9,354,206, is the lack of a wet couplant acting directly upon the surface being imaged. Ultimately, a gel-free system was achieved in their design. The ultrasonic transducer is vertically displaced using an actuator, which has the purpose of applying a periodic force on the sample, which is coupled with the transmission of ultrasonic energy. While both the force exerted by the transducer and the ultrasonic input pulse are periodic, the ultrasonic input pulses are transmitted at a higher frequency of at least 1 MHz in comparison to the sonic frequency of at least 50 Hz for the exerted force. The host machine processes and quantifies the level of attenuation from the transmitted ultrasonic impulse to detect defects in the sample; defects in samples can scatter the ultrasonic signal and result in a smaller output pulse. (Zalameda & Johnston, 2016)

This entire system consisted of an actuator, an ultrasonic transducer, a dry couplant, a scanning device to aid in the positioning of the transducer along the surface being imaged, and a system that operates in communication with the ultrasonic transducer. The communication system consists of an ultrasonic pulse/receiver that focuses on ultrasonic energy transmittance to the sample, a pulsed actuator power supply to power/displace the actuator, a processor to quantify the attenuation of ultrasonic energy based on the return pulses, and a host machine to formulate conclusions based on the processed return pulses. The space between the dry couplant and the transducer is filled with a wet couplant like fluid or gel. A perforated "skirt", characterized by having many pores, eliminates the air interface between the transducer by applying a vacuum to suction the transducer to the surface being imaged. (Zalameda & Johnston, 2016)

Oscillating the US transducer vertically on the surface, thus exerting varying forces on the sample, results in a gliding motion of the transducer across the surface. The actuator lowers the transducer so that it exerts a force on the sample, lifts up the transducer to alleviate the force, and glides laterally to another location on the sample to repeat the process again. This "hopping" motion reduces the overall applied force which consequently lessens the net frictional force acting on the transducer. (Zalameda & Johnston, 2016)

The dry couplant can rest upon the sample, remaining stationary in respect to the gliding transducer, or it could also be wrapped around the transducer to allow these two components to move in unison. The latter set-up entails a dry couplant that is fully enclosed around the transducer, with an inner compartment containing a wet couplant (water or gel). The dry couplant was shaped so that it came to a point at the tip to help transmit the sonic pulses when the transducer contacts the sample. (Zalameda & Johnston, 2016)

2.5 Ultrasound Imaging

US imaging is a complex and multifaceted process, with different modes of image acquisitions, tests for quality, and methods of signal processing. Consequently, its complexity necessitates an establishment of standards from the American Association of Physicists in

Medicine to ensure the system is operating at an acceptable capability. This section goes into more depth about the different imaging modes, techniques, quality tests, and signal processing.

2.5.1 Ultrasound Imaging Modes

Involved in the process of US imaging is choosing the mode of imaging dependent upon the desired application. Two examples of US imaging modes include B-mode where the B stands for brightness, and Doppler Mode involving the doppler shift. B-mode is used for producing 2D images and can be used for both diagnostic and therapeutic purposes (VISUALSONICS, n.d). Through the use of linear array transducers, a plane is scanned producing a 2D image with many "dots" (interpreted as pixels of an image) that have different levels of brightness to form the complete image (VISUALSONICS, n.d) (Carovac, Smajlovic, & Junuzovic, 2011). The levels of brightness are dependent upon the intensity of the returning echo from the object being identified (Natalja, n.d.) In other words, the greater the amplitude of the echo, the greater the brightness of each dot that makes up the image. B-mode imaging can be applied to image guided injections for therapeutic purposes, determine structural anomalies, visualize movement of the cardiac cycle, and find tumors, lesions, or cysts (Carovac, Smajlovic, and Junuzovic, 2011).

Doppler mode for imaging is another mode that is suited for measuring blood flow. When analyzing a volume, the direction and speed of the volume can be seen in an image by calculating the frequency shift. The doppler effect allows knowledge of how close or far an object is from the transducer. If the signal received back from the object is bigger than the frequency of the signal emitted, then it indicates that the object is close. If the signal received is smaller than the frequency of the signal emitted, then it is an indication that the object is far. This can be represented using a pulsing sound because it is within the audible range, and it is also referred to as the doppler shift, which is the difference between the signal that is transmitted and received. There are other ways to display the information produced through the use of doppler mode such as power Doppler (non-directional), color Doppler with an image (directional), and spectral Doppler shown graphically (Carovac, Smajlovic, & Junuzovic, 2011).

2.5.2 Advanced Imaging Techniques

Harmonic Imaging exploits the nonlinear US waves in the body. The first wave experiences distortion when transmitted into the body, and the harmonic wave can compensate for this by amplifying the first wave to produce better readings. This technique has improved axial and lateral resolution, increased signal to noise ratio, and reduced wall reverberation as well as side lobes. Moreover, Spatial Compound imaging is used greatly in the breast, musculoskeletal, and blood vessel applications. This method uses electronic beam steering of the transducer array which allows for multiple scans of one area from different angles (Entrekin, 2001). Images can be taken anywhere from three to nine times of one given area. Results show improved image quality due to the reduction of clutters, speckles, and other artifacts. Furthermore, spatial compound imaging has shown great development in image contrast resolution and tissue differentiation sections.

Speckle reduction is a big factor in US imaging. The reduction of speckles is difficult to pull off without blurring the image's sharp features. These features include corners, edges, and targeted points. Adaptive speckle reduction is when important features such as the location and edges of the image are estimated to further analyze the pixels. Then, every pixel is applied to an adaptive filter that is aligned to the nearest edge on the image. As a result, the image's shape and

adaptive filters are produced by the length of distance and angles (Eom, 2011). Another technique focuses on tissue aberrations, which are mainly caused by sound speed variations, leading to poor readings of histotripsy pulses. Aberration correction is meant to measure the phase aberrations by the placement of a hydrophone at the specified site in vivo.

2.5.3 Tests for Ultrasound System and Image Quality

The American Association of Physicists in Medicine (AAPM) and the American College of Radiology (ACR) have set boundaries of how to determine the quality of US images. Assessment should begin with acceptance testing, which will populate performance baselines to compare test results to. Such tests include "physical and mechanical inspection, image uniformity/artifact survey (each transducer port on the scanner should be tested), geometric accuracy, system sensitivity, spatial resolution, contrast resolution, and fidelity of US scanner electronic image display(s)". While these tests are to be performed when the US device is first obtained, some tests should be completed annually on the instrument. These annual "performance evaluations" include tests for "system sensitivity, geometric accuracy, contrast resolution, spatial resolution, fidelity of the display device(s) used for primary interpretation, and doppler functionality (quantitative or qualitative evaluation)". (AAPM, 2016)

Physical and mechanical inspection of the US device pertains to the mechanical integrity of the device and ensuring it is safe for both the patient and the operator. An image uniformity and artifact survey identifies artifacts that are present in images. An example of this test is done with an "in-air" image (no gel or phantom) and comparing it to a typical gel/phantom image (ACR, 2019). Tests for geometric accuracy assess the US instrument's measurement of depth, volume, and size of objects so that it is accurate to the real horizontal and vertical measurements obtained using calipers (ACR, 2019).

System sensitivity, a "measure of minimum detectable echogenicity", is quantified through signal-to-noise ratio (SNR) or penetration (Ustuner & Holley, 2003). To determine sensitivity, a normal image with a phantom would be taken, and then a noisy image would be taken (with transmitters turned off). Each image would be low-pass filtered with the amplitude detected and log detected to produce signal mean and noise mean plots (e.g. azimuth (°) vs. depth (cm)) (Ustuner & Holley, 2003). Moreover, penetration is defined as the depth where the SNR is less than 6 dB or where the correlation coefficient (frame-to-frame correlation) is less than 0.5 (Ustuner & Holley, 2003). Parameters of interest for US scanner electronic image display performance include gray scale response and luminance calibration, presence of pixel defects, and overall image quality. Contrast resolution can be characterized by clutter energy to total energy ratio (CTR) or contrast to noise ratio (CNR). CNR is more applicable for the imaging of soft tissues (Ustuner & Holley, 2003). Information density can be found by squaring the CNR and dividing by the average speckle size as indicated in **Equation 5** below (Ustuner & Holley, 2003).

$$\textbf{Information Density (ID) = CNR}^2\textbf{/S}$$

Equation 5: *Information Density (where CNR is the contrast to noise ratio and S is the speckle size)*

Because information density is dependent on the object, this value can be normalized to represent the normalized information density "to distinguish 1 dB brightness differences in the presence of fully-developed speckle", using **Equation 6** below (Ustuner & Holley, 2003).

$$\textbf{Normalized Information Density (NID)} = 1/(2S\sigma^2_{speckle})$$

Equation 6: Normalization Information Density (where S is the speckle size and σ is the variance)

In addition to contrast resolution, another type of resolution includes spatial resolution, encompassing axial, lateral, and elevational directions. Axial and latter resolution refers to how well the US device can distinguish two separate objects (poor resolution would lump two small objects as one in the US image).

Outside of the AAPM standard protocols, there are other parameters that should be considered to determine if an US image is of good quality. The dynamic range of an US system is characteristic of the range between the least visible echo to the maximum echo; this appears as a "gray scale" which corresponds to the amplitude of the echoes received. The surroundings about a focal point where there is prime lateral resolution is referred to as the focal zone (i.e. surpassing the focal zone is indicative of poorer lateral resolution and thus a poorer quality image). (ACR, 2019)

2.5.4 Signal Processing

Signal processing of US data functions to take a large amount of information and compact it to ease the interpretation and analysis of the data. Signal processing that occurs before the data is stored in the computer is termed preprocessing; post-processing occurs after the data is stored. Examples of preprocessing include time-gain compensation (TGC), selective enhancement, log compression, fill-in interpolation, edge enhancement, image updating, and write zoom. TGC functions to compensate for the reduction in the signal amplitude due to attenuation by amplifying the signal in a time-dependent fashion. Selective enhancement builds upon TGC by amplifying signals as needed (non-uniformly) as desired for specific regions of interest. Typically, US images (signal amplitudes) are stored as 8 bits, meaning there are 256 possible shades of gray total. Because the amplification from TGC can cause the signal amplitudes to exceed 256 by several orders of magnitude, logarithmic transformations are used to compress the data to fit in the 0-256 range, a process termed log compression. Additionally, if there are blank pixels, a fill-in interpolation is executed by averaging the signals of nearby pixels to fill-in the blank pixel.

Edge enhancement helps to make boundaries and interfaces (e.g. the difference between tissue and bone) appear more dramatic and noticeable in an image by applying a weighting factor to the amplitude. Image updating refers to how the old amplitude values for a specific location of imaging will be kept in the memory until a new value is obtained, which would replace (alternative could be averaging the old and new values). Lastly, the write zoom allows the image to be magnified to a specific, desired field-of-view. Because the total number of pixels are maintained while the dimensions of the region-of-interest (ROI) are decreased, there is a greater number of pixels per length. (For example, a 5x5 matrix compared to a 4x4 matrix would have less pixels per each 1x1 component.) Consequently, the spatial resolution would be increased. (Hedrick & Hykes, 1989)

Post-processing pertains more to the display of the US image since it occurs after the data is preprocessed and stored. The 256 possible values in 8-bit storage correspond to different intensities or brightness of gray. This grayscale map thus shows the relationship between signal amplitude and the brightness level. Black/white inversion would produce images that appear black at high amplitudes and white at low amplitudes, which is a reverse of what is normally shown. Freeze frame stops image acquisition and displays a stagnant image on the screen for longer viewing. Read zoom allows the user to magnify an image which was already taken, although it does not increase the number of pixels for smaller dimensions (spatial resolution stays constant). Some post-processing techniques relate more to data manipulation and analysis. For example, contrast enhancement can shift the linear gray scale map to allow gray or white values to occur at higher amplitudes. A linear gray scale map (pixel value vs. brightness) would cause gray to occur at the middle of the 0-256 pixel range, which is 128. Contrast enhancement may steepen the slope of the brightness/pixel value line, causing bright and white colors to occur at higher pixel values. This form of post-processing does not change the number of pixels, but rather changes the physical display of brightness at different amplitudes compared to the linear grayscale map. Smoothing is useful to reduce noise by averaging nearby pixels to generate a new value. Additionally, distance calculation can be performed, which is more so a form of data that can be obtained from the image. If one pixel translates to a set length of the actual object, then the real, physical dimensions for a ROI with a set number of pixels can be determined. (Hedrick & Hykes, 1989)

2.6 Electrical Systems with Linear Actuators

Actuators can be incorporated into a mechanical system in order to initiate movement based on the inputs it receives. One type of actuator, called a ball screw actuator, can produce linear motion due to the clockwise or counterclockwise turning of a lead-screw. A shaft is fixed to the screw so when the screw turns, the shaft moves with it in a direction dependent on the direction of the rotation. This rotary motion of the screw is made possible by electrical pulses sent to a stepper motor. Stepper motors typically operate so that it would take 200 steps per one complete revolution of the screw, meaning 1.8° per step. The vertical displacement of the shaft from one revolution would be determined by the pitch of the screw, which is the distance between the threads. For example, a screw with a pitch of 1mm would displace the shaft 1mm from one revolution, 2 mm from two revolutions, and so forth. The direction of rotation is based on the polarity of the voltage supplied from the power supply, where clockwise rotation would displace the shaft downward and counterclockwise would displace upward. Moreover, the maximum distance the shaft can traverse is defined by the stroke length, which is the difference between the fully extended state and the fully retracted state of the actuator.

The movement of an actuator requires a few other components. First and foremost, a power supply is needed. An Arduino can be used to control the movement of the actuator since it is composed of a microcontroller (a physical circuit board which can be controlled) and an Integrated Development Environment (a computer software that allows code to be written and uploaded for the physical board). However, because an Arduino operates at a voltage of 5V with small limits, an intermediate component is needed for the actuator to be controlled, since it may operate at 20-50 V. For a stepper motor-powered actuator, a stepper motor driver is needed to act as the intermediate. Besides being able to control the amount of voltage supplied to the Arduino, the stepper motor driver has additional benefits in the sense that it can increase the precision of the stepper motor. Whereas the typical stepper motor operates at 200 steps per revolution ("full step"),

the stepper motor driver can increase the number of steps per revolution. For example, a stepper motor driver set to the ⅛ step option would have 1600 microsteps per revolution (0.225° per step) as opposed to 200 steps per revolution (1.8° per step).

In addition to the electrical components previously mentioned, sensors can be incorporated to provide feedback for the stepper motor to respond to. There are both digital and analog pins on the Arduino board which can be used depending on whether the input from the sensor is binary or a range of values, respectively. An example of a sensor that can be used is a load cell, which is essentially a force sensor. The Arduino can be used to take the readings from the load cell as an input. The Arduino code could then be written to tell the stepper motor to perform some action based on the value read in as an input. For example, a code may be structured so that a force reading of 3 N will tell the actuator to rotate 1 revolution, while a force reading of 6 N will cause it to rotate 2 revolutions.

3.0 PROJECT STRATEGY

The goal of this project is to determine a method to eliminate the need for topical gel on the skin for US imaging. The solution includes electrical, mechanical, and material components to acquire high quality images. The electrical and mechanical components include a Clarius US transducer to acquire images, a linear ball screw actuator to move the transducer vertically, and a load cell to sense the forces the transducer exerts on a surface. The material component contains materials intended to mimic the properties of topical gel including polydimethylsiloxane (PDMS), PDMS mixed with solid titanium dioxide, neoprene rubber, and nitrile rubber. The quality of images acquired without topical gel were intended to be of comparable or equivalent quality as the reference image, which was the conventional image acquired with topical gel. Each component of this project has a potentially important role in the overall success of this project; therefore, each element was carefully cultivated and validated.

3.1. Client Statement

The client is in need of an US Imaging Instrument for diagnostic or therapeutic purposes that will not require the use of a topical gel interface between the US probe and the surface being imaged. The images acquired should be of equivalent or comparable quality as those that would have been achieved with the use of gel as a conductive material. Moreover, air between the probe and the surface should be close to nonexistent. The device should be easy to operate, lightweight, and sterilizable. Aesthetics should be taken into consideration but not prioritized over function.

3.2 Revised Client Statement

The client is in need of an US Imaging Instrument for diagnostic purposes that will not require the use of a topical gel. The images acquired should be of equivalent or comparable quality as those that would have been achieved with the use of gel as a conductive material. The device should be easy to operate, lightweight, and sterilizable. Aesthetics should be taken into consideration but not prioritized over function.

4.0 METHODOLOGY

The primary components of the methods used in this project include the development of an actuated US transducer system to vertically displace the US probe, manufacturing of solid biomaterials to replace topical gel, and signal processing means to quantitatively assess image quality. Each of these components have their own design process, alternative designs, and design verification, which are discussed in this section. Following the detailing of these three components of the methodology, the final design will be discussed, demonstrating how each component comes together.

4.1 Project Overview

The project's many components were developed simultaneously and eventually came together at the completion of the project. Major milestones can be characterized under specific academic terms (A, B, C, D) and major phases. For a visual representation of the subsequent timeline discussed, see **Appendix A** with 'Gantt Chart of the Project'.

The project began with the Developmental Phase, which lasted eight to nine weeks or the entirety of A Term along with a portion of B Term. In this phase, the team completed an extensive literature review. It was important to develop the scope of the project and form a basis for the direction that the project would go in. A large portion of this research was presented in the Literature Review Chapter of this paper. Once the scope and important aspects of the project were established, the team began to design the project. This included what the team would need to develop, the form of imaging that would take place, and how the project would be conducted for the duration of the academic year. Key milestones that would need to be met in order to reach the project's goal were also established. Then, imaging and design parameters were outlined, followed by a brainstorm of the design of the system. This was an iterative process, where many different factors of the product were considered. A rough prototype design was established, and the team explored and purchased the components necessary to build the prototype.

The next phase of the project was the Experimentation Preparation Phase, which lasted the first four weeks of B term. It began with the purchasing and acquisition of prototype materials. Some important materials that were purchased were the ball screw actuator, load cell amplifier, load cell, and US phantom. As these materials were in transit, the team developed the details of the actuator system. This was an extensive learning curve process, seeing as it was a new technology for the team to learn. Similarly, signal processing dictated another learning curve as it was a new concept for the entire team. This would be used in order to analyze the experimental data collected and the draw conclusions of the project. Lastly, an experimental plan was developed, with careful consideration of the experimental goals outlined at the start.

For the remainder of B Term, The First Experimentation Phase took place about three to four weeks. This was a pivotal time for the team because the first experimental data was collected, where the role of topical gel in imaging was tested. Dhirajsinh's pneumatic actuation system was used; the US transducer was lowered until it exerted a force on the sample and images were taken. Additionally, the team created the first PDMS samples to be used as the dry couplant. To finish this phase, the team then collected reliable images with and without gel to be analyzed as experimental data. The team then processed the data through the signal processing pipeline that was iterated continuously. Finally, the assembly of the actuator system began.

The Second Experimentation Phase of the project was conducted throughout the entirety of C Term. Issues presented in the First Experimentation Phase were addressed, trouble-shot, and improved upon; next steps in the system were taken as well. The term began with a solidification of the details pertaining to the experimental plan, experimental system, and required technical components. There were issues encountered with the 3D print and actuation system, however they were eventually resolved through several rounds of troubleshooting and even reprinting the 3D print. Moreover, in the middle of the term, the team developed the second iteration of PDMS samples. It was found that lower concentrations of TiO_2 were needed. All current materials were then imaged, and signal processing was performed on the results. Thus, conclusions were able to be drawn on across gel versus no gel conditions as well as different materials.

In D Term, the final term, the team completed the Third Experimental Phase. This phase consisted of the first four weeks of the term, and many developments took place. After unexpected issues, the actuator system became fully functional. New PDMS samples were manufactured in the third week, with lower concentrations of TiO_2. These new materials were then also imaged to have a full dataset of all materials analyzed for the project. With the fully functional system and all materials finalized, the team then conducted frequency testing: the final stage of testing where US images were taken with the actuated US system operated at frequencies of either 6 Hz or 14 Hz. This "sonic" frequency is characterized by the speed at which the actuator lifts and then lowers the US transducer at a specified height (i.e., in cycles/second). Signal processing for frequency testing started in this phase and continued into the next, the Conclusion Phase. In the fourth, fifth, and sixth week of D Term, signal processing of data finished and conclusions to the project were drawn.

That encompasses the entirety of the 'US Imaging without Gel for Clinical Application' project. It had six major phases including: The Developmental Phase, the Experimentation Preparation Phase, The First Experimentation Phase, The Second Experimentation Phase, The Third Experimentation Phase and the Conclusion Phase. The project clearly followed an iterative design process where the project's design was continually improved upon until the final system was produced. The project took place over the course of twenty-seven weeks.

4.2 Design Ideation

During the Developmental Phase of the project, the team determined the design requirements needed to reach the project goals. Based on these requirements, the team ideated four different design ideas. This section discusses the designs ideated as well as the process of evaluation used to proceed with only one design.

4.2.1 Preliminary Designs

During the ideation portion of the Developmental Phase, four designs arose. The first two designs focused on the gel replacement component alone, without adding any changes to the transducer. Design #1 was a membrane-enclosed gel which could "clip-on" to the US transducer. The membrane would have consisted of a thin, rubbery material that had similar acoustic properties to skin and could glide across the surface being imaged. Design #2 was an adhesive patch that had an inner gel layer. It would be pre-packaged, individually wrapped, and sterile. The clinician would unwrap the patch and attach it to the surface being imaged. Since both design concepts were purely

material in nature, extra considerations and detailed planning did not occur for these in the brainstorming phase.

While Designs #1 and #2 focused on the gel couplant component alone, the team wanted to brainstorm ideas that would change the motion of the US transducer. Inspired by the NASA U.S. Patent No. 9,354,206 by Zalameda and Johnston (2016), the team planned Design #3 to use actuation as a method to reduce friction when gliding the probe. Because this solution is very technical in nature, much planning went into it, including the 3D printed parts needed, electrical components, and set-up. Firstly, an actuator would be needed to displace the US probe in a tapping motion. Tapping the probe along the sample instead of dragging would reduce the overall net friction. The actuator would be attached to the portion of the actuator that undergoes linear, vertical motion such as through a 3D printed component to perfectly fit it.

Due to potential risk of the actuator lowering the US transducer to an extent that would inflict pain on the patent, a load cell would be incorporated. Force would have to be read in and adjusted continuously to account for any external forces the clinician applied simply from human operation. This would ensure the force applied to the skin would be constant, regardless of how much pressure the clinician would incite. For the load cell to read the force the transducer exerts on the skin, the load cell would have to be fixed, and the US transducer would have to be freely moving so that it can push up against the load cell. To better visualize this, **Figure 1** below shows how the US transducer (green), load cell (orange), linear actuator (grey and black), and 3D-printed components (red and blue) would fit together to form Design #3.
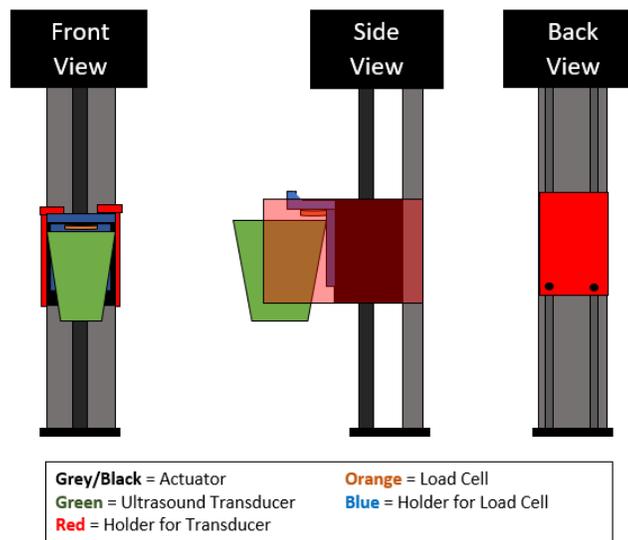
Figure 1: Design schematic of Design #3. US transducer (green), actuator (grey/black), and load cell (orange) with components that would be 3D printed (red/blue).

As shown in **Figure 1**, the orange load cell would be fixed to the black box on the actuator, called a shaft, via the blue 3D print. The red 3D printed part hooks onto the black shaft and holds the green US transducer. As seen, there is a small amount of space between the transducer and the load cell. When the actuator lowers the US transducer onto the sample to cause a force on the sample, the US transducer will move up and hit the orange load cell. The tapping motion would

then consist of the actuator lifting the probe up and down at a frequency designated in the Arduino code.

While Design #3 seemed promising, several areas for improvement came to the team's attention. The difficulty associated with writing a code to continually read forces and adjust them inspired Design #4. For this design, an actuator, transducer, load cell, and 3D prints would still be used. However, the actuator could be held at a fixed height (i.e., no variable forces exerted by the clinician operating the probe). Fixing the system vertically would allow the team to control for variable forces without having to write a complex code. With this design, the actuator could lower the US transducer until it reaches a designated amount of force (e.g., 5 N). Then, it would displace the US transducer equal distances up and then down so that the net movement is 0, meaning it returns to the initial exerted force every time.

4.2.2 Design Selection

In order to decide which of the four designs to pursue, the team had to reflect on the client statement. Additional input requirements that would benefit the project outcomes were explored as well. From this assessment, five key "functional blocks" were determined. These included 1) having similar acoustic properties to tissues, 2) eliminating the air interface between the US transducer and sample, 3) minimizing frictional forces associated with a gel-free condition, 4) having sterilizability, and 5) being easy-to-operate and lightweight. In this ranked list, number one represents the most important functional block, while number five would represent the least. The ranking order was determined by prioritizing the functional blocks that would contribute the most to meeting the goal of comparable or equivalent image quality.

Based on the five functional blocks, a Pugh Concept selection matrix was utilized. The highest-ranking functional block (#1) would have the highest weight of points (5). An additional category was added to supplement the five functional blocks: feasibility. While a solution may stand out as the most promising, the feasibility of it being achieved in one academic year should be taken into consideration. This new input requirement was ranked in the fourth position alongside sterilizability. Furthermore, the baseline was established as a gel-free US system rather than the standard, since it is a given that the proposed designs are likely to be lower ranking than the gold standard. Thus, it made more sense to see if the proposed designs rank better than the worst condition: US imaging without any gel, actuation, or couplant. Baseline is defined as all 0's for the points. If a design is better than the baseline in any of the categories, it will be assigned a 1. If it is the same, it is assigned a 0. The scores for each category are multiplied by the weight, and then all the scores are tallied up. The design with the highest-ranking score was the one selected to proceed with. The Pugh Concept selection matrix for Designs #1 through #4 is shown in **Table 1** on the next page.

Table 1: *Pugh Concept Selection Matrix for four different design ideations.*

Objective	Wt.	Gel-free US (Baseline)	Membrane Enclosed Gel	Gel Adhesive Patch	Actuated Transducer System #1	Actuated Transducer System #2
Ideal acoustic properties	5	0	1	1	1	1
Eliminate air interface	4	0	0	0	1	1
Minimize friction	3	0	0	0	1	1
Sterilizability	2	0	0	0	0	0
Feasibility	2	0	1	1	0	1
Easy-to-operate	1	0	1	0	0	0
Lightweight	1	0	1	1	0	0
Rank Score		0	7	6	12	14

Based on the results from the Pugh Concept selection matrix, Design #4 had the highest number of points: 14. While the first iteration of the actuated transducer system was very promising, the feasibility of this design was lacking. It was inferred that project outcomes would be the best with a more simplified and controlled system to get results like Design #4, and then future research could progress to a more complex system like Design #3, which would have accommodated for variable lateral and vertical motions applied by the human operator.

4.3 Final Design

Once the design idea to proceed with was selected, the process of finalizing the design began. The two main components were the actuated US transducer system and the solid couplant to replace gel. Testing was performed periodically through the First, Second, and Third Experimentation Phases to validate the design and test the hypotheses of the project. The following sections detail both design and testing.

4.3.1 Actuated Ultrasound Transducer System

With the inspiration of the project lying in the Zalameda and Johnston (2016) U.S. patent No. 9,354,206, one important component of the gel-free US imaging system is the hopping motion of the US transducer to avoid friction associated with gliding a probe on a gel-free surface. An actuator can be used to achieve this by providing linear motion to whichever component is attached to it. This section details the methods used to create this linear actuation system in order to translate the US transducer vertically at a designated frequency.

4.3.1.1 Materials

The primary components of the actuator system included the linear actuator, a motor driver board, and an Arduino board. A load cell, and the subsequent amplifier, was of use as well to output force data. A list of materials used for the actuator-transducer system along with the design specifications is shown in **Table 2** below.

Table 2: Materials purchased for the actuated US transducer system.

Material	Ball Screw Linear Stage Actuator	3 kg Load Cell	HX711 Load Cell Amplifier	TB6560 Stepper Motor Driver Board
Source	Ebay	Amazon	Amazon	Amazon
Manufacturer	RATTM Motor	Calt	SparkFun	HiLetgo
Model #	CBX1605-100A	DYHW116	B01K7Z02IW	3-01-0146
Price	$92.90	$60.00	$15.61	$9.99
Size	100 mm	182.88 x 73.91 x 29.97 mm	76.2 x 50.8 x 25.4 mm	70 x 50 x 33 mm
Specifications	X-axis load: 30kg Y-axis load: 10kg Max speed: 50 mm/s Stroke length: 100mm Motor: Nema23 High Torque Stepper Motor Accuracy: 0.03mm Current: 3A	3kg Compressive Force 5-12 V Sensitivity: 1-2 mV/V Input: 400Ω Output: 350Ω	2.7-5 V < 1.5mA	10-35 V DC ± 3A max output

The maximum vertical and horizontal loads for the Ball Screw Linear Stage Actuator (RATTM Motor, CBX1605-100A) are 30kg and 10kg, respectively. The actuation force is produced by the NEMA 23 High torque Stepper Motor, which would be controlled by the TB6560 Stepper Motor Driver Board. In **Figure 2** below, an image of the actuator can be seen.
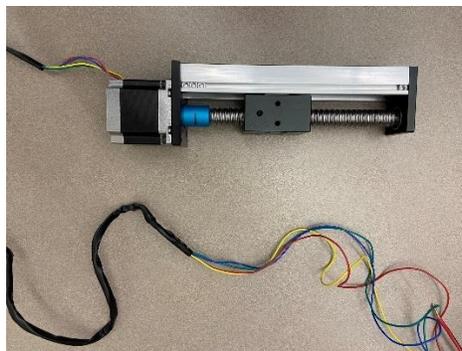
Figure 2: Ball screw linear stage actuator. NEMA 23 high torque stepper motor positioned at left with colorful wires coming out, stepper motor can spin the screw at the blue cylindrical section, and black rectangular box, "shaft", displaces along the screw.

It is important to note how the actuator operates in order to fully understand the design. When a voltage is applied to the stepper motor of the actuator, as shown as the grey and black box on the left side of Figure 1, the actuator moves. A code is written in the Arduino desktop program, which can be uploaded to the Arduino board. The stepper motor driver board takes the commands from the Arduino and sends pulses to the stepper motor accordingly. The screw rotates in "steps", which are fractions of a full rotation. Normally, the stepper motor completes one rotation in 200 increments or steps. If the stepper motor rotates counterclockwise, the shaft on the actuator will displace downward and vice versa. The step settings can be specified by flipping switches directly on the stepper motor driver board. More steps per revolution indicates a higher resolution and smoother motion. For example, ⅛ step setting completes 1600 steps per revolution, instead of the standard 200 steps. **Table 3** below summarizes how the steps can be varied on the driver board.

Table 3: Microsteps guide for the TB6560 stepper motor driver board.

Microstep resolution	Steps Per Revolution	S3 Switch	S4 Switch	Degrees per step
Full step	200	OFF	OFF	1.8
1/2 step	400	ON	OFF	0.9
1/8 step	1600	ON	ON	0.225
1/16 step	3200	OFF	ON	0.1125

4.3.1.2 Electrical Connections

Evidently, the TB6560 driver board acted as the intermediary between the voltage supply and the stepper motor, which allowed careful control of the microstep resolution. For all testing, the driver board was set to the ⅛ step setting, meaning 1600 steps per revolution. Also connected to the driver board was the Arduino board. Similarly, the load cell amplifier acted as the intermediary between the load cell and the Arduino board. The connections necessary for the actuator or the force-sensing components are shown below in **Tables 4 and 5**, respectively.

Table 4: Connections for the actuated component of the electrical system.

TB6560-Arduino Connections		TB6560-NEMA 23 Connections		TB6560-Power Supply Connections	
TB6560	**Arduino**	**TB6560**	**NEMA 23**	**TB6560**	**Power Supply**
CW+	Pin 4	B+	Red wire	+24V	+
CLK+	Pin 5	B-	Green wire	GND	-
CLK-	GND	A+	Yellow wire		
CW-	GND	A-	Blue wire		
EN-	GND				
EN+	GND				

Table 5: *Connections for the load-sensing component of the electrical system.*

HX711-3KG Load Cell Connections		HX711-Arduino Connections	
HX711	**3KG Load Cell**	**HX711**	**Arduino**
RED	Red wire	VCC/VDD	5V
BLK	Black wire	DAT	Pin 3
WHT	White wire	CLK	Pin 2
GRN	Green wire	GND	GND

To better visualize what these connections entail, **Figure 3** below shows a design schematic of the NEMA 23 stepper motor, the power supply, the TB6560 stepper motor driver board, the Arduino board, the HX711 load cell amplifier, and the 3 kg load cell.
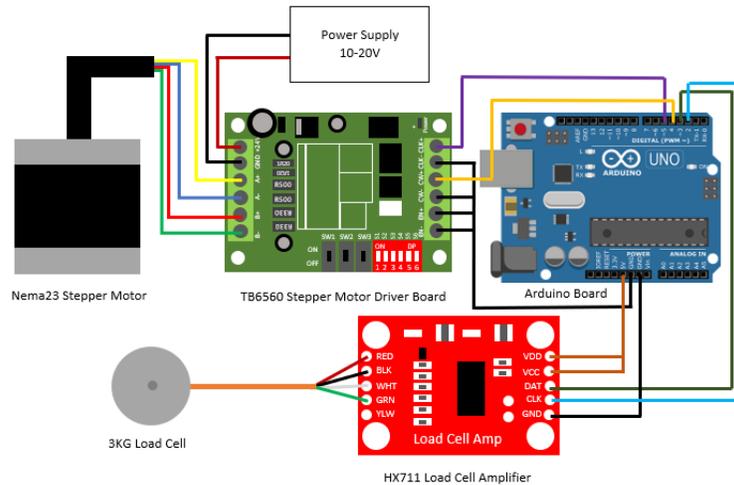
Figure 3: *Electrical system schematic. NEMA 23 stepper motor connected to a TB6560 stepper motor driver board, which is then connected to the power supply (ideally 24 V) and Arduino board. 3kg load cell and HX711 load cell amplifier connected to the Arduino board.*

4.3.1.3 Design Verification

As mentioned, the two main functions of the electrical system were to 1) displace the US transducer via an actuator and 2) sense the force exerted on the sample to provide information to the actuator. The Arduino code written to displace the actuator was tested first. This code essentially controls the time in between the pulses of the stepper motor to effectively determine the frequency of the rotations of the screw, and it can be found in **Appendix B**. The basis of such a code is that the stepper motor can be set to have a specified number of microsteps to complete one revolution, such as 1600 microsteps for the ⅛ step setting. Increasing the number of microsteps per revolution ultimately increases the resolution of the rotations, as the movement would be more smooth. Moreover, the electrical components were all connected, as shown in **Figure 4** on the next page.
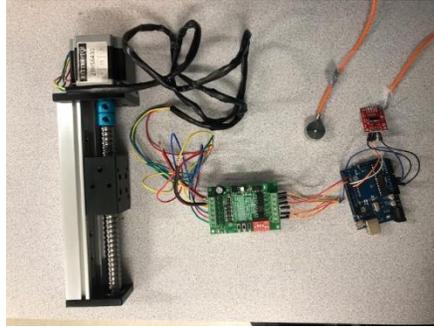
Figure 4: Purchased electrical components set up.

After the components were set up, the Arduino code was able to be tested. The stepper motor driver was put into the ⅛ step mode, meaning 1 revolution would complete in 1600 microsteps or pulses. The first trial of testing operated at a very slow speed in order to fully assess the functionality of the actuator; 2000 microseconds were in between each of the 1600 pulses. It should be noted that the actuator was secured into an upright position using a chemistry ring stand and two clamps to ensure the piece did not topple over from the weight of the stepper motor. This ring stand set-up along with the wiring of the components is shown in **Figure 5** below.

Figure 5: Design verification set-up for electrical system. Actuator secured in a ring stand as well as the TB6560 stepper motor driver board, load cell, HX711 load cell amplifier, Arduino board.

Seeing the first trial of actuator testing was successful, more testing was performed at faster rates, for example, setting the delay in between pulses to be 1500, 500, and 200 microseconds, in that order. Following the decreasing of the delays, the actuator was tested where it would complete one revolution in the clockwise direction and then another in the counterclockwise direction. Consequently, the shaft on the actuator displaced 5mm in the positive y direction and then 5 mm in the negative y direction. The code for this motion was effective, therefore proving that the mechanism of displacing the actuator the same distance in either direction to achieve a net displacement of zero is feasible for this system. However, it should be noted that these preliminary tests did not include calculating a specific frequency from the rotations, which should be performed next.

The second component of the electrical system which needed to be validated was the load cell. The HX711 load cell amplifier was connected to the Arduino board so that the DAT terminal corresponded to pin 3 and the CLK terminal corresponded to pin 2. Attempts were made to calibrate the load cell by using Nathan Seidle's (2014) Arduino code for determining the

calibration factor (refer to **Appendix B**). Ultimately, the procedure for calibrating the load cell begins with running the Arduino code without any weight exerted on the load cell. The calibration code tares the load cell. Then, an object with a known weight is added on top of the load cell, as visioned in **Figure 6** below, and the Arduino code returns a value for the weight in pounds.
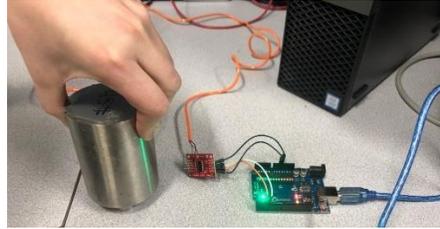
Figure 6: *Application of an object on top of the load cell. Connections to the HX711 load cell amplifier and subsequently the Arduino board.*

If the weight returned does not match the known weight, then the "+" or "-" keys can be pressed to increase or decrease the calibration factor by 10. The calibration factor should be adjusted until the weight returned from the Arduino code matches the actual weight of the object. Moreover, the verification process for the load cell was unsuccessful in the sense that the Arduino code returned a weight of 0 lbs regardless of the amount of weight applied. However, after resoldering all of the connections, the load cell was able to be calibrated correctly. The calibration factor was determined to be 290.

4.3.1.4 3D Printed Components

In order to fix the US transducer to the shaft of the actuator, 3D printed components were needed. The models for the 3D-printed components to attach the US transducer and the load cell to the actuator were created in Autodesk CAD. A Robotics Engineering Master's student at Worcester Polytechnic Institute, Dhirajsinh Deshmukh, helped to design the shape of the 3D prints. In **Figure 7** below, screen captures of the CAD file of the parts to be 3D printed, credited to Dhirajsinh Deshmukh, are shown.
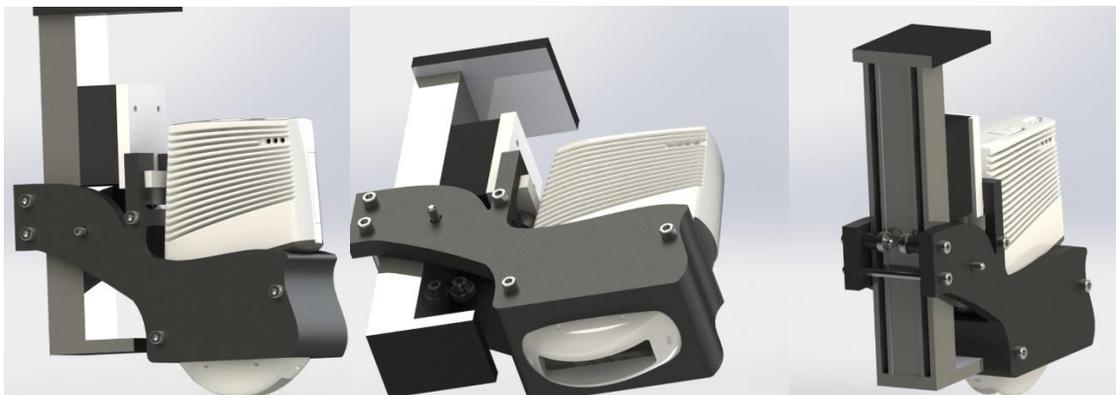
Figure 7: *CAD drawing of parts to be 3D printed, created by Dhirajsinh Deshmukh, Robotics Engineering Master's student at Worcester Polytechnic Institute. From left to right: sideview, under view, and back view.*

The US transducer would be fully enclosed on the sides while the bottom portion would be left open so that the probe could contact the surface being imaged (as shown in the middle image in **Figure 7**). It can be seen that a white rectangle is fixed to the shaft (black box) of the actuator.

There is a protrusion out at the bottom of this piece where the black piece holding the US transducer can hook onto. This hooked mechanism allows the US transducer to push up toward the protrusion when a force is applied, while preventing the transducer from falling away when lifted away from the surface. Consequently, a load cell would be secured to the underside of the white protrusion to read in the forces applied due to the movement of the US transducer. It should be noted that with the load cell secured at the bottom of the shaft, the US transducer would not be directly exerting a force on the load cell; it would be the base holding the US transducer that makes contact with the load cell. In the preliminary designs, it was intended that the protrusion be secured to the top of the shaft so that the top of the US transducer could exert a force on the load cell. However, this idea was no longer considered because the top of the transducer is sloped so the force reading may have been inaccurate. Moreover, the 3D printed parts following these CAD drawings are shown in **Figure 8** below.
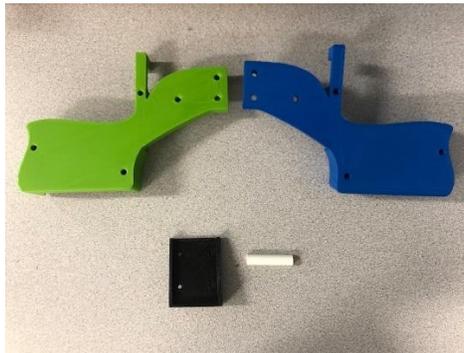
Figure 8: *3D printed parts for the actuated transducer system, where the blue and green parts would join to hold the US transducer, the black part will be fixed to the shaft on the actuator, and the white part.*

4.3.1.5 Device Assembly

The actuated US transducer system required two main parts of assembly: electrical wiring and 3D-prints. All connections were made semi-permanent by either soldering or by securing the wires with screws (e.g., on the stepper motor driver board). The set-up of the electrical components for the final design is shown in **Figure 9** below.
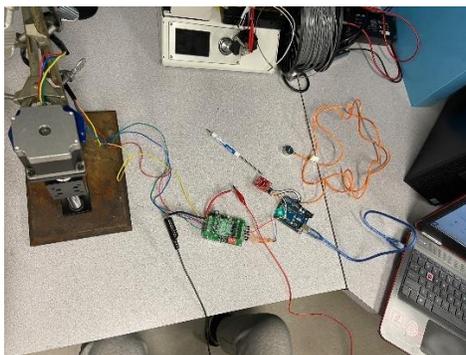
Figure 9: *Set-up of actuated system with the actuator secured to a ring stand.*

The black 3D printed part to hold the load cell was bolted into the shaft of the actuator with M5 bolts. The load cell was bolted to the underside of the black 3D printed part as mentioned previously. The Clarius linear array US transducer was fit into the green/blue 3D printed parts and secured with M5 bolts and nuts. The green/blue 3D printed parts holding the US transducer were

hooked onto the L shaped, black 3D print. Additionally, the green/blue 3D prints were further connected through M5 bolts running from the blue print to green print, behind the actuator. This set-up can be seen in **Figure 10** below, with the various parts labelled.
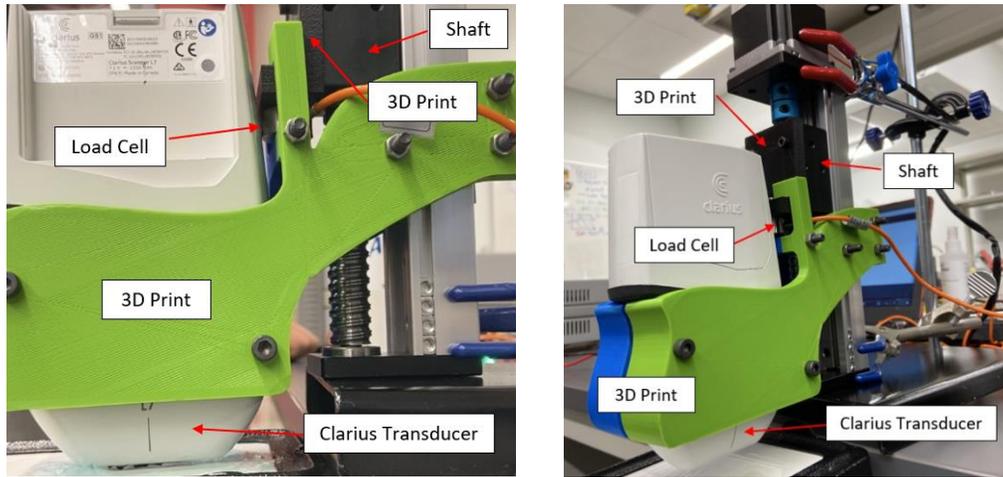
Figure 10: Assembly of actuated US transducer system.

4.3.2 Solid Couplant Materials

Solid couplants were hypothesized to replace the topical gel used for conventional US readings. The team hoped to find or manufacture a dry and solid couplant material that would be sufficient enough to produce comparable readings as compared to conventional readings using topical gel. This section details the design process of identifying potential solid couplants, the preliminary designs, as well as design validation.

4.3.2.1 Selection of Materials

Compared to liquid, gel-like couplants, solid dry couplants are better in longevity, ease of use, and cleanliness. These dry couplant materials should imitate the acoustic impedance of the tissue that is being imaged. Upon brainstorming ideas in the Developmental Phase for dry, solid couplants, dimethylpolysiloxane (PDMS) along with rubber-like materials were chosen by the team. Specifically, nitrile rubber, neoprene, and PDMS were selected as candidates for the dry couplant materials. These materials were chosen because they may have the closest acoustic impedances that mimic that of a tissue during imaging while also being flexible, solid, and sterilizable.

PDMS is made of silicone elastomer base as well as a curing agent, of which both were provided by a biomedical engineering lab at Worcester Polytechnic Institute. Specifically, the Sylgard 184 silicone elastomer base (Sigma-Aldrich) was used. In addition to this, the team decided to add titanium dioxide (TiO_2) to the PDMS material mixture. The TiO_2 particles act as structures for portions of the US wave to reflect from to ultimately increase acoustic impedance. The decision to incorporate TiO_2 was based on a study done by Guillermic (2019), where the researchers tested different various mixtures of PDMS and TiO_2. The amount of TiO_2 used per PDMS ranged from 10% to 25% by volume; the attenuation in these samples was found to

increase, thus demonstrating that the acoustic impedance can be modified to desired levels by mixing of the components at different concentrations.

While the PDMS had to be manufactured in a laboratory by the team, the other solid couplants could be purchased. Additionally, the TiO_2 had to be purchased to add to the samples of PDMS. The table below, **Table 6**, depicts the primary materials the team have purchased for testing and/or making the final dry couplants.

Table 6: Materials purchased for the dry couplant component of the project.

Material	Titanium Dioxide	Nitrile Rubber	Neoprene
Source	Fisher Scientific	Amazon	Amazon
Manufacturer	Fisher Scientific	MATNIKS Rubber	MATNIKS Rubber
Model #	MFCD00011269	B076VHLCP7	B018H9CCPG
Size	1 kg	12 x 12 x 0.12 in.	6 x 6 x 0.18 in.

As mentioned, there are two rubber mediums separate to PDMS that will be tested. These rubber materials include a 1/8 thickness, smooth nitrile rubber (NBR) and a 1/16 thickness, smooth commercial neoprene. **Figure 11** below depicts the two different rubber solid couplants:

Figure 11: Nitrile rubber (left) and commercial neoprene (right).

4.3.2.2 PDMS Manufacturing Procedure

In general, the process of manufacturing PDMS is based on the formation of crosslinks. The Sylgard 184 silicone elastomer base (Sigma-Aldrich) comes in a glue-like consistency. When the corresponding curing agent is added, cross links form, making the PDMS stiffer. The elastomer makes up for the majority of the material and a small amount of curing agent is enough to cure the entire sample. The ratio of elastomer to curing agent will determine how flexible the material is. For example, a 20:1 ratio for PDMS would be stiffer than a 10:1, since there is less curing agent relative to the elastomer.

The process began with using a weigh boat to measure the mass of the elastomer base, making sure to tare the scale before adding the base. Then, the curing agent is carefully added until the desired ratio is met. For this project, ratios of 10:1 and 20:1 were used with 20 g of elastomer base. Once both materials are weighed out to the desired amount, the mixing occurs. Due to its viscous-like properties, PDMS had to be mixed for a minimum of 10 to 15 minutes to ensure that the curing agent was well dispersed into the elastomer base. Unequal mixing would cause the

PDMS sample to have variable stiffness throughout. The PDMS mixture was moved to 9 x 9 cm plastic mold, which was sterile to prevent the presence of dust or unwanted particles. Since the mixing process can cause air bubbles to form, vacuuming is necessary for around thirty minutes. During vacuuming, the air pockets would start rising to the surface of the material, thus indicating vacuuming is effective. Additionally, quick opening and closing of the valves on the vacuum chamber caused air to rush back in the vacuum seal. The air bubbles on the surface would pop from the change in pressure, thus expediting the vacuuming procedure. **Figure 12** shows three different TiO$_2$-PDMS samples in the vacuum chamber.

Figure 12: Three TiO$_2$-PDMS samples inside vacuum chamber.

If the PDMS were to cure completely with the air bubbles, there would be no possibility to fill them later on. Furthermore, these air pockets could cause data fluctuation and cause artifacts in the US images, since the acoustic impedance of air interferes with the US. Once the air bubbles were no longer visible in the plastic mold, the PDMS was baked for one hour in 60 to 65 Celsius degrees temperature. This temperature is high enough to expedite the curing process for PDMS but also low enough to prevent the plastic mold from melting. After one hour of baking, the PDMS cooled for an additional 10-15 minutes.

4.3.2.3 PDMS Samples

The first four PDMS samples were made with different ratios and ingredients as a preliminary test run. One of these samples contained TiO$_2$ (93% pure, not to be used in finalized samples) to familiarize the team with the process of incorporating TiO$_2$. This was done to experiment and determine what specific ratio was desired for the future testing protocols. In this initial test, the samples made included one sample with 10g monomer and 17% TiO$_2$ by volume, one sample with 20g monomer at a 10:1 curing ratio, one sample with 10g monomer at a 10:1 curing ratio, and one sample with 10g monomer at a 20:1 curing ratio. **Figure 13** below shows the four samples that were made and how they shaped around an arm.
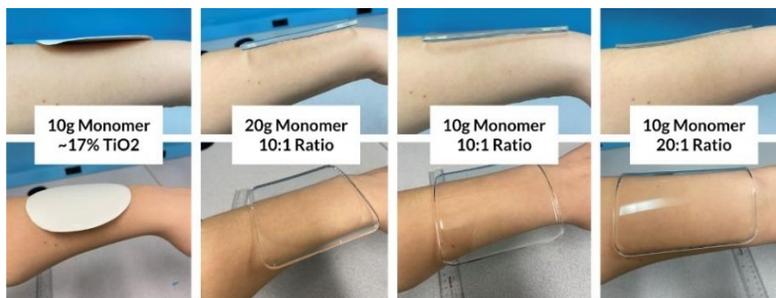
Figure 13: One TiO$_2$-PDMS sample (far left) and three PDMS samples at varying curing ratios.

The first round of PDMS provided insight into how the different elements of PDMS could be manipulated to give different properties. The three samples without TiO_2 gave the team a much better understanding of how different ratios worked when making the couplant. This can be seen in **Figure 13** when the different samples are positioned on the surface of the skin, arriving to a conclusion that the malleable properties are more visible when the ratio of the curing agent is lower (eg. 10:1 < 20:1). This is because a smaller amount of curing agent means less crosslinks will form, producing a less stiff sample. Moreover, homogenizing the TiO_2 within the PDMS was very difficult, as the viscous liquid form of the elastomer quickly turned dough-like from the particles. It could not be ensured that the TiO_2 was completely homogenized throughout each PDMS sample, since the mixing process was from the team's own manual mixing rather than a more standardized technology, which was not available. Furthermore, the manual, vigorous mixing to homogenize the TiO_2 caused more air bubbles to form. Consequently, the vacuum step took longer than it did in the normal PDMS samples.

The parameters for PDMS making in the subsequent trials were determined on several main principles. Firstly, the 20:1 ratio was found to be the most ideal since the PDMS followed the contour of the arm well. While 10g of base compared to 20g would produce a thinner and thus more flexible sample, it was decided that 20g of base would be better to use. When only 10g of elastomer was used with TiO_2, the mixture did not fill the square mold completely, as demonstrated by the circular shape. Therefore, 10g would not be enough base to account for the TiO_2. Since the concentration was in terms of volume, it made more sense for the team to set the total volume as the unchanged parameter, since the mass of the elastomer or TiO_2 would change depending on TiO_2 concentration. Additionally, this allows for thickness to be maintained between samples. For a sample to have 20g of base, the total volume would be 20.4 mL. The team rounded up the desired volume to 25 mL, to make sure there was enough base to saturate the TiO_2 particles even at high concentrations.

For the second trials of PDMS making, calculations were made to determine the exact amounts of TiO_2 that should be used in the PDMS samples. While the first sample with TiO_2 showed promise, it was difficult to determine the exact amount to use as the 7% of impurities seemed to vary the density. 99% pure TiO_2 (Fisher Scientific, MFCD00011269) was purchased to use instead of the initial 93% pure TiO_2 to make up for those inconsistencies. **Table 7** below depicts the five samples of 25 mL volume that were cultivated with varying volumes of silicone elastomer base and TiO_2, while the curing ratio was maintained at 20:1.

Table 7: Mass and volumes of TiO₂ and PDMS for five TiO₂-PDMS samples at varying concentrations.

		Density TiO2 (g/mL)		Density PDMS (g/mL)	
		4.26		0.982	
%Volume TiO2	Total Volume (mL)	Volume TiO2 (mL)	Mass TiO2 (g)	Volume PDMS (mL)	Mass PDMS (g)
15%	25	3.75	15.98	21.25	20.87
17.50%	25	4.38	18.64	20.63	20.25
20.00%	25	5.00	21.30	20.00	19.64
22.50%	25	5.63	23.96	19.38	19.03
25.00%	25	6.25	26.63	18.75	18.41

As demonstrated from the first trial of PDMS making, homogenizing the mixture was the most difficult part of the process. To counter this, the team agreed upon using a milk frother to

combine everything together. In doing so, the TiO$_2$-PDMS were well mixed together up until the 22.5% volume sample. From there on forward, the samples were mixed to the best of the team's abilities despite the milk frother overheating and shutting down. Another major point to note was the air pockets were successfully sucked out via the vacuum chamber but the sheer thickness and viscosity of the 22.5% and 25% TiO$_2$-PDMS samples still showed craters and bumps on the surface. This process was twice as long as the previous sample made due to the air pocket residues still existing. However, the air pockets or bumps were only towards the surface of the PDMS indicating that the vacuum chamber successfully worked slowly but gradually. **Figure 14** below shows three TiO$_2$-PDMS samples of increasing TiO$_2$ concentration, where the bumpiness dramatically increases at higher concentrations.

Figure 14: 20%, 22.5%, 25% TiO$_2$ (vol.) PDMS samples (left to right).

The 15%, 17.5%, 20%, 22.5%, and 25% TiO$_2$ by volume PDMS samples were imaged during the First Experimentation Phase, and it was decided that more samples should be made at lower concentration of TiO$_2$. The higher concentrations showed too much US wave interference, as the images did not visualize much. Consequently, new PDMS samples were made with 7.5%, 10%, or 12.5% TiO$_2$. This time around creating and mixing the particles were significantly easier due to the lower volume concentration of the TiO$_2$. **Figure 15** below shows the three new PDMS samples, along with the older samples created earlier on.
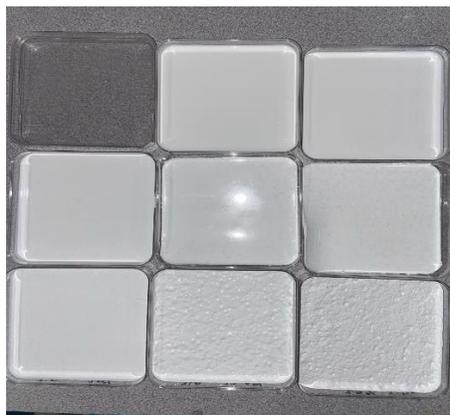
Figure 15: 0%, 7.5%, 10.5%, TiO$_2$ (vol.) PDMS samples (top left to right); 12.5%, 15%, 17.5%, TiO$_2$ (vol.) PDMS samples (middle left to right) and 20%, 22.5%, 25% TiO$_2$ (vol.) PDMS samples (bottom left to right).

As seen from **Figure 15**, the samples were more textured and less malleable as more TiO$_2$ was added. Reflecting back on all the procedures and creation of PDMS, the team concluded that the samples must have lower amounts of TiO$_2$ in order to have the desired acoustic properties as well to reduce the amount of inhomogeneity and texture, since air would fill these areas and cause interference. Once again, the team decided the concentrations tested should be decreased, after

imaging the samples through the Second Experimentation Phase. Therefore, 1%, 3%, and 5% TiO$_2$-PDMS samples were made. **Appendix C** shows a detailed table with all the measurements used to create TiO$_2$-PDMS samples ranging from 1-25% TiO$_2$ concentrations.

4.4 Experimental Set-Up

As demonstrated, the final design for the gel-free US imaging system consists of many different elements. Firstly, the US transducer is required to take images. The ball screw linear actuator with a NEMA 23 motor makes the vertical displacement of the US possible; this necessitates a power supply, an Arduino board, and a stepper motor driver. The entire system was decided to be kept fixed and stationary. A chemistry ring stand with clamps was used to hold the actuator in place in an upright position. This set-up is shown in Figure # below.
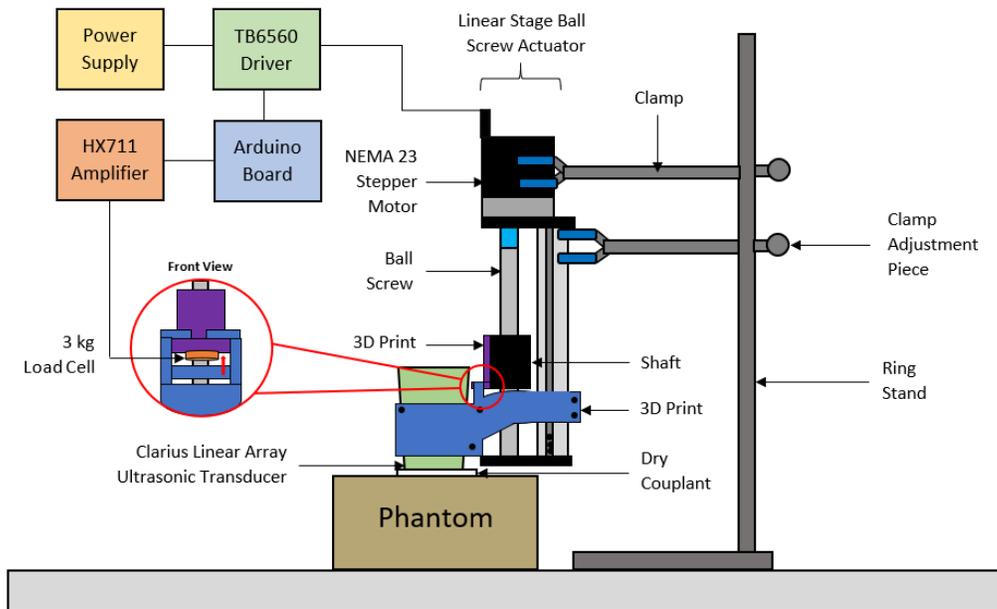
Figure 16: Experimental set-up of the actuated US transducer system for testing, fixed to a ring stand and positioned to image a phantom with a dry couplant replacing the topical gel (not drawn to scale).

As seen in **Figure 16**, the US transducer was fixed to the actuator by a rigid ring stand. In the diagram, the actuator is suspended in the air to compensate for the height of the phantom. However, an alternate approach is putting the ring stand at the edge of the table with the actuator not elevated. If the phantom is on a surface lower than the table, then the actuator would not need to be elevated. The dry couplant was placed on top of the phantom to replace topical gel. The load cell was secured to the 3D printed part (colored purple in **Figure 16**) on the underside so that when the US transducer presses down on a surface, the 3D printed part holding it (colored blue in **Figure 16**) will push up and hit the load cell. A photograph of the phantom used in this experimental set-up is shown in **Figure 17** on the next page.

Figure 17: CIRS General Purpose Phantom with targets of interest outlined in red box.

The red box in **Figure 17** indicates the section of the phantom that appears in the US image obtained. This requires a depth of 7 cm set in the Clarius program. The grayscale circles are structures that appear in the image acquired. The white smaller dots also appear. This phantom mimics tissues which allowed the team to get data with clinical relevance without needing to perform human testing.

4.5 Testing

In order to have an iterative process for this project, the team did not postpone testing until the system was completely assembled. Instead, experimentation occurred in three different phases throughout the project. The first and second experimentation phases helped to finalize the experimental set-up so that the main data collection could occur in the third phase. This section details the methods used in each of these three experimentation phases.

4.5.1 First Experimentation Phase

The first experimentation phase occurred during the last half of B Term. A main component of this phase of testing was demonstrating the difference between US imaging either with or without gel on the surface. Since this was very early on in the project, the team had not started assembling the device yet. Therefore, Dhirajsinh Deshmukh's device was used. This was a pneumatic actuated US transducer device, operated at a sonic frequency of 30 Hz, meaning the actuator both lifted and lowered the US transducer thirty times in one second. In **Figure 18** below, Dhirajsinh's system is shown imaging a CIRS Thyroid US Training Phantom.

Figure 18: Experimental setup for the preliminary testing on a CIRS Thyroid US Training Phantom using Dhirajsinh's pneumatic actuation system as part of the First Experimentation Phase.

The Clarius linear array US transducer used in the First Experimentation Phase was the same one used in the Second and Third Experimentation Phases that followed. It should be noted that the pneumatic actuation component of this testing mimicked what the team wanted to achieve with the proposed design of this project—a system that limits variable forces exerted by the human operator. Whereas the ball screw actuator system used the ring stand to keep the system stationary, the pneumatic actuator uses pressure to control the amount of force exerted, similar to what would have been achieved with Design #3 mentioned in the Preliminary Designs section of this paper. Therefore, when one of the team members started to push down the transducer onto the phantom, the system would correct the added force to ensure a constant force was applied to the phantom. All conclusions drawn from this preliminary testing were qualitative since signal processing codes were not complete yet.

Another important component of the First Experimentation Phase was the beginning of material testing. At this point, only the 15%, 17.5%, 20%, 22.5%, and 25% TiO_2-PDMS samples were made. When imaging these PDMS samples on top of the phantom, both with and without gel, the images were very low quality. None of the internal structures of the phantom were able to be visualized. Therefore, this experimentation phase is what led to the creation of 7.5%, 10%, and 12.5% TiO_2-PDMS samples to see if better images could be obtained. Similar to the pneumatic actuation tests, this material testing was all qualitative in nature, since signal processing was not doable yet. This phase concluded with *Gel Versus No Gel* testing, which repeated the same testing as mentioned previously but on a CIRS General Purpose Phantom. From this, the team had a positive control (with gel; best condition) and negative control (without gel; worst condition).

4.5.2 Second Experimentation Phase

During C Term, the Second Experimentation Phase took place. The main portion of this experimentation phase was to image all of the couplants and quantify image quality using the signal processing code. The materials imaged were the neoprene, nitrile rubber, and the 0%, 7.5%, 10%, 12.5%, 15%, 17.5%, 20%, 22.5%, and 25% TiO_2-PDMS samples. It was important that the acoustic properties were analyzed for all of the materials, especially for the TiO_2-PDMS samples since the concentration can have a dramatic affect on acoustic impedance. Therefore, to ensure that all image quality quantifications were purely based on the material properties and not confounding factors, the materials were imaged with gel, as shown in **Figure 19** below.
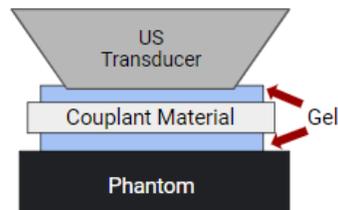
Figure 19: Set-up of couplant on a phantom for material testing.

Having gel layers between the couplant and both the transducer and phantom controlled for any air interference. Similar to the First Experimentation Phase, the team's device was not assembled yet. Therefore, Dhirajsinh's system was used again. However, an important difference for this testing was that a robotic arm was used to stabilize the transducer. Therefore, there was no variation in the orientation of the transducer relative to the phantom that would have been possible

during human operation. The actuation mechanism was not used in material testing, meaning the US transducer did not oscillate 0.5 mm up and down; rather, the arm lowered the transducer until 5 N of force was applied on the phantom. Also, a different phantom was used, called the CIRS General Purpose US Phantom. The set-up for material testing during the Second Experimentation Phase is shown in **Figure 20** below.

Figure 20: Experimental set-up for material testing in the Second Experimentation Phase, using a pneumatic system with the Clarius US transducer.

Qualitative analysis of the images during data collection led the team to attempt even lower concentrations for TiO_2-PDMS. Even though the 7.5%, 10%, and 12.5% samples were made after the First Experimentation Phase, the results from the Second Experimentation Phase suggested the concentrations could be lowered. Therefore, the team manufactured 1%, 3%, and 5% TiO_2-PDMS samples and then imaged those samples using the same process as previously mentioned. The images from all these material testing trials, including those with the new 1%, 3%, and 5% TiO_2-PDMS samples, were analyzed using signal processing methods, shown in **4.6 Signal Processing**.

4.5.3 Third Experimentation Phase

The Third Experimentation Phase occurred during D Term and resulted in data most important to the project outcomes. By this point, the team's system was completely assembled. The Arduino code was completely functional. The actuator lowered until the US transducer exerted 5 N of force on the CIRS General Purpose US Phantom. Once 5 N was reached, the actuator would lift the transducer up and down 0.5mm at a frequency of either 6 Hz or 14 Hz. In order to achieve the optimal number of images (at least 900), the oscillation motion of the US transducer would take place over one minute. The experimental set-up for data collection in this Third Experimentation Phase is shown in **Figure 21** below.
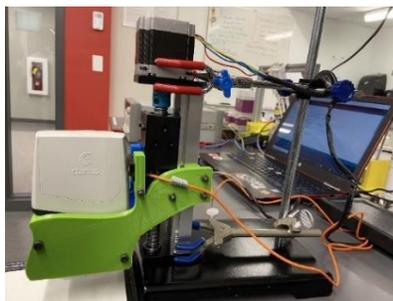
Figure 21: Experimental set-up for frequency testing the Third Experimentation Phase, using the actuated US transducer system designed in the project.

Seeing the 0% TiO$_2$-PDMS sample was determined to be the most ideal (see **5.0 Results**), this was the couplant used in the Third Experimentation Phase. Four different parameters were tested: with actuation, without actuation, with gel, and without gel. Actuation indicates either 6 Hz or 14 Hz. The four possible trials are shown in **Table 8** below.

Table 8: Experimental conditions for the third experimentation phase.

	With Gel	**Without Gel**
With Actuation (6 or 14 Hz)	With actuation, with gel	With actuation, without gel
Without Actuation (0 Hz)	Without actuation, with gel	Without actuation, without gen

For the 0 Hz actuation trial, the actuator would lower the US transducer until 5 N was exerted, just like it would in the actuation trials. The only difference for this trial was that there was no oscillation of the probe. It should be noted that the **Table 8** experimental conditions were repeated for multiple scenarios, for example one round with PDMS and one round without PDMS for both 6 Hz and 14 Hz. In total, twelve trials were performed, all utilizing the 0% TiO$_2$-PDMS sample:

1. No PDMS, gel **(positive control)**
2. No PDMS, no gel **(negative control)**
3. PDMS, gel
4. PDMS, no gel
5. No PDMS, no gel, 6 Hz actuation
6. No PDMS, gel, 6 Hz actuation
7. PDMS, no gel, 6 Hz actuation
8. PDMS, gel, 6 Hz actuation
9. No PDMS, no gel, 14 Hz actuation
10. No PDMS, gel, 14 Hz actuation
11. PDMS, no gel, 14 Hz actuation
12. PDMS, gel, 14 Hz actuation

The images from each of the twelve trials were processed using the signal processing methods detailed in **4.6 Signal Processing**. From the Third Experimentation Phase, which was the final round of data collection, major conclusions were drawn for the project.

4.6 Signal Processing

This section details the design process of each of the image processing techniques used to quantify image quality. Some examples of methods discussed include image display, image resizing and definitions of regions of interest, various analysis techniques, image registration, a function to vectorize images, and a function that processes multiple images at a time. The methods of quantification of the results such as mean, standard deviation, and box and whisker plots, hypothesis testing, are discussed as well. All of this is done through coding developed using

MATLAB software. These codes will be thoroughly discussed throughout this section and their correlated written codes can be found in **Appendix D.**

4.6.1 Design Process

To conduct signal processing on the collected experimental data, several different signal processing tools were constructed. These tools were created using the program MATLAB. The literature used to develop the signal processing codes was mainly MathWorks, which outlines the different functionalities that MATLAB has. It was also developed to align with current literature in the field of Signal Processing, specifically the published work "Image Quality Evaluation of US Imaging Systems (Sassaroli et al., 2019). The MATLAB codes presented in this section are the entirety of fully developed and finalized MATLAB codes. Not all were used in the final analysis of experimental data, however this shows the entire development of signal processing throughout the entirety of the project. Some smaller codes were left out due to their insignificance. **4.6.2 Processing of Data using Signal Processing Pipeline** presents the finalized process of conducting signal processing on experimental data and which codes were ultimately used.

4.6.1.1 Image Resizing and Definition of Regions of Interest

The next code written was designed to resize an image. The development of this code arose from a desire to investigate the industry standard reference image for the imaging surface. A reference image is the optimal quality that should be obtained from the object being imaged. Specific to the experimental configuration of this project, the reference image came from imaging the phantom with gel on the surface. Based upon the phantom and the reference image, it allows for quality comparison of acquired images. This is made possible due to established parameters/ characteristics of the phantom. For this study, the phantom used was a CIRS General Purpose US Phantom, model 054GS.

The phantom has set specifications due to the manufacturing of the imaging material. The General Purpose US Phantom is composed of Zerdine® which is a hydrogel polymer. It has gray scale and sensitivity targets at different depths within the Zerdine®. For this phantom, CIRS provides a reference image of what the targets all look like when penetrated by a signal going to the full depth of the phantom. It was established through this study that use of the provided "industry standard" reference image would not be the same size image as that acquired during experimentation. This necessitated the development of a code which could resize an image and align it to the size of the other images being analyzed ("General Purpose US Phantom," n.d.).

It was important to find a solution to resize the reference image because otherwise, MATLAB would not be able to compare it to the collected data. When beginning to investigate writing this code, the team encountered difficulties with determining the size of the array needed. The following questions were asked:

- "What size should the image be?"
- "How do we find the size of our other images?"
- "Are all the images the same size?"
- "What is the best methodology for resizing the image?"

In order to answer these questions, different MATLAB tools available in the toolbox had to be researched. Consequently, the starting point to resize was determined as the ability to crop

images. In order to achieve this, the specifications (height and width of array, number of pixels, pixel type, etc.) of the collected images had to be determined. With the necessary details defined, the code was written to utilize the function imcrop, which cropped the image and then used it for comparison. However, after receiving feedback on the code, it was concluded that the "imresize" function would be more suitable. Therefore, this function was implemented in the final iteration of the code.

The final resizing code written resizes image A to be the same specifications as image B. In the analysis, image A is the reference image, and image B is the image of interest or the experimental image. The code functions by initially reading the images. Again, the image was read as grayscale because that aligns with the format that was determined that all data should be in. After the image is read and stored as variables, the size of the images is then found. Along with the size of the image, the code also specifically outputs the height and width of each image for easy identification. The reference image, or image A, is then resized to the size of the experimental image, image B. This is done utilizing the function "imresize". The two images are then displayed on a figure to give a visual representation of how image A was resized. This allows for it to clearly show that both images are now the same size.

Once the images were resized, a portion of code that Professor Lammert shared was utilized, which defined the regions of interest (ROI) were define in the images. The importance of ROI was made most apparent from the research paper: "Image quality evaluation of US imaging systems: advanced B-modes" (Sassaroli, 2019) as well as upon discussions with Professor Lammert. The ROI is useful for future analysis because this will define the pertinent regions of the image that are necessary for certain characteristics of the image to be found and compared.

The first step to this process is to define the target and background of the image. The target is the specific piece of the image that is ideally going to be found or displayed. The background is the negative space of the image, which ideally would be black for this project. Once these areas are defined, the region will be isolated with a circle, where the radius could be altered based upon the image being used. These regions are then used to define what the region of interest is and subsequently plot a figure. This figure will display the original image, an image where the target region is shown, and an image where the background region is shown. Again, these regions can be changed based upon the image being utilized. Lastly, it will display the mean and standard deviation of each region. This is useful when comparing images to see if they have similar pixel values, thus being of similar quality.

4.6.1.2 Vectorizing Code

The purpose of the vectorizing code is to provide an efficient way to process many images at a time without taking a significant amount of time. In order to run the code, the name of the folder with the images of interest is required as well as the name of the desired name of the new file that the vectorized images will be placed in after the code is run. The code automatically goes through each image one by one in the folder and resizes each one into a vector that is written into a new file for the user. In the file, one image corresponds to one row; for example, if there are four images, there will be four rows present in the file. The file containing the vectorized images acts as the input into the following code used to calculate the metrics, where it would then be fully processed. The metrics code will be further discussed in depth in the following section.

4.6.1.3 Metrics Computer

The next step in the code development was to formalize what characteristics would be useful to analyze for comparison between images. This investigation commenced with reviewing the research paper "Image quality evaluation of US imaging systems: advanced B-modes" (Sassaroli, 2019). This paper gave a great insight into the way in which values can be used to compare images and obtain the quality of images. Consequently, some of the tools that could be used as characteristics to compare images were identified.

Three main metrics were identified to be included in the analysis of the images. The first metric was the mean square error (MSE). This would allow for MATLAB to take two images and filter pixel by pixel, finding the difference between them and squaring the value, then taking the overall average. It was then determined that 2D correlation should be found within the image to account for any potential differences between images. It functions by registering the image of interest and then outputting a correlation metric. If the correlation were found to be zero, that would indicate that there was no relationship—it was purely linear. The peak signal to noise ratio (PSNR) was identified to be immensely useful in analysis because it measures the peak error of the image. The PSNR is calculated for a desired image in comparison to the reference image. It is depicted in decibels within MATLAB giving a scalar value in type double (Psnr, 2020). The MSE along with the PSNR can be used to compare the image of interest to the reference image and assess their quality (Psnr, 2020). The final metric identified was the structural similarity index (SSIM) of the image. The SSIM compares an image of interest to a reference image and computes a metric to show the image quality degradation. This is done in a grayscale image.

The code for analysis begins by using the function 'imreconfig' which creates both an optimizer and a metric configuration. There is then a for loop within the code which will continually process for each image in the designated folder being processed. The for loop begins by registering each image. This is done using the computed optimizer and metric configuration and a reference image, as inputs to the MATLAB function 'imregister'. The next step is for the metrics MSE, PSNR and SSIM to be computed for each image. A table is created with this data. Once this is completed the processing then goes onto calculating the mean and standard deviation for each metric. These values are then also displayed within tables for convenient data interpretation.

4.6.1.4 Statistical Analysis

To begin quantifying the experimental metric, both the mean and standard deviation of each signal processing technique for each image was determined. The mean value for each metric allows for a clear depiction of what the average value for that metric was for each experimental condition. This will allow the metrics to be compared for each experimental condition as an average as opposed to individual data points. The mean metric values will also be statistically analyzed as discussed in the subsequent section in order to draw conclusions between experimental conditions. The standard deviations go along with the means computed to see the variability and spread of the data compared to the mean. It shows whether the mean calculated is an accurate representation of the data set analyzed. In other words, if the standard deviation is very large it would show that the mean is not an accurate representation for the experimental condition as a whole. In addition to calculating the mean and standard deviation of each experimental condition, other statistical analysis was performed. The team first approached the statistical analysis through

conducting a paired t-test along with a box and whiskers plot. The goal of these statistical tests will be discussed in the following sections. However, after careful consideration it was determined that these hypothesis tests were not accurate for our datasets. A t-test is applicable for data that is of a normal distribution whereas our data was nonparametric. This fact was found using the MATLAB function 'histfit'. An example of this can be seen in **Appendix E**. This led to the decision to conduct a Wilcoxon Rank Sum test then Kruskal Wallis test and lastly, a pairwise comparison. All these statistical analysis methods will now be presented.

T-test Hypothesis Testing

A statistical analysis, t-test, is useful for identifying trends in experimental data and determining if the results are statistically significant. Moreover, hypothesis testing is used to determine whether the results show an experimental conclusion or if they can be attributed to chance. In the context of this project the t-test would be conducted with two sample groups. For example, it could be the conditions: "gel" versus "no gel". For the gel condition, a phantom would be imaged with topical gel on the surface, acting as a control condition since it is the closest to current imaging practices. No gel would mean the imaging of a phantom without the use of a topical gel. Because the aim of this project is to demonstrate the differences between gel and no gel imaging conditions, the null hypothesis would be: "If gel is used on the surface of the phantom during image acquisition, then it will produce higher quality images than those acquired without gel." The power and significance level of the test must be defined based upon the experimental conditions. The statistical analysis will then ensue with the use of the experimental data. Both the test statistics and p-value will then be calculated using MATLAB, which signifies how likely the null hypothesis is to be true based on the observed data. With these results, it will be able to be determined whether the null hypothesis can be accepted or rejected, showing whether the data is consistent or inconsistent (Ilakovac, 2020).

When making conclusions based upon statistical analysis, it is important to be aware of the errors that can arise. The two errors that can occur are Type I and Type II errors. A Type I error is what can be deemed as a false positive, detecting an effect that is not necessarily present. It is the incorrect rejection of the true null hypothesis. A Type II error can be referred to as a false negative, failing to detect an effect that is present. It is the failure to reject a false null hypothesis. A Type I error is typically called alpha (α) and a Type II error is typically called beta (β). The alpha, or significance level, is set before testing and is commonly either 0.05 or 0.01. The p-value found during statistical testing will be compared to the alpha to determine whether the data is statistically significant (Ilakovac, 2020). If the significance level is set to 0.05 and the p-value is less than 0.05 it would result in rejecting the null hypothesis and accepting the alternative hypothesis. If the p-value were greater than or equal to 0.05 than the null hypothesis would be retained (du Prel et al., 2010). The beta value is dependent on the size of the effect, sample size and the established significance level (Ilakovac, 2020). The beta value is equal to one minus the set power value. The power being predetermined and dependent on sample size and other factors. The power is typically chosen to be 80% in statistical analysis (du Prel et al., 2010). This means that the condition would have a probability of happening less than 20% of the time.

The last piece of hypothesis testing that was defined was the form of statistical test that was to be conducted during analysis. The test was identified as a two sample, one tailed t-test for the analysis. A two sample, also referred to as an independent, t-test was chosen for all experimental testing because all comparisons being made always have data independent of each

other; there was no expectation that any conditions would be assumed to be similar to each other. A one tailed t-test was chosen because they would result in a confidence in the data tending toward one direction. With the nature of this experiment, the one tailed test will dictate whether the population means are greater or less than the other (du Prel et al., 2010). This is why a two sample one tailed t-test was performed for statistical analysis.

In the code developed it begins by inputting the matrices of each metric metric (MSE, PSNR and SSIM) from the two experimental conditions into the workspace. They are then analyzed using the 'ttest2' MATLAB function. This will then output a p and h value for each metric. Conclusions based upon the dataset and null hypothesis can then be made.

Box and Whiskers Plot

To further analyze the experimental data in addition to the statistical t-test, a box and whiskers plot code was developed. A box and whiskers plot is a wonderful way of visually representing a large amount of data and depicting how the entire data set behaves. The structure of a box and whiskers plot consists of three essential components. The first to highlight is the "box", which shows the interquartile range of the data. This means the middle fifty percent of the data set. The median will be represented by the solid line in the middle of the "box" on the plot. The "whiskers" which come out of either end of the "box" show the twenty five percent of the data on either side of the interquartile range. These "whiskers" will not include outliers (Larsen, 1985).

For this box and whiskers plot, a box chart was utilized due to its unique visualization capabilities. This is a specific tool that MATLAB can output once the data metrics are analyzed. One of the unique features is that the box will have notches surrounding the mean of the dataset. When comparing two different data sets, the notches allow for one to interpret with 5% confidence whether the true means of the data sets differ. For example, if two data sets are plotted on the same box and whiskers graph and their notches do not overlap, then it can be said with 5% confidence that the true means of the two data sets differ. To further accentuate the notches to interpret this "overlap", each "box's" notched region will appear in light blue ("Boxplot", n.d.).

When interpreting the plot, it is important to analyze its unique features. The median line is within the "box". This is a visual way of seeing whether the median accurately represents the entire data set. For instance, if the median is exactly in the middle of the "box" then it would show an accurate representation of the mean. However, if the median line is closer to an end of the "box", then that could draw the conclusion that there was variability within the data set, and the median may not be an accurate representation of the mean. Comparing the means and notches allow for a form of visual hypothesis testing. This adds to the robustness of the experiment's statistical analysis ("Boxplot", n.d.).

Wilcoxon Rank Sum Test

As previously mentioned, the Wilcoxon Rank-Sum test was chosen instead of the t-tests due to the nature of the distribution of our datasets which are nonparametric. The purpose of a Wilcoxon Rank-Sum test is to determine if two samples, which in our case would be two datasets, are from the same distribution, using the medians instead of means for both populations (LaMorte, MD, PhD, MPH, 2017). The null hypothesis of this test states that the two samples are the same

while the alternative hypothesis states the opposite (LaMorte, MD, PhD, MPH, 2017). It is assumed that the samples being tested against each other are independent (Mathworks, 2021).

The goal of this test for our project is to prove a statistical difference between all of our conditions tested and the gel reference condition. In order to claim that there is a difference between the materials, a h-value of 1, which is true, would be needed as well as a p-value that is zero if not close to zero. This allows the null hypothesis stating that they are equal to be rejected, and the alternative hypothesis stating that they are different to be accepted.

Kruskal Wallis Test

Due to the nonparametric distribution of the datasets, a Kruskal Wallis statistical test was also developed (see **Appendix E** for an example of the experimental nonparametric distribution). The purpose of a Kruskal Wallis test is to perform a multiple comparison of multiple experimental conditions to see if they come from the same distribution. It is useful for comparing different conditions and that is another reason why it was appealing for this project's statistical analysis. For this hypothesis test, the null hypothesis is all condition medians are equal and the alternative hypothesis is that at least one of the condition's medians is different from at least one of the other conditions (Kruskalwallis, 2021).

To perform this statistical analysis, the MATLAB function 'kruskalwallis' was used. This function returns the p-value of the null hypothesis, showing whether the data comes from the same distribution. It also returns an ANOVA table which has the STATS values, the test results, and a box plot of the data. From the ANOVA table it was determined that the most relevant value to focus on was the Chi Square. This is because the larger the value, the more correlation there is between the datasets and the smaller it is, the more distribution there is between the datasets. The box plot is also very useful for seeing each condition's distribution and mean comparatively as previously discussed in **Box and Whiskers Plot** (Kruskalwallis, 2021).

It was then determined that a pairwise comparison would be useful to see the distribution between conditions when compared to each other. To conduct this statistical analysis the MATLAB function 'multcompare' was used. This requires the input of STATS which is obtained from the kruskal wallis test. It will then produce a graph of the comparison of all conditions based on their mean ranks. Each condition is represented by a line with a symbol in the middle. If the condition's line is in the same interval as another condition, it can be concluded to be comparable and if not, it is significantly different. It is an interactive graph meaning the different conditions can be clicked on and the statistical outcome of comparability will be clear with the use of color changes. This test will also produce a variable that holds the multcompare values in a matrix of 6 columns. The first two columns contain the conditions that are being compared. The third is the lower limit for the 95% confidence interval for the true mean difference. The fourth is the difference of the estimated group means. The fifth is the upper limit for the 95% confidence interval for the true mean difference. Lastly, the sixth is the p-value for a hypothesis test corresponding with a mean difference of zero. If all p-values are small it shows that the conditions differ (Kruskalwallis, 2021).

This code begins by the user inputting all of the conditions that are desired to be compared. These should be done by metric. In our datasets, all of our metrics were rows and for this function it is necessary for them to be columns. This resulted in the function 'transpose' to be used to make

all conditions columns. These columns were then translated into a matrix as a single variable. The function 'kruskalwallis' was then performed on that variable. This resulted in the outputs as previously discussed. Once all of the outputs were saved, then the pairwise comparison using the function 'multcompare' was performed. This again was performed with the input of STATS which was produced by the Kruskal Wallis Test. 'Multcompare' then produced the outputs as discussed above and those were also saved. That concluded the multi comparison and pairwise comparison hypothesis testing using the Kruskal Wallis test and 'multcompare (Kruskalwallis, 2021).

4.6.1.5 Image Display

The first code written was a display/ formatting code. This code was used to easily depict images or graphs that were desired to be compared or displayed. It allowed for easy identification of differences and the presentation of data sets. The purpose of this code is to display four images on one figure in a polished format.

The code begins by reading an image to grayscale. The purpose of this is to convert the data values/ pixels into a matrix of values based upon pixel intensity. In a grayscale image, the smallest values correspond to the color black while the largest represent the color white. These values will be depicted in the format of uint8, resulting in the values having a lower limit of zero (pure black) and an upper limit of 255 (pure white) ("Image types in the toolbox," n.d.).

Once the pixels are read to grayscale and placed within a matrix, they are then configured and positioned within the figure based upon the input order. If this is desired to be changed, all the user must do is alter the placement of each image within the code. The standard format is where the first image entered will appear in the upper left, the second image will appear in the upper right, the third image will appear in the lower left, the fourth image will appear in the lower right. It will also be important, based on what is being shown, to correlate the title within the code, to the image being displayed. If a reference image is used, this is also an important indication to make within titling.

There was not a significant amount of iteration done on this code. Being a straightforward image display code, it required basic MATLAB skills. Therefore, it did not necessitate an extensive amount of ideation.

4.6.2 Data Processing with Signal Processing Pipeline

By the end of the project when processing the data for the final time, the signal processing pipeline was finalized. This was a long process and essentially took the entirety of the project to complete. It was an iterative process of continually adding and narrowing down the way in which the team wanted the data to be analyzed and presented. The steps to process the data along with the functions used will not be discussed.

To begin, it was essential to outline all experimental conditions datasets and how they were desired to be processed. If datasets were not saved in an appropriate manner, it could cause signal processing to be difficult. In these datasets, it was important to identify the number of images being analyzed. In order to perform proper analysis, all datasets need the same quantity of data points (images). Initially, the team was processing close to 1000 images in order to achieve statistically significant and conclusive data. However, as time to process got shorter and the confidence in the

experimental results got higher, it was decided to process the first 10% of images collected, meaning the first 100 images.

Once all data was appropriately organized the processing could begin. To begin processing, the Vectorizer function was utilized, which vectorized all 100 images into a .mat file. This file would then be saved. This was done for all conditions. Then, the Metrics Computer Function was run. This required the input of the .mat file of the reference dataset and the .mat file of the condition being compared. This was done for every metric and resulted in the metrics, means of the metrics, and standard deviations of the metrics, all of which were saved. Once all conditions were run through the metrics, the statistical analysis was then performed, beginning with the Wilcoxon Rank Sum test. The Wilcoxon Rank Sum test required the inputs of each metric .mat file from the reference dataset and a condition's dataset. This then produced the p and h values for each metric, which were saved. Then, STAT for all three metrics was computed. This returned the zval (z-statistic) and the rank sum test statistic. Once this test was completed, the Kruskal Wallis test was then conducted as a comparison of any conditions that were desired to be compared. This required the input .mat matrices of the metric which were then put into a matrix and then imputed into the function 'kruskalwallis'. This resulted in the outputs as discussed above: p-value, ANOVA table, STATS and a boxplot, all of which were saved. The pairwise comparison of the STATS was then conducted using 'multcompare. This produced the multiple comparison based on mean rank graph and the Z multcompare values as discussed above. These outputs were also saved. All outputted data was saved throughout the entirety of processing.

That concludes the sequential order in which signal processing was conducted on all experimental data. From this data, conclusions and interpretations of the data were made in order to formulate the project's final results.

4.6.3 Verification of Algorithms

To write each desired algorithm, the team had to go through many iterations of debugging and testing to investigate each code's functionality. The first round of testing was performed using two small folders, each containing four images, representing two different conditions. Testing was then completed using folders with a higher quantity of images. If the function ran properly and provided the table with each metric, the standard deviations, the means, the hypothesis testing, and the box plots, then the test was concluded to have passed.

Due to the timeframe needed for processing to be completed, we updated our algorithms to no longer reflect functions in order to conduct processing in a timely fashion. The updated code was tested with larger datasets of 909 images, which was proven to still take a large amount of time to process. Since our previous results using our function with a dataset of 100 images produced viable results, we decided to run our updated code with datasets of 100 images each. At the stage of statistical analysis for frequency testing, we found that the PSNR values for hypothesis testing were both "NaN" due to a possible value of infinity in the file holding the values of the metric for PSNR. In order to fix this issue, we applied the "isinf" function in MATLAB to filter out the infinity values if any were to be present, which resolved our issue of "NaN" in hypothesis testing values for PSNR.

After some thought and consideration of our methods for statistical analysis, a decision was made to use Wilcoxon Rank-Sum tests, Kruskal Wallis, and pairwise comparison instead of

hypothesis testing and boxplots alone because of nonparametric distribution in our datasets. The code was also troubleshot with the aid of Professor Lammert. Periodic meetings were set throughout the development of the signal processing to discuss new techniques that could be applied to improve the algorithm.

5.0 RESULTS

This section provides the project's results, both quantitative and qualitative. The qualitative results focus on the design process of the actuated US transducer system along with the visual comparison of images acquired during experimentation. The quantitative results present the metric calculations and statistical analysis of all experimental conditions. Both the qualitative and quantitative results present a complete picture of the project's findings and what conclusions were able to be drawn.

5.1 Qualitative Results

The qualitative results of this project were crucial in the progression of the project along with the corroboration of quantitative results. The qualitative results were found during experimentation and through the visual comparison of images acquired. These results will now be presented in the following sections.

5.1.1 Experimental Qualitative Findings

In each of the three major stages of experimentation—*With Gel Versus Without Gel* testing, *Material* testing, and *Frequency* testing—qualitative analysis was used to progress the project prior to quantitative analysis. If there was an issue identified qualitatively during experimentation, the team would try to resolve the issue as soon as possible, often before all quantitative analysis could be performed. These major findings are as follows: **In the *With Gel Versus Without Gel* testing**, there were no significant qualitative findings. **In the *Material* testing**, the major qualitative finding pertained to the functionality of the PDMS samples. It was observed that all PDMS samples with high concentrations of TiO_2 were not producing quality images. Therefore, the team decided to make lower concentration TiO_2-PDMS samples. Then, the new TiO_2-PDMS samples were imaged and found to produce low quality images as well. This resulted in the team making the final iteration of PDMS samples with TiO_2 concentrations of 1%, 3%, and 5%. If the team had not used these qualitative findings from imaging, it would have likely resulted in the lower concentrations never being made. **In the *Frequency* testing**, the team observed several issues with the actuated system, the first being issues with the calibration of the load cell. These issues were quickly resolved. The next issue pertained to the experimental setup. As the actuator would translate the transducer, the force it created caused the ring stand to displace and the system to become shaky. The team resolved this by applying manual stabilization of the ring stand and actuator to inhibit movement. These major qualitative findings were pivotal in the team being able to produce all subsequent qualitative and quantitative results.

5.1.2 Visual Comparison of Images

The following section will discuss the visual qualitative comparisons of the experimental testing and what was found in each major experimental phase. An important note is that all images displayed were acquired during *Frequency* testing, where the CIRS General Purpose Phantom was imaged at a depth of 7 cm. All images are still applicable to the conclusions drawn from the

different stages of experimental testing. The purpose for this choice in image display is because in both *With Gel Versus Without Gel* and *Material* testing, the images acquired were square in composition. The *Frequency* testing images were a fan shaped composition, as is typical of US images. In order to make all the qualitative comparisons consistent, it was chosen to display the *Frequency* testing images. Again, it is important to emphasize that the same results found within this analysis were also found within the square shaped images of *With Gel Versus Without Gel* and *Material* testing as well. This choice of visual display is for consistency purposes.

5.1.2.1 Ultrasound Imaging Comparisons

The goal of the US images is to demonstrate the effect that gel has during imaging. A good quality image would depict the five grayscale targets of the phantom, which are essentially five circles of different darkness lined up side-by-side in the image. These targets can be seen clearly in the first image on the left of **Figure 22** below, corresponding to the positive control - *no PDMS, with gel*.
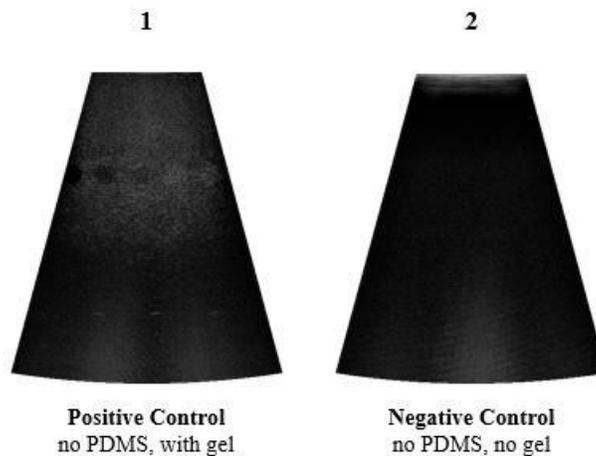
Figure 22: US imaging comparison with gel versus without gel.

Evidently, in the rightmost image in **Figure 22**, the negative control - *no PDMS, no gel*, the grayscale targets cannot be seen at all. The image is predominantly black. This is because without the use of the topical gel there is no way for the US waves to propagate and produce an image of the internal structures of the phantom. This comparison shows that the *positive control* produces an image of much higher quality than the *negative control*. This validates the decision to use the *positive control* as the highest quality image comparison and the *negative control* as the worst quality image comparison. These images form the bounds of a spectrum of image quality, in which all subsequent imaging can be qualitatively and quantitatively compared to.

It should also be noted that the negative control - *no PDMS, no gel* shown is in fact the experimental condition of *14 Hz actuation, no PDMS, no gel*, meaning the actuation mechanism of the system was turned on for this trial. This condition was intended to be the *no actuation, no PDMS, no gel* condition. However, due to inconsistencies in the images acquired during frequency testing, it would have resulted in inaccurate visual comparisons. This resulted in the need for an alternative *negative control* for visual comparison. The condition that was closest to the *negative control* was the *14 Hz actuation, no PDMS, no gel* condition. The rationale for this condition being

44

the closest to the *negative control* will be further supported in **5.2.3 Frequency Testing**. That is why this condition is presented as the *negative control* for all qualitative analysis.

5.1.2.2 Material Testing

In the *Material* testing, the team imaged neoprene, nitrile rubber, PDMS, and varying concentrations of TiO$_2$-PDMS. The details of this testing are laid out in **4.5.2 Second Experimentation Phase**. **Figure 23** below shows a visual comparison of the effect PDMS as a couplant had during imaging.
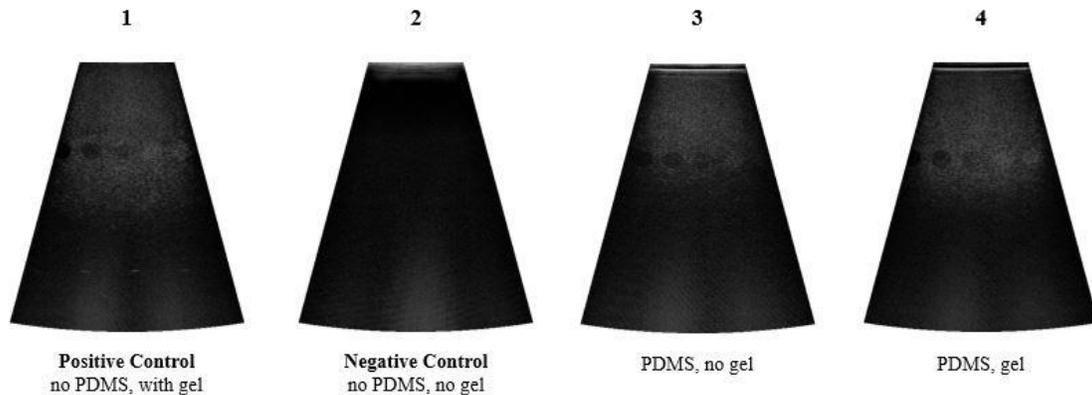
Figure 23: *US imaging comparison showing the effect of PDMS.*

From left to right, the order of images are as follows: the first image is the *positive control*, the second image is the *negative control*, the third image is imaging *with PDMS without gel*, and the fourth image is *imaging with PDMS with gel*. This condition was chosen to be the *positive control* due to it being the experimental equivalent to current medical US imaging practices. The rationale for the *positive* and *negative controls* can be referenced in **5.1.2.1 US Imaging Comparisons**. The goal of this comparison is to visually demonstrate the validity of using PDMS as a replacement to topical gel through qualitative analysis.

In the *positive control* condition, five circles of varying contrast are clearly visible. These are the five grayscale targets of the CIRS General Purpose Phantom. The purpose of these targets is to allow for the visual quantification of image quality. As expected, the *positive control* is the highest quality, showing all five of the grayscale targets most clearly compared to the other images. Evidently, the *negative control* is predominantly black, not showing the grayscale targets. This is to be expected in a n*egative control* condition, seeing as it should be of the worst quality. The third and fourth image in **Figure 23** are closer in clarity to the *positive control* than the *negative control*. However, it is apparent that the fourth image is of slightly better quality than the third. In the rightmost side of the fourth image, it shows the fourth and fifth grayscale targets (white) in greater detail than in the third image. Those are the most important points in the visual comparison between these conditions. Furthermore, it should also be explicitly discussed why there is a white line at the top of the third and fourth image in **Figure 23**—this is the PDMS. The reason the PDMS is visible as a white line in the third and fourth images while nothing is at the top of the *positive control* is because topical gel has optimal acoustic properties relative to tissues. PDMS has a slight

discrepancy in acoustic properties, as discussed in the creation of the material. Therefore, there is an acoustic mismatch that causes the US wave to partially reflect, producing a white line.

From this qualitative analysis, it can be concluded that the third and fourth images of **Figure 23** are of comparable quality to the *positive control*. This demonstrates that PDMS, when used as a couplant, can produce high quality images. The influence of gel should also be discussed in this visual comparison. Seeing as the fourth image is slightly more comparable to the *positive control* than the third, that would lead to the conclusion that the use of *gel and PDMS* is a better experimental condition than *no gel and PDMS*. However, there is a discrepancy in this conclusion. Through quantitative analysis it was determined through metric calculations and statistical analysis, that *no gel and PDMS* was in fact the better experimental condition. This was an inconsistency that was not expected and will be further discussed in section **5.2.3 Frequency Testing** as to what the project's final conclusion is. From a purely qualitative analysis, it is shown that *no actuation, with PDMS, with ge*l is the optimal experimental condition, as it is the most comparable to the *positive control*.

5.1.2.3 Frequency Testing

In the *Frequency* testing, US images were taken with the experimental set-up of the designed actuated US transducer system. The US transducer was lowered to apply a force of 5 N on the phantom, and then it oscillated from that position at a sonic frequency of either 6 Hz or 14 Hz, at a distance of 0.5 mm up or down. Other trials in *Frequency* testing operated at 0 Hz, meaning there was no oscillation (no actuation). **Figure 24** below, is a visual representation comparing the three frequency conditions of interest to the *positive* and *negative controls*.
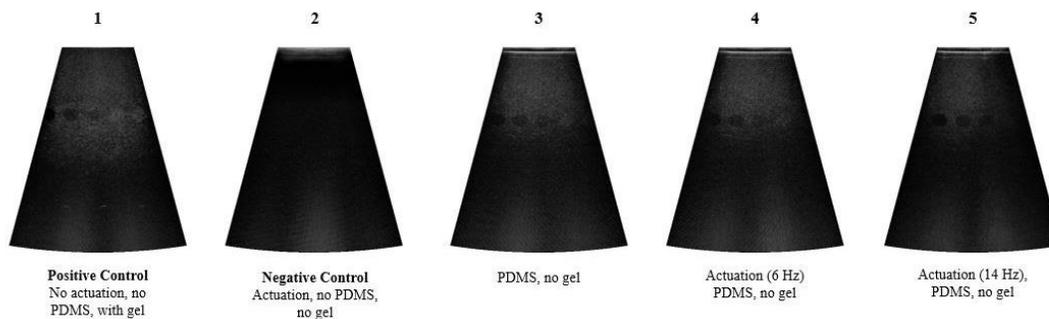
Figure 24: US imaging comparison showing the effect of actuation.

From left to right of **Figure 24**, the order of images are as follows: the first image is the *positive control*, the second image is the *negative control*, the third image is imaging *with PDMS without gel*, the fourth image is *imaging with an actuation frequency of 6 Hz with PDMS with gel*, and the fifth image is *imaging with an actuation frequency of 14 Hz with PDMS with gel*. The rationale for the *positive* and *negative controls* can be referenced in **5.1.2.1 US Imaging Comparisons**. The goal of this comparison is to visually demonstrate the effect that actuation at different frequencies had during imaging. The condition of *PDMS, no gel* is being used for comparison because it was found to be the best experimental condition through quantitative analysis, which will be further discussed in **5.2.3 Frequency Testing**.

Between the *positive* and *negative controls*, the *negative control* has the worst image quality when compared to the *positive control* and the rest of the conditions. In the *negative*

control, you cannot see any grayscale targets while in the *positive control* you can see about five grayscale targets, as expected. The three conditions of interest compared to both controls include *PDMS without actuation or gel*, *actuation at 6 Hz with PDMS and no gel*, and *actuation at 14 Hz with PDMS and no gel*. All three conditions of interest are similar overall in image quality. If you look at **Figure 24**, in the images labelled three, four, and five, you can see about three to four grayscale targets in each of them, which is comparable to the *positive control* having five grayscale targets. The condition *with actuation at 14 Hz, couplant, and no gel*, image five, is slightly worse than image four, which is at *6 Hz*. This demonstrates that *6 Hz* actuation produces a better image. A close look will show there are four grayscale targets in images three and four and only about three distinct grayscale targets in image five. The PDMS alone without gel still has good image quality without actuation, proving the possibility for image quality that is close to the *positive control* with the couplant alone, regardless if actuation is or is not present.

5.2 Quantitative Results

The following section details the quantitative results that were found through experimentation. All imaging was conducted on the CIRS General Purpose US Phantom at a depth of 7 cm. The experimental results that will be presented are as follows: *With Gel Versus Without Gel* testing, *Material* testing, *Frequency* testing, and *Homogeneity* testing.

5.2.1 With Gel Versus Without Gel

The results of the *With Gel Versus Without Gel* experimental testing will now be presented. This will include important notes as to how the experimental data was analyzed and the final conclusions that were found through this testing. All findings concluded that the *with gel* experimental condition produced higher quality images and that it was significantly different than the *without gel* condition.

5.2.1.1 Reference Image

The following image, **Figure 25**, is the reference image used for the *With Gel Versus Without Gel* experimental testing. The image was collected during the *With Gel Versus Without Gel* experimental testing. The reference image is the *with gel* condition due to it being the experimental equivalent to medical US imaging.
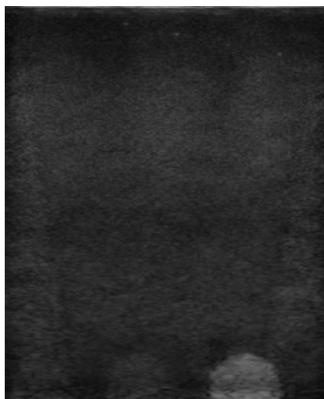
Figure 25: Reference image for with gel versus without gel testing and material testing.

An important note about this reference image is that it does not include the variables of a dry couplant or actuation. Seeing as, the goal of the *With Gel Versus Without Gel* experimental testing was to set a baseline for the best and worst images that could be experimentally acquired. In essence the results of this testing will give a spectrum for all other experimentation to then be compared to. **Figure 25** is image "42.708.png", which was used as the *With Gel Versus Without Gel* reference image. The notation of the image's title indicates the order that it was collected during data collection—there is no other significance to the numbering. The reference image is used in the calculation of signal processing metrics to quantify image quality. Each image collected will be compared to the reference image, and then the metrics calculated will be used to draw experimental conclusions and final results.

5.2.1.2 Mean, Standard Deviation, and Wilcoxon Rank Sum

MSE, PSNR, and SSIM were used to quantify the image quality of the experimental images during *With Gel Versus Without Gel* testing. **Table 9** below summarizes the findings for these three metrics for images taken either with or without gel.

Table 9: Means and standard deviations: with gel versus without gel.

Experimental Condition	MSE (Mean ± SD)	PSNR (Mean ± SD)	SSIM (Mean ± SD)
With Gel (Reference)	133.89 ± 243.86	33.33 ± 7.18	0.89 ± 0.13
Without Gel	1499.7 ± 32.72	16.37 ± 0.098	0.36 ± 0.005

As seen in **Table** 9, the MSE of *with gel* and *without gel* were both large values. The MSE corresponds to the mean squared error of pixel intensities over the entire image. A small MSE value corresponds to good image quality while a large MSE value is an indication of poor image quality. This concluded that the *with gel* condition being much closer to zero, is better in image quality than the *without gel* condition. The PSNR in the *with gel* condition was quite larger than the *without gel* condition; this shows that the *with gel* condition produced higher quality images when compared to the reference image. This is because the larger the PSNR value, the higher the quality of the image due to it being more comparable to the reference image. This subsequently shows that the *without gel* condition was of lesser quality. The SSIM metric is also calculated by comparison to the reference image. The larger the SSIM value, the more similar it is to the reference image, therefore the higher the quality. This is because it will determine the difference between the image of interest and the reference image. The SSIM value is a quantity between zero and one. Typically to be very high quality, it is desired to have a value above 0.97. From this, it can be concluded that based upon all the means calculated, the *with gel* condition is of higher quality and is more similar to the reference image.

With the means discussed, the standard deviations (SD) of these means can be used to show if these values accurately represent the entire data set for each condition. Ideally, smaller values for SD suggest that the mean is representative for the entire condition. For all metrics, the SDs were relatively low. The only slightly elevated SD was in the MSE of the *with gel* condition. The variability in this dataset is believed to be due to the fact that more of the grayscale targets of the phantom were visible, rather than the other datasets which were predominantly black and would have low variability because they would all be black. The *with gel* condition's images would vary

more because the contrast of the images is likely to vary more. This is the rationale as to why it is believed not to be concerning that the SD of the *with gel* condition is large.

Additional to the means and standard deviations for each metric, the Wilcoxon Rank Sum test was performed on the *with gel* and *without gel* conditions in comparison to the *gel reference*. **Table 10** below reports the results of this test for the *With Gel Versus Without Gel* testing.

Table 10: Results of Wilcoxon Rank Sum test: with gel versus without gel.

Experimental Condition: No Gel		MSE	PSNR	SSIM
h		1 (true)	1 (true)	1 (true)
p		2.56E-34	2.56E-34	2.56E-34
Stats	**zval**	5050	15050	15050
	ranksum	-12.22	12.22	12.22

As indicated in **Table 10** above, for both conditions, the results of this test were identical. All the h-values were equal to one and true, while all the p-values were 2.5621 x 10^{-34}, which is a small number that is close to zero. The null hypothesis in this case states that the image quality of the gel dataset is the same as the image quality of the dataset without gel. The alternative hypothesis states that the image quality of the gel dataset is different from the image quality of the dataset without gel. For both conditions based on the h and p-values, the null hypothesis is rejected, and the alternative hypothesis is accepted, proving that there is a difference between the gel and no gel datasets. This result was expected going into the experiment and proven with our calculations and statistical analysis.

It should be noted that for all Wilcoxon Rank Sum tests there was an issue that was encountered. For all tests, in all conditions, the results were the same. We ran the test several times and tried to come to a resolution why these would have been our results, but we were not able to find any issues within the tests. This resulted in all the tests being considered to be true and their results used in all presented results.

5.2.1.3 Kruskal Wallis and Pairwise Comparison

The Kruskal Wallis provided some very useful results in the comparison of the *with gel* and *without gel* conditions. **Table 11** below shows which conditions were considered and **Table 12** on the next page shows the subsequent outputs.

Table 11: With gel versus without gel Kruskal Wallis processing sequence.

Condition number	Material Name
1	With Gel (Positive Control)
2	Without Gel (Negative Control)

The numbering of the materials is useful in interpretation of the conditions in the multiple comparison based upon mean rank.

Table 12*: With gel versus without gel Kruskal Wallis important statistical outputs.*

	MSE	**PSNR**	**SSIM**
P-Value	2.52E-34	2.52E-34	2.52E-34
Chi Square	149.2537313	149.2537313	149.2537313

Evidently, the Kruskal Wallis provided some very useful results in the comparison of the *with gel* and *without gel* conditions. For all metrics, it was found that the p-value was $2.52 \times 10^{-34.}$ This value indicated a rejection of the null hypothesis that both experimental conditions came from the same distribution, which then confirmed the alternative hypothesis that they come from different distributions. The next numerical finding was in the STATS calculations with the value of chi square that is calculated. For all metrics, it was found that chi square value was 149.25. The very large number shows that there is a very large difference between the two conditions.

Additionally, the box plot generated for the MSE metric also provided some very useful information. It showed that there was a large distribution in the *with gel* dataset and that there was a small distribution the *without gel* dataset. Lastly, there was a large difference in the median values for both conditions. This is shown in the boxplot in **Figure 26** below.
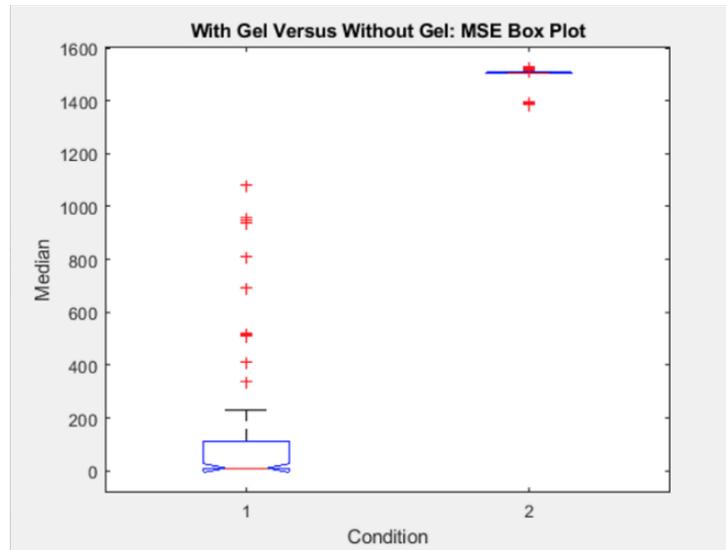
Figure 26*: Box plot of the MSE metric with gel versus without gel.*

The Pairwise comparison also produced significant results. From the computed Z statistics, the value of interest was the p-value. For this test, the p-values were very small, all metrics being 1.06×10^{-10}, which depicts a large difference between conditions. The multiple comparison based on mean ranks plot also supported this finding. The MSE metric example can be referenced in **Figure 27** on the next page; the same findings were supported through all metrics. The plot showed a significant difference between conditions due to their means not intersecting on the plot. Once again, this rejected the null hypothesis that the conditions came from the same distribution.
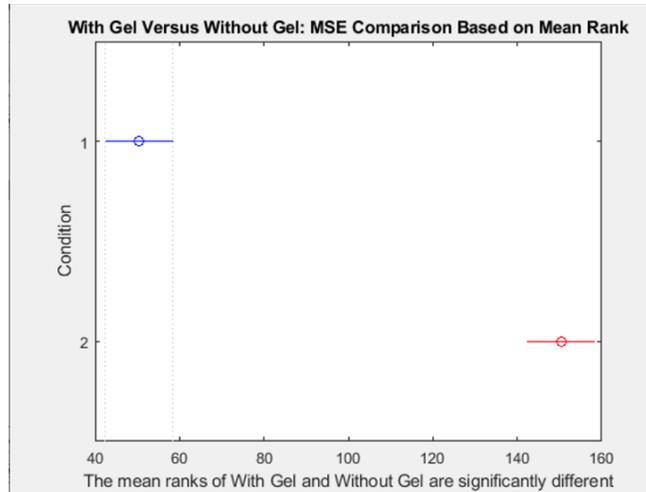
Figure 27: With gel versus without gel comparison based on mean rank MSE.

Both statistical tests show statistically significant findings that the conditions of *with gel* versus *without gel* are significantly different, as supported by the previous findings of the metric calculations and Wilcoxon Rank Sum test.

5.2.2 Material Testing

The results of the *Material* testing will now be presented. This will include important notes as to how the experimental data was analyzed and the final conclusions that were found through this testing. All findings concluded that there was a large difference between materials tested, PDMS was a viable replacement for topical gel as a dry couplant, and PDMS with TiO_2 diminished image quality.

5.2.2.1 Reference Image

The same reference image that was discussed in **5.2.1.1 Reference Image** was also used in *Material* testing signal processing. Again, the aim of the reference image is in the calculation of signal processing metrics to quantify image quality. Each image collected of all materials will be compared to the reference image, and then the metrics calculated will be used to draw experimental conclusions and final results.

It should be noted that all images of *Material* testing were the same shape as those collected in the *With Gel Versus Without Gel* experimental testing. This shape is shown through the reference image. All images have a square composition. This confirms that using this image as a reference image produced accurate results in signal processing performed.

5.2.2.2 Mean, Standard Deviation, and Wilcoxon Rank Sum

For *Material* testing, the materials of interest were neoprene, nitrile rubber, PDMS, and PDMS with TiO_2. To quantify image quality, MSE, PSNR, and SSIM were of interest. The results of these three metrics for each of these materials is shown on the next page in **Table 13**.

Table 13: *Means and standard deviations of all materials imaged in material testing, with the statistically significant data highlighted in blue.*

Experimental Condition	MSE (Mean ± STD)	PSNR (Mean ± STD)	SSIM (Mean ± STD)
Reference with Gel (100 images)	133.89 ± 243.86	33.33 ± 7.18	0.89 ± 0.13
Neoprene	1381 ± 8.008	16.72 ± 0.025	0.29 ± 0.005
Nitrile Rubber	1385.2 ± 2.82	16.72 ± 0.008	0.30 ± 0.006
PDMS 0% TiO$_2$	1320 ± 40.01	16.91 ± 0.13	0.31 ± 0.005
PDMS 1% TiO$_2$	1380 ± 26.55	16.75 ± 0.08	0.29 ± 0.01
PDMS 3% TiO$_2$	1370 ± 4.30	16.75 ± 0.01	0.29 ± 0.002
PDMS 5% TiO$_2$	1370 ± 4.30	16.75 ± 0.01	0.29 ± 0.002
PDMS 7.5% TiO$_2$	1379 ± 11.88	16.74 ± 0.037	0.29 ± 0.006
PDMS 10% TiO$_2$	1390.9 ± 12.13	16.70 ± 0.04	0.28 ± 0.008
PDMS 12.5% TiO$_2$	1377.8 ± 10.56	16.74 ± 0.03	0.29 ± 0.005
PDMS 15% TiO$_2$	1376 ± 8.62	16.74 ± 0.02	0.29 ± 0.003
PDMS 17.5% TiO$_2$	1374.8 ± 8.46	16.74 ± 0.02	0.29 ± 0.004
PDMS 20% TiO$_2$	1320 ± 5.18	16.94 ± 0.02	0.32 ± 0.002

The MSE corresponds to the mean squared error of pixel intensities over the entire image. If the MSE value is smaller, it indicates good image quality while a large MSE value indicates poor image quality. The goal for the MSE values of material testing is that all materials are similar to, if not close to, the low MSE value of the gel reference, which is 133.89. The materials overall had a common trend of being in the 1300 range, indicating poor image quality for all the materials tested. Although this statement is true, the *0%* and *20% TiO$_2$-PDMS* stood out, with values both in the 13,200 range, while the other materials were in the 13,700-13,900 range. Similar trends were found as well in both the PSNR and SSIM. The PSNR (peak signal to noise ratio) measures the peak error of the image, and the SSIM (structural similarity index) determines the difference between the image of interest and the reference image. If the PSNR and SSIM values were larger, there is an indication of higher image quality because it is more comparable to the reference image. The expectation for these metrics is that the gel reference had the highest values with the best image quality. This statement was proven true for PSNR with the *gel reference* having the highest value of 33.33. Out of all materials, the *0%* and *20% TiO$_2$-PDMS* had the highest values of PSNR at 16.91 and 16.94, being the most comparable to the *gel reference*. The rest of the materials range from 16.72-16.75. For the SSIM, the *gel reference* had the highest value as well at 0.89. The *0%* and *20% TiO$_2$-PDMS* also had the highest values, at 0.31 and 0.32, while the rest of the materials ranged from 0.28-0.30.

Overall, the three metrics show a common trend in which the *0%* and *20% TiO$_2$-PDMS* materials stood out with a small margin, showing a possibility that PDMS is promising as a couplant, and most of the materials with PDMS and *TiO$_2$* had indications of poorer image quality

due to the higher MSE values, higher PSNR values, and higher SSIM values, when compared to the condition with PDMS and without TiO_2 with slightly better values. Additionally, the standard deviations of all the metrics were low, indicating that the means were representative, adding to the validity of the results for the means of each condition's metrics. Again, it can be noted that the *with gel* condition MSE had a large SD; for the rationale as to why this is seen to not be an issue in the condition's results, refer to **5.2.1.2 Mean, Standard Deviation, and Wilcoxon Rank Sum**.

The Wilcoxon Rank Sum test which considers the medians of the two independent samples was also performed for each material; it was used to show that the materials were different from the gel reference dataset. For all materials, the results of this test were identical. An example of the results from this test for one material can be found in **Table 14** below.

Table 14: Example of results of two-sample Wilcoxon Rank Sum for material testing, comparing all materials to positive control.

Experimental Condition: 0% TiO₂ PDMS		MSE	PSNR	SSIM
h		1 (true)	1 (true)	1 (true)
p		2.56E-34	2.56E-34	2.56E-34
Stats	**zval**	5050	15050	15050
	ranksum	-12.22	12.22	12.22

All the h-values were equal to one and true, while all the p-values were 2.5621×10^{-34}, which is a small number that is close to zero. The null hypothesis in this case states that the image quality of the gel dataset is the same as the image quality of the material dataset. The alternative hypothesis states that the image quality of the gel dataset is different from the image quality of the material dataset. For every material based on the h and p-values, the null hypothesis is rejected, and the alternative hypothesis is accepted, proving that there is a difference between the gel and material datasets. This result was expected going into the experiment and proven with the calculations and statistical analysis.

5.2.2.3 Kruskal Wallis and Pairwise Comparison

In the Kruskal Wallis test similar results were found as those found in the Wilcoxon Rank Sum. As before, the materials of interest were neoprene, nitrile rubber, PDMS, and PDMS with TiO_2. On the next page, **Table 15** shows each condition which was used in the Kruskal Wallis test, and **Table 16** shows the important outputs.

Table 15: All materials Kruskal Wallis processing sequence.

Condition Number	Material Name
1	With Gel (Positive Control)
2	Without Gel (Negative Control)
3	Neoprene
4	Nitrile Rubber
5	PDMS 1% TiO_2
6	PDMS 3% TiO_2
7	PDMS 5% TiO_2
8	PDMS 7.5% TiO_2
9	PDMS 10% TiO_2
10	PDMS 12.5% TiO_2
11	PDMS 15% TiO_2
12	PDMS 17.5% TiO_2
13	PDMS 20% TiO_2
14	PDMS 0% TiO_2

The numbering of the materials is useful in interpretation of the conditions in the multiple comparison based upon mean rank.

Table 16: All materials Kruskal Wallis important statistical outputs.

	MSE	PSNR	SSIM
P-Value	1.10E-190	1.10E-190	6.42E-173
Chi Square	931.06	931.06	848.23

As seen in **Table** 16 above, for the metrics of MSE and PSNR, the p-value was 1.10×10^{-190}, and for SSIM, the p-value was 6.42×10^{-173}. While it is not consistent between all metrics, these p-values are considerably less than zero, proving the test to reject the null hypothesis. The null hypothesis of the Kruskal Wallis test is that all conditions come from the same distribution. This confirms the alternative hypothesis that all conditions do not come from the same distribution. Based upon the STATS calculations, the chi square was found to be 931.06 for both MSE and PSNR, and it was 848.23 for SSIM. Again, while not all metrics are consistent, both values are extremely large and confirm that there is a large difference between conditions.

Lastly, a boxplot of the MSE metric shows results supporting this finding as well. In this plot, it is clearly depicted that the positive and negative controls, conditions 1 and 2, form bounds

for the best and worst MSE median values, respectively. This boxplot for the MSE metric is shown in **Figure 28** below.
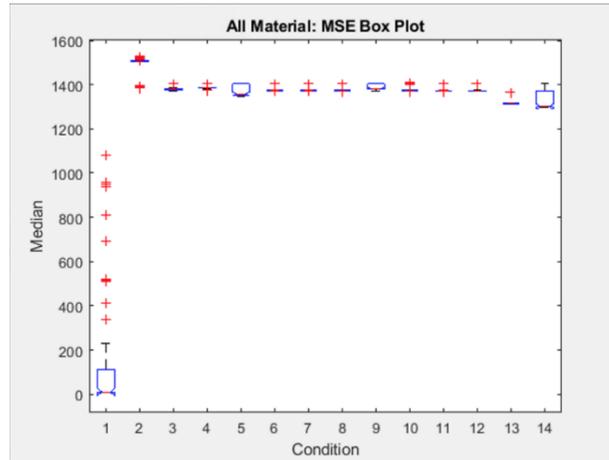
Figure 28: Box plot of the MSE metric for each material used as couplant.

Figure 28 shows the ideal 'spectrum' that was discussed previously in order to determine image quality. All other materials did fall within these bounds (between condition 1 and 2). The median that was closest to the positive control for this metric is the *0% TiO₂-PDMS*. This was found to be true for all metrics, showing that in our statistical analysis, it can be concluded that *0% TiO₂-PDMS* is the most comparable in quality to the positive control.

Through the pairwise comparison, it was found that the computed Z statistic was significantly small for all materials. There were some outliers that were closer, if not equal to, one as well. Being close to one shows that those materials' image quality being compared were comparable. However, when looking at the dataset as a whole, there was not a significant amount of comparability, leading to the conclusion that there was a difference between the materials' image quality being compared.

The next important aspect of the pairwise comparison was the multiple comparison based upon mean rank, which can be referred to in **Figure 29** below, showing the MSE metrics.
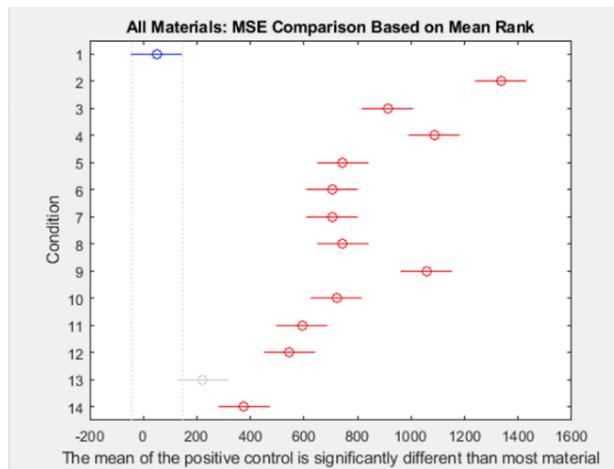
Figure 29: Comparison of all couplant materials, based on mean rank MSE.

In the plot in **Figure 29**, all materials' mean ranks are being compared to the *positive control*. The only material that was comparable was the *20% TiO$_2$-PDMS*. For the PSNR metric, the only material comparable was the also *20% TiO$_2$-PDMS*, and for SSIM, the only material comparable was the *negative control*. This shows that there was a large amount of variability between material pairwise comparison of metrics, with each test consisting of fourteen conditions and each only having one comparability outcome to the *positive control*. It was concluded that the comparability found could have been outliers or reasonable accountability in the data, forming the final conclusion that all materials tested were significantly different. This is further supported in the following discussion of statistical analysis performing on materials of interest. It is also interesting to note that there was some comparability found between the following materials: *PDMS 3% TiO$_2$, PDMS 5% TiO$_2$, PDMS 7.5% TiO$_2$, PDMS 10% TiO$_2$, PDMS 12.5% TiO$_2$, PDMS 15% TiO$_2$,* and *PDMS 17.5% TiO$_2$*. This result supports our claim that the higher TiO$_2$ concentrations of PDMS negatively affected image quality, seeing as it was already found that the higher concentrations of TiO$_2$ PDMS were more comparable to the negative control. Now that this statistical analysis shows that they are similar to each other, it supports the conclusion that the higher the concentration of TiO$_2$, the more likely it was to lead to poor image quality.

Kruskal Wallis and Pairwise comparisons were also performed on only materials of interest and supported the conclusion that all materials were significantly different. The materials of interest were determined through all experimental analysis previously presented. The following materials were compared: the *positive control,* the *negative control, nitrile rubber, 0% TiO$_2$ PDMS, 1% TiO$_2$ PDMS, 3% TiO$_2$ PDMS,* and *5% TiO$_2$ PDMS*. The same statistical findings held true. For the Kruskal Wallis test, it was found that there was a significant difference between all materials. In the pairwise comparison, it was found that there was a difference between materials with a similarity found in nitrile rubber, *1% TiO$_2$ PDMS,* and *3% TiO$_2$ PDMS*. This was slightly different from the analysis of all materials; however, it does show that there is some variability to consider as previously mentioned when drawing conclusions based upon mean rank. Since the mean is ranked in order to perform the statistical test, there is some variance depending on the inputted condition, hence why the comparability of materials is slightly different between the two tests.

In conclusion, it was found through the Kruskal Wallis and Pairwise comparison tests that all materials were statistically significantly different. It was also found that there was some comparability between materials, but the only comparability that could be confidently confirmed was that high concentrations of TiO$_2$-PDMS were comparable in image quality.

5.2.3 Frequency Testing

The results of the *Frequency* experimental testing will now be presented. This will include important notes as to how the experimental data was analyzed and the final conclusions that were found through this testing. All testing was done with the *0% TiO$_2$ PDMS* because it was proven through *Material* testing to be the most effective dry couplant. All findings found that *0% TiO$_2$ PDMS without gel or actuation* was the best experimental condition, the presence of gel in tandem with PDMS impedes image quality, there is a statistical difference between the positive control and the other experimental conditions, the use of actuation does not have a significant impact on image quality, and the 6 Hz actuation was a better frequency in comparison to the 14 Hz.

5.2.3.1 Reference Image

The following image, **Figure 30**, is the reference image used for the *Frequency* testing. The image displayed is "22_20_06.282868.png". Again, the notation of the image's title denotes the order that it was collected during data collection. The reference image is used in the calculation of signal processing metrics to quantify image quality. Each image collected will be compared to the reference image, and the metrics calculated will be used to draw experimental conclusions and final results. This new reference image is different from those used in other signal processing due to the images in frequency testing being a fan shape rather than a square.

Figure 30*: Reference image for frequency testing.*

5.2.3.2 Mean, Standard Deviation, and Wilcoxon Rank Sum

In *Frequency* testing, images were taken at either 0 Hz (no actuation), 6 Hz, or 14 Hz sonic frequencies. **Table 17** below shows the MSE, PSNR, SSIM for various conditions.

Table 17*: Means and standard deviations during frequency testing (effects of actuation), where yellow shows PDMS with gel at either 0, 6, or 14 Hz actuation, green shows the negative control, and blue shows the positive control.*

Experimental Condition	MSE (Mean ± STD)	PSNR (Mean ± STD)	SSIM (Mean ± STD)
6 Hz: No PDMS, no gel, actuation	287.51 ± 5.40	23.55 ± 0.08	0.73 ± 0.002
6 Hz: No PDMS, gel, actuation	1223.3 ± 63.67	17.26 ± 0.22	0.34 ± 0.02
6 Hz: PDMS, no gel, actuation	132.0 ± 1.53	26.94 ± 0.05	0.76 ± 0.001
6 Hz: PDMS, gel, actuation	1120.8 ± 23.25	17.64 ± 0.08	0.36 ± 0.006
14 Hz: No PDMS, no gel, actuation (Negative Control)	300.92 ± 5.47	23.25 ± 0.07	0.73 ± 0.01
14 Hz: No PDMS, gel, actuation	1225.2 ± 0.76	17.24 ± 0.002	0.34 ± 0.002
14 Hz: PDMS, no gel, actuation	142.41 ± 1.80	26.60 ± 0.05	0.76 ± 0.0009
14 Hz: PDMS, gel, actuation	1268.5 ± 93.64	17.11 ± 0.32	0.32 ± 0.04
No PDMS, gel, no actuation (Positive Control)	24.90 ± 2.82	34.13 ± 0.1	0.85 ± 0.02
PDMS, no gel, no actuation	124.56 ± 3.68	27.18 ± 0.13	0.76 ± 0.003
PDMS, gel, no actuation	1121.5 ± 2.34	17.63 ± 0.009	0.37 ± 0.001

The MSE as discussed above in **5.2.2.2 Mean, Standard Deviation, and Wilcoxon Rank Sum** corresponds to the mean squared error of pixel intensities over the entire image. Out of all the metrics, MSE stood out. PSNR is typically best to use; however, MSE compares to the reference, showing the most comparability, proving to be our best metric in this case. The higher the MSE value, the poorer quality of the dataset. The expected result is that the gel MSE value would be the lowest because it is the conventional method used for US imaging. The *gel reference* had the smallest MSE with a value of 24.90. The other conditions in this set had MSE values ranging from 124.56 to 1268.5, which are significantly higher values than the gel reference, meaning that the other conditions have poorer image quality. Although the reference had the best MSE value, there were some conditions that had values on the lower side around 100. The condition with just the *0% TiO$_2$ PDMS* without gel or actuation had a value of 124.56; the condition with actuation at *6 Hz, a couplant (0% TiO$_2$ PDMS), and no gel* had a value of 132; and the condition with actuation at *14 Hz, a couplant (0% TiO$_2$ PDMS), and no gel* had a value of 142.41. As discussed previously, qualitatively all three visually had similar quality showing three to four grayscale targets, which is shown here as well as all three are in a similar range. Additionally, the PDMS without gel with actuation at *14 Hz* has a higher value of 142 than the one at *6 Hz* with a value of 132. This was also proven in the *14 Hz* condition, where only three distinctive grayscale targets were seen and in the *6 Hz* where four distinctive grayscale targets were seen. The rest of the conditions are higher than 200 and go all the way up to 1268.5, leading all the way to the poorest indication of image quality. Overall, the *gel reference* dataset has the best image quality while the condition using just the couplant had the second-best quality. The third and fourth conditions with best quality were in a similar range, and both used the couplant with actuation and without gel. Thus, the values show that the *PDMS without gel or actuation* is the best material of interest and a viable replacement for gel. For all the three metrics, the standard deviations were all generally low, suggesting that the means are representative, adding validity to our results.

Additionally, in frequency testing, a pattern was found indicating that gel impedes the image quality when used with the actuation and materials or both then compared to conditions without gel. This trend can be seen in **Table 18** below.

Table 18: Means and standard deviations during frequency testing (effects of gel), where white corresponds to without gel and blue corresponds to with gel.

Experimental Condition	MSE (Mean ± STD)
6 Hz: No PDMS, no gel, actuation	287.512 ± 5.40
6 Hz: No PDMS, gel, actuation	1223.3 ± 63.67
6 Hz: PDMS, no gel, actuation	132.0 ± 1.53
6 Hz: PDMS, gel, actuation	1120.8 ± 23.25
14 Hz: No PDMS, no gel, actuation (negative)	300.92 ± 5.47
14 Hz: No PDMS, gel, actuation	1225.2 ± 0.76
14 Hz: PDMS, no gel, actuation	142.41 ± 1.80
14 Hz: PDMS, gel, actuation	1268.5 ± 93.64

In **Table 18**, the detrimental effect of gel with PDMS is shown, where the mean values of the MSE across the board are significantly better for the conditions without gel when compared to the conditions with gel. Consistently for both the *6 Hz* and *14 Hz* conditions, the MSE values for the conditions with gel are in the thousands, indicating poorer image quality when compared to the conditions without gel that have smaller MSE values in the hundreds. This shows that gel impedes the quality of the images while the absence of gel contributes to better image quality.

The Wilcoxon Rank Sum test was also performed on each condition for *Frequency* testing and is used to show that the *gel reference* dataset is different from the other 11 conditions tested. The test can be found in **Table 19** below.

Table 19: Results of two-sample Wilcoxon Rank Sum for frequency testing, comparing different conditions to the positive control.

Experimental Condition: PDMS, no gel, no actuation		MSE	PSNR	SSIM
h		1 (true)	1 (true)	1 (true)
p		2.56E-34	2.56E-34	2.56E-34
	zval	5050	15050	15050
Stats	**ranksum**	-12.22	12.22	12.22

For all the conditions, the results of this test were identical All of the h-values were equal to one and true. While all the p-values were 2.56×10^{-34}, which is a small number that is close to zero. The null hypothesis in this case states that the image quality of the gel dataset is the same as the image quality of the material dataset. The alternative hypothesis states that the image quality of the gel dataset is different from the image quality of the material dataset. For every condition based on the h and p-values, the null hypothesis is rejected, and the alternative hypothesis is accepted, proving there is a difference between the *gel dataset* and the rest of the conditions. This was expected going into the experiment and proven with calculations and statistical analysis.

5.2.3.3 Kruskal Wallis and Pairwise Comparison

With the nature of the *Frequency* testing, both the Kruskal Wallis and Pairwise Comparison tests were conducted in a slightly different fashion than in the other experimental conditions. The aim of these tests was to demonstrate the influence of the dry couplant and the effect that actuation had on imaging quality. This resulted in the following groups of Kruskal Wallis and Pairwise Comparison tests to be run: all 6 and 14 Hz actuation with couplant, all 6 and 14 Hz actuation without couplant, all 6 Hz, all 14 Hz, and all that did not include actuation. The conditions that did not include actuation were as follows: positive control, negative control, PDMS with gel, and PDMS without gel. This no actuation grouping allowed for the same results that were found within material testing to be further corroborated now in this new period of experimentation. All statistical results confirmed the results presented in **5.2.2 Material Testing**. Again, it should be noted that for statistical processing of the other grouped conditions, the negative reference was the *14 Hz actuation, no PDMS, no gel* due to there being variance in image composition in the intended negative reference of *no actuation, no PDMS, no gel* that was collected.

In the Kruskal Wallis test, it was confirmed that each group of conditions had a large variance between them. This was proven through all tests producing a large p-values and large chi square values. Both of which show that the conditions being compared within the test come from a different distribution. It was also found that through the pairwise comparison tests, that for all conditions tested there was a significant difference between them. There were no conditions of noteworthy comparability. **Tables 20** and **21** below show the experimental conditions tested using Kruskal Wallis, for both 6 Hz and 14 Hz frequencies, respectively.

Table 20: *6 Hz frequencies Kruskal Wallis processing sequence.*

Condition Number	Material Name
1	No PDMS, gel, no actuation (Positive Control)
2	14 Hz: No PDMS, no gel, actuation (Negative Control)
3	6 Hz: PDMS, gel, actuation
4	6 Hz: No PDMS, gel, actuation
5	6 Hz: PDMS, no gel, actuation
6	6 Hz: no PDMS, no gel, actuation

Table 21: *14 Hz frequencies Kruskal Wallis processing sequence*

Condition Number	Material Name
1	No PDMS, gel, no actuation (Positive Control)
2	14 Hz: No PDMS, no gel, actuation (Negative Control)
3	14 Hz: PDMS, gel, actuation
4	14 Hz: No PDMS, gel, actuation
5	14 Hz: PDMS, no gel, actuation
6	14 Hz: No PDMS, no gel, actuation

The Kruskal Wallis boxplots allowed for the most conclusive answers to our experimental inquiries. In **Figures 31** and **32** on the next page, the Kruskal Wallis MSE box plots are shown for 6 Hz actuation and 14 Hz actuation, respectively. In each of these box plots, the first two conditions are the positive and negative controls, and then the conditions are the variations of gel and PDMS. For further clarification on the ordering of conditions, refer to **Tables 20** and **21** above.
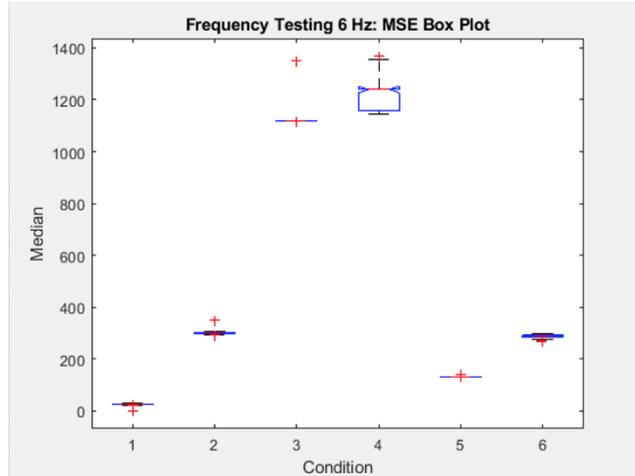
Figure 31*: Box plot of the MSE metric when actuation is at 6 Hz.*
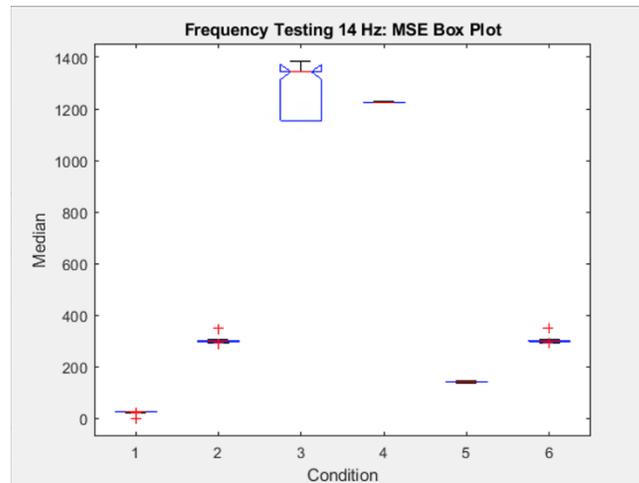
Figure 32*: Box plot of the MSE metric when actuation is at 14 Hz.*

In both box plots in **Figures 31** and **32**, conditions three and four include gel and conditions five and six do not. Samples five and six lie within the bounds of the positive and negative controls and three and four do not. This proves that the use of gel in addition to the dry couplant had much worse image quality than those images without gel. In *Material* testing, all couplants were tested with the use of topical gel, with the aim of eliminating the impedance of air that could corrupt image quality, allowing solely the functionality of the dry couplant to be determined. However, through this frequency testing, it is found that the use of gel actually had the opposite affect and interfered with image quality. The experimental conditions that were shown to be best, their medians being the closest to the *positive control, were 6 Hz: PDMS, no gel, actuation* and *14 Hz: PDMS, no gel, actuation,* respectively. This further supported the claim that PDMS without gel was the best experimental condition. This also shows that there is not a significant result as to which frequency of actuation is better. Both 6 and 14 Hz have comparable medians. The best experimental condition between the two frequencies can be found to be *6 Hz: PDMS, no gel, actuation*. While it is by a very small margin, the median is closer to the *positive control* then the 14Hz.

Now that the 6 Hz and 14 Hz actuation frequencies were discussed, a discussion of all frequencies of interest can take place. **Table 22** below shows the conditions of interest used in the Kruskal Wallis processing sequence, where 0 Hz, 6 Hz, and 14 Hz are all detailed. Below **Table 22** is **Figure 33**, which shows a box plot representation of data from those five conditions.

Table 22: All frequencies of interest Kruskal Wallis processing sequence.

Condition Number	Material Name
1	No PDMS, gel, no actuation (Positive Control)
2	14 Hz: No PDMS, no gel, actuation (Negative Control)
3	PDMS, no gel, no actuation
4	6 Hz: PDMS, no gel, actuation
5	14 Hz: PDMS, no gel, actuation
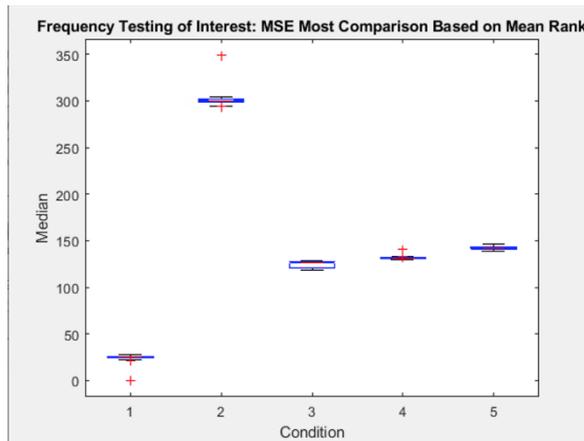
Figure 33: Box plot of the MSE metric when actuation is at "frequencies of interest".

In **Figure 33** showing the MSE box plot of *All Frequencies of Interest*, it compares the positive and negative controls to *PDMS, no gel, no actuation, 6 Hz: PDMS, no gel, actuation* and *14 Hz: PDMS, no gel, actuation*. These conditions were 'frequencies of interest' because they were isolated to be the best overarching experimental conditions through all frequency testing. There is a prominent ascending order between the three conditions of interest. Through the comparison of medians, it can be seen that *PDMS, no gel, no actuation* was the best experimental condition because it is the closest in value to the *positive control*. Alternatively, it can be seen based upon the medians that *14 Hz: PDMS, no gel, actuation* was the worst experimental condition due to it being the closest to the *negative control*. As discussed in the previous box plot comparisons of the 6 and 14 Hz conditions, the conclusion of *6 Hz: PDMS, no gel, actuation* being the better of the two frequencies is further supported. It can be determined conclusively that the optimal experimental condition is *PDMS, no gel, no actuation*.

In conclusion, through the Kruskal Wallis and Pairwise comparison tests, there were several major findings, the first being the use of gel and a dry couplant impedes image quality. The use of actuation does not have a significant impact on image quality. The 6 Hz actuation was

a better frequency, by a small margin, in comparison to the 14 Hz. Lastly, the best experimental condition was *PDMS, no gel, no actuation*.

5.2.4 Homogeneity Testing

The following section will describe the results from the testing of PDMS TiO$_2$ homogeneity as discussed in the methodology of the project. The aim of this testing was to see if imaging different regions of a PDMS sample with TiO$_2$ would result in a variance in image quality. This would then demonstrate that the dispersion of TiO$_2$ was different throughout the PDMS sample. Allowing for the conclusion to be drawn that the TiO$_2$ was not homogenous throughout the PDMS samples and which could have affected the results of *Material* testing. In other words, the PDMS samples with varying concentrations of TiO$_2$ results could have been skewed due to the homogeneity of TiO$_2$ that was present in the area imaged during *Material* testing.

The PDMS used in this testing was the 7.5% TiO$_2$ PDMS. It was imaged in three regions of the square sample, the lower right (LR), the middle (M) and the upper left (UL). The results of the *Homogeneity* experimental testing will now be presented. This will include important notes as to how the experimental data was analyzed and the final conclusions that were found through this testing. It was found that homogeneity was not an issue within the 7.5% TiO$_2$ PDMS sample, however this is still a factor that should be considered when viewing the results as a whole. Further homogeneity testing should be conducted if the project was to be continued or reproduced.

5.2.4.1 Reference Image

The same reference image that was discussed in **5.2.1.1 Reference Image** was also used in *Homogeneity* testing signal processing. Again, the aim of the reference image is in the calculation of signal processing metrics to quantify image quality. Each image collected in *Homogeneity* testing will be compared to the reference image and then the metrics calculated will be used to draw experimental conclusions and final results. All images of *Material* testing were the same shape as those collected in the *Homogeneity* experimental testing, which is shown in the reference image. All images have a square composition. This confirms that using this image as a reference image produced accurate results in signal processing performed.

5.2.4.2 Mean, Standard Deviation, and Wilcoxon Rank Sum

As mentioned, the 7.5% TiO$_2$ PDMS sample was imaged in different locations: LR, M, and UL. The MSE, PSNR, and SSIM at each location is shown in **Table 23** below.

Table 23: Means and standard deviations during homogeneity testing.

Experimental Condition	MSE (Mean ± SD)	PSNR (Mean ± SD)	SSIM (Mean ± SD)
LR	1377.55 ± 16.57	1 ± 0.05	0.29 ± 0.01
M	1380.95 ± 21.14	16.73 ± 0.07	0.29 ± 0.01
UL	1373.92 ± 5.08	16.75 ± 0.02	0.29 ± 0.002

Focusing on the MSE metric, which shows more comparability to the PSNR and SSIM in this case, all three locations on the *7.5% TiO₂ PDMS* have high MSE values. This indicates that all three have poor image quality and that one spot of the PDMS sample is not worse than the other, showing homogeneity throughout this sample as the numbers are all in a similar range with an indication of poor image quality.

Additional to the means and standard deviations of the metrics, the Wilcoxon Rank Sum test was performed on the condition using the conventional method of US imaging with gel (positive control), and the three locations on the sample PDMS. **Tables 24**, **25**, and **26** below show the Wilcoxon Rank Sum results for the lower right, middle, and upperleft locations respectively.

Table 24: Results of two-sample Wilcoxon Rank Sum for lower right (LR) of 7.5% TiO₂ PDMS compared to positive control.

Experimental Condition: LR		MSE	PSNR	SSIM
h		1 (True)	1 (True)	1 (True)
p		2.56E-34	2.56E-34	2.56E-34
	zval	5050	15050	15050
Stats	**ranksum**	-12.22	12.22	12.22

Table 25: Results of two-sample Wilcoxon Rank Sum for middle (M) of 7.5% TiO₂ PDMS compared to positive control.

Experimental Condition: M		MSE	PSNR	SSIM
h		1 (True)	1 (True)	1 (True)
p		2.56E-34	2.56E-34	2.56E-34
	zval	5050	15050	15050
Stats	**ranksum**	-12.22	12.22	12.22

Table 26: Results of two-sample Wilcoxon Rank Sum comparing upper left (UL) of 7.5% TiO₂ PDMS compared to positive control.

Experimental Condition: UL		MSE	PSNR	SSIM
h		1 (True)	1 (True)	1 (True)
p		2.56E-34	2.56E-34	2.56E-34
	zval	5050	15050	15050
Stats	**ranksum**	-12.22	12.22	12.22

From **Tables 24**, **25**, and **26**, it is evident that the lower right, middle, and upper left locations all proved to be different than the positive control with h-values of 1 as well as p-values that are close to zero, allowing us to reject the null hypothesis that they are the same to the

positive control and accept the alternative hypothesis that they are different from the positive control. This result was expected as the positive control is the best method of imaging and should be different in quality to all the locations on the *7.5% TiO₂ PDMS*. Overall, there are similar patterns found in the MSE value showing poor image quality and showing a difference from the positive control in the Wilcoxon Rank Sum test for the three locations on the sample PDMS. This suggests the image quality of the *7.5% TiO₂ PDMS* as a whole is uniform and mostly homogenous for the lower right, middle, and upper left locations imaged from the sample.

5.2.4.3 Kruskal Wallis and Pairwise Comparison

In the Kruskal Wallis test there were some interesting results when trying to determine the homogeneity of TiO_2 in the *7.5% TiO₂ PDMS* sample. **Table 27** below shows the different conditions for the Kruskal Wallis test, followed by **Table 28** which reports the results.

Table 27: Homogeneity Kruskal Wallis processing sequence.

Condition Number	Material Name
1	With Gel (Positive Control)
2	Without Gel (Negative Control)
3	PDMS 7.5% TiO_2 LR
4	PDMS 7.5% TiO_2 M
5	PDMS 7.5% TiO_2 UL

The numbering of the materials is useful in interpretation of the conditions in the multiple comparison based upon mean rank.

Table 28: Homogeneity Kruskal Wallis important statistical outputs.

	MSE	PSNR	SSIM
P-Value	2.69E-81	2.69E-81	8.31E-83
Chi Square	381.55	381.55	388.54

For the metrics of MSE and PSNR, the p-value was 2.69×10^{-81}, and for SSIM, the p-value was 8.31×10^{-83}. While it is not consistent between all metrics, these p-values are considerably less than zero proving the test to reject the null hypothesis. The null hypothesis of the Kruskal Wallis test is that all conditions come from the same distribution. This confirms the alternative hypothesis that all conditions do not come from the same distribution. Based upon the STATS calculations, the chi square was found to be 381.55 for both MSE and PSNR, and 388.54 for SSIM. Again, while not all metrics are consistent, both values are extremely large and confirm that there is a large difference between conditions.

Additionally, a boxplot for the MSE metric for all five conditions was helpful to draw conclusions. As shown in **Figure 34** on the next page, the positive and negative controls, conditions 1 and 2, respectively, form bounds for the best and worst MSE median values.
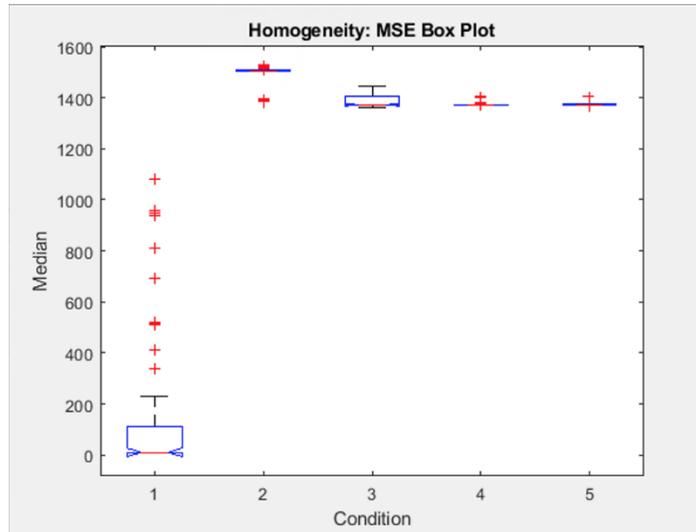
Figure 34: Box plot of the MSE metric for 7.5% TiO₂-PDMS at different locations.

All images of the *7.5% TiO₂ PDMS* fell within these bounds between condition 1 and condition 2. The median that was closest to the positive control for this metric is the *LR* imaging of the *7.5% TiO₂ PDMS*. However, it is clearly depicted that the medians of all conditions, *LR, M,* and *UL*, are all extremely similar. They all also have a similar distribution within their respective datasets. The only condition with some variance was the *LR* condition. This allows for the conclusion to be drawn that there is a small variance, but all three datasets are reasonably similar to the *positive control*. These trends held true for all metrics. This points to the conclusion that the sample could be homogeneous.

Through the pairwise comparison, the fact of homogeneity is further explored. In **Figure 35** below, the mean rank of the *LR* condition is being compared to all other conditions.
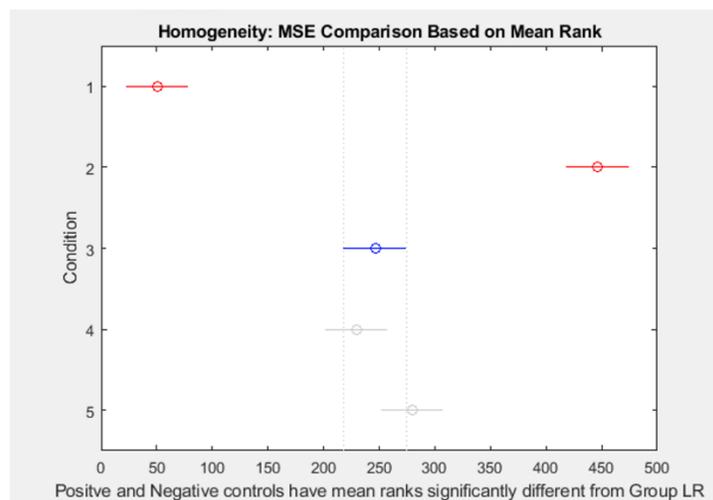
Figure 35: Homogeneity analysis of 7.5% TiO₂-PDMS, based on mean rank MSE.

Through this plot in **Figure 35**, it is clear that conditions four and five, M, and UL respectively, are comparable to the *LR* condition due to their grey color. The *positive* and *negative*

controls were significantly different seeing as they are red in color. This draws the conclusion that the *LR, M,* and *UL* conditions are all statistically significantly similar based upon mean rank. These trends held true for all metrics.

In conclusion, it was found through the Kruskal Wallis and Pairwise comparison tests that all imaging of the *7.5% TiO₂ PDMS* in varying regions were comparable and similar, showing that there was likely a reasonable amount of homogeneity in TiO_2 throughout PDMS samples. It should still be emphasized that through the creation of PDMS, there were issues when trying to achieve homogeneity; however, these results show that despite the difficulty of homogenization, it was likely achieved regardless.

6.0 DISCUSSION

At the completion of the project, the team had developed an actuated US transducer system to perform gel-free US imaging. 3D printed parts were used to secure both the load cell and the transducer to the linear stage ball screw actuator. The design was based on the Design #4 iteration, detailed in **4.2.1 Preliminary Designs**. For testing, the entire system was made fixed to a rigid ring stand set on a tabletop. There are some evident limitations to this setup when applying to a clinical setting. The actuator itself was already rather large and heavy, combined with the transducer, 3D prints, and the ring stand, the system was far from handheld. In light of the client statement, it was desired that the physicians could hold the gel-free US imaging system in their hands so that they could translate the transducer over the surface area of skin. Evidently, the fixing nature of the ring stand prevented such movement.

With this project, the ring stand was a necessity to control the orientation of the US transducer respective to the sample being imaged as well as the force exerted on the sample. It should be noted that the Design #3 iteration from **4.2.1 Preliminary Designs** found a way to control these two factors while keeping the system dynamic. Incorporating a "feedback" loop into the Arduino code would consist of the Arduino continuously taking in the force readings from the load cell and immediately dictating the actuator to either raise or lower to return the force exerted to the desired value. For example, if the desired force was 5 N but the human operator of the system accidentally pressed down an additional 1 N just from holding the probe, the Arduino code would compensate for this by raising the actuator to alleviate the additional 1 N of force. Ultimately, the actuated transducer system associated with Design #3 would have been able to account for any confounding forces from human operation, eliminating the need for the ring stand. With the length and novelty for this project, it made more sense for the team to pursue Design #4 with a ring stand to at least demonstrate the potential for clinical gel-free US imaging so that future research can be done to make the system more dynamic and controlled.

In addition to size, another limitation of the design lies in the PDMS couplant. A dynamic system like Design #3 could only achieve so much with a square of PDMS lying flat on the skin. The 9cm x 9cm size of the PDMS couplant is a very small range for imaging. To image across a large surface area, the PDMS would have to either be manufactured in larger surface areas or the PDMS would have to be lifted and moved to the next spot for imaging. Another issue that could arise is the friction from the lateral motion causing the PDMS to bunch up underneath the US transducer, which could cause opportunities for air to get under the PDMS. A potential solution for this problem is a clip-on couplant, similar to what was detailed in Design #1 of the **4.2.1 Preliminary Designs** section. A metal O-ring structure could have been used to secure a segment

of PDMS around the lens of the US transducer. To prevent air from filling between the lens and the PDMS, the space could be filled with gel. However, this process would have to come with experimental testing, since the results from this project indicated higher image quality of PDMS when there was no gel present (i.e., would the gel-filled interface imped image quality?).

Another consideration with PDMS was the homogeneity of the TiO_2 particles dispersed within it. As mentioned in **4.3.2.2 PDMS Manufacturing Procedure**, the formation of this silicone-like material is through the many microscopic cross links forming together. This step in the procedure did require an extensive amount of mixing the silicone elastomer base and the curing agent for maximized homogeneity. Without proper mixing, some portions of the PDMS would be stiffer than others. The addition of TiO_2 to the PDMS samples made the homogenizing step much more difficult. TiO_2 is a white powder-like substance; when added to the clear PDMS, the whole sample would turn white and lose its transparency. This made it hard for the team to determine whether the PDMS with TiO_2 samples were truly entirely homogenized. Due to TiO_2 being a powder-like material and the uncured PDMS being a viscous, liquid-like material, the mixing of the two would cause TiO_2 to form clumps. This was especially true for the higher volume TiO_2 samples because there was less PDMS elastomer to saturate the powder.

The homogenization process for TiO_2-PDMS samples was simplified with the use of a "milk frother", which was essentially a battery-powered whisk. For the most part, the milk frother worked well, except for with the PDMS-TiO_2 samples with higher TiO_2 concentrations such as 15%-25%. These samples were in fact, too thick viscous for the milk frother to mix; the device continued to overheat and power off periodically. In these situations, the team had to mix the samples manually, which was more laboring and less efficient. Consequently, more effective alternatives for homogenizing the TiO_2-PDMS samples should be considered. One method that was heavily considered at the start of the project was the sonicator and its subsequent usage of sonication. Sonication is the process of applying sound energy to the sample so that the particles within the sample would homogenize or extract depending on the purpose. The sonicator has many different applications for implementation but for our project's sake, we would have used it to effectively speed up our dissolution of components. As mentioned before, if time had allowed, this method would have been a great way to homogenize the higher TiO_2-PDMS samples as they were beyond the milk frother's capabilities.

Worries about heterogeneity in TiO_2-PDMS samples were especially present after analyzing the results listed in **Table 13** in **5.2.2.2 Mean, Standard Deviation, and Wilcoxon Rank Sum**, where *Material* testing demonstrated that the image quality of 20% TiO_2-PDMS was close to the 20:1 PDMS (0% TiO_2). These two samples were the only conditions to demonstrate this higher level of image quality, compared to other materials like 1-17.5% TiO_2-PDMS. Theoretically, the 20% TiO_2-PDMS should have had the worst values by going off the **Table 13** values for the other materials. The fact that the 20% sample trial showed good, decent images but 1%-17.5% TiO_2-PDMS samples did not, could suggest heterogeneity, meaning that the image could have been taken at a less concentrated section of the sample, not representative of 20% of volume. If homogenized properly, a descending pattern in the values recorded in **Table 13** should have been seen. In order to either prove or disprove the suspicions for inhomogeneity, *Homogeneity* testing was performed, detailed in **5.2.4 Homogeneity Testing**. No significant differences were found in image quality at different locations of the 7.5% TiO_2-PDMS. However,

perhaps the 20% TiO_2-PDMS sample, since homogenization is more difficult at higher concentrations, would have shown significant differences.

Furthermore, there were a few key points the team wanted to touch over if time had allowed. For future projects, we would recommend testing out **a)** how actuation plays a role in a dynamic, not-fixed system and **b)** human testing/clinical testing. The final design iteration had the transducer-actuator system in a stationary position via a ring stand. This set-up was imperative for this project to obtain data with the least number of confounding variables. However, it would be of interest to see how this would translate to a moving, dynamic system. Friction was an important factor to keep in mind when pursuing a gel-free system. Since a dynamic system is more fitting for clinical application, it is important to acquire images that are taken in motion and see how friction plays a role. Also, dynamic testing would be necessary to validate the effectiveness of actuation to reduce friction.

Additionally, another important consideration for this project was to test the final actuated US transducer system on human tissues. This project did receive IRB approval to image various parts of the human body on team members. However, time did not allow for this to take place. Nonetheless, for future research, we recommend that images are taken of different parts of the body as this would provide more clinically relevant information and findings. For this project, a linear array transducer was used, which have a flat lens for the sake of imaging flat surfaces. If the team had access to a convex US transducer, this transducer would have been also tested, since these are common in the clinical setting; convex transducers are curved linear probes that have a wider field of view and are primarily used for curved parts of the body such as the hips, abdominal areas, and so on. Therefore, clinical trials for this system in the future should incorporate both linear array and convex US transducer to enhance the clinical significance of the research.

Overall, the results from this project indicate a good starting point for gel-free US imaging in a clinical setting. PDMS showed to be a promising couplant to replace topical gel. More research can be conducted to find what specific form for PDMS could be the best—should it remain a flat sheet against the skin or should it attach directly to the US transducer? Also, actuation proved to have little impact on image quality. Therefore, it can be inferred that poorer image quality would not be the cost of testing a dynamic imaging system. The assumption that actuation could be a useful tool to reduce friction without impeding image quality is one that should be tested with future experiments. Ultimately, the team's findings provide some scientific basis for future studies to build from in order to develop a compact, hand-held, and dynamic gel-free US imaging system for clinical applications.

7.0 Conclusion

This project was inspired by the U.S. Patent No. 9,354,206 by Zalameda and Johnston (2016), where topical gel was eliminated through two key design components: 1) replacement of topical gel with a nitrile rubber and 2) an actuation mechanism to reduce friction associated with gliding the US transducer on a gel-free surface. The latter component is characterized by "sonic" frequency, which specifies the number of cycles of lifting and then lowering the probe in one second (units of Hz). Inspired by this NASA patent, the team attempted to tackle gel-free US imaging within a clinical setting rather than an aerospace setting like Zalameda and Johnston did.

To achieve an effective gel-free US imaging system, the team focused on developing an actuated system, manufacturing or purchasing solid couplants, and creating a signal processing method to quantify image quality. The actuated system included a linear stage ball screw actuator, a load cell, a load cell amplifier, a stepper motor driver, a power supply, and an Arduino UNO Rev3 board. 3D printed parts were used to attach the Clarius linear array US transducer to the actuator while still allowing the transducer to move freely so it could exert forces on the load cell. Nitrile rubber and neoprene were considered to replace gel, but PDMS (without titanium dioxide) proved to have the highest image quality without gel during the material testing. Testing trials with the actuation mechanism were characterized by the actuator lowering the US transducer until 5 N force exerted on the phantom were read by the load cell, followed by a 0.5 mm oscillation upward and downward at either 6 Hz or 14 Hz. Experimental conditions for testing included gel-free without actuation, gel without actuation, gel-free with actuation, and gel with actuation. For the "without actuation" trials, 5 N of force was exerted but no oscillation movement followed.

From the results of testing, the 0% TiO_2-PDMS proved to have the highest image quality out of the experimental groups. While the no actuation trial had the best image quality, 6 Hz and 14 Hz sonic frequency for actuation did not have a significant impact on image quality. Furthermore, these results show a strong indication for PDMS to be a solid couplant that could replace topical gel. Further experimentation should occur for a dynamic imaging system rather than a system fixed to the ring stand, like this project tested. Additionally, more iterations of PDMS couplants should occur, testing different shapes, sizes, and configurations of the PDMS relative to the US transducer.

REFERENCES

Alpha_drift. (2010). US Modes: A, B, & M. Retrieved from
    http://sonodriftzone.blogspot.com/2010/01/US-modes-b-
    m.html#:~:text=A%2DMode%2C%20or%20Amplitude%20Modulation,amplitude%20sp
    ikes%20of%20different%20heights.&text=B%2DMode%2C%20or%20Brightness%20M
    odulation,the%20absence%20of%20vertical%20spikes.

American College of Radiology & American Association of Physicists in Medicine (ACR-
    AAPM). (2016). ACR–AAPM TECHNICAL STANDARD FOR DIAGNOSTIC
    MEDICAL PHYSICS PERFORMANCE MONITORING OF REAL TIME US
    EQUIPMENT. Retrieved from https://www.acr.org/-/media/ACR/Files/Practice-
    Parameters/US-Equip.pdf?la=en

American College of Radiology. (2019, December 13). Quality Control: US and Breast US
    (Revised 12-12-19). Retrieved from
    https://accreditationsupport.acr.org/support/solutions/articles/11000064162-quality-
    control-US-and-breast-US-revised-12-12-19-

Animal US Association. (n.d.). What is US gel for? Retrieved September 21, 2020, from
    https://www.animalUSassociation.org/what-is-US-gel-for/

Aziz, A., Dar, P., Hughes, F., Solorzano, C., Muller, M. M., Salmon, C., Salmon, M., &
    Benfield, N. (2018). Cassava flour slurry as a low-cost alternative to commercially
    available gel for obstetrical US: a blinded non-inferiority trial comparison of image
    quality. BJOG : an international journal of obstetrics and gynaecology, 125(9), 1179–
    1184. https://doi.org/10.1111/1471-0528.15123

Binkowski, A., Riguzzi, C., Price, D., & Fahimi, J. (2014). Evaluation of a cornstarch-based US
    gel alternative for low-resource settings. The Journal of emergency medicine, 47(1), e5–
    e9. https://doi.org/10.1016/j.jemermed.2013.08.073

Boxplot. Retrieved from https://www.mathworks.com/help/stats/boxplot.html

Brendel, B., Rick, S. W., Stockheim, M., & Ermert, H. (2002). Registration of 3D CT and US
    datasets of the spine using bone structures. Null, 7(3), 146-155.
    doi:10.3109/10929080209146025

Brenner, David J,PhD, DSc, & Hall, Eric J,DPhil, DSc. (2007). Computed tomography -- an
    increasing source of radiation ExposureCurrent concepts: The New England Journal of
    Medicine, 357(22), 2277-84. doi:http://dx.doi.org/10.1056/NEJMra072149

Cafarelli, A., Miloro, P., Verbeni, A., Carbone, M., & Menciassi, A. (2016). Speed of sound in
    rubber-based materials for ultrasonic phantoms. *Journal of US*, 19(4), 251–256.
    https://doi.org/10.1007/s40477-016-0204-7

Carovac, A., Smajlovic, F., & Junuzovic, D. (2011). Application of US in medicine. *Acta
    informatica medica : AIM : journal of the Society for Medical Informatics of Bosnia &*

Herzegovina : casopis Drustva za medicinsku informatiku BiH, *19*(3), 168–171. https://doi.org/10.5455/aim.2011.19.168-171

CIRS. (2013). *Thyroid US*

Craig, C. F. Phd. How US Works. Retrieved from https://www8.physics.utoronto.ca/~jharlow/teaching/phy138_0708/lec04/USx.htm.

Diagnostic imaging. (2003).Cardinal Health Inc. Retrieved from http://www.elimpex.com/companies/victoreen/Catalog/DI8.pdf

du Prel, J. B., Röhrig, B., Hommel, G., & Blettner, M. (2010). Choosing statistical tests: part 12 of a series on evaluation of scientific publications. *Deutsches Arzteblatt international*, *107*(19), 343–348. https://doi.org/10.3238/arztebl.2010.0343

E. Berry. Chapter 13: US Imaging [Powerpoint Slides]. Retrieved from https://humanhealth.iaea.org/HHW/MedicalPhysics/TheMedicalPhysicist/Studentscorner/HandbookforTeachersandStudents/Chapter_13.pdf

Engelbert, P. R. & Palma, J. K. (2015). Petroleum Jelly: A Novel Medium for Ocular US. The Journal of Emergency Medicine, 49(2), 172-174. doi:10.1016/j.jemermed.2015.03.003

Firgelli Automations Team. (2020). How Do You Control a Linear Actuator with an Arduino? Retrieved from https://www.firgelliauto.com/blogs/tutorials/how-do-you-control-a-linear-actuator-with-an-arduino#:~:text=The%20Arduino%20can%20be%20used,using%20one%20I%2FO%20pin.&text=To%20retract%20the%20actuator%2C%20the,all%20the%20pins%20to%20high.

García-Martínez, F., Roldán, F. A., Martín, Á H., & Rodrígez, M. S. (2016). "Umbrella" Artifact Caused by Air Bubbles in US Gel. Actas Dermo-Sifiliográficas (English Edition), 107(7), 603. doi:10.1016/j.adengl.2016.06.010

General Purpose US Phantom. Retrieved from https://www.cirsinc.com/products/US/zerdine-hydrogel/general-purpose-US-phantom/

Guillermic, R., Lanoy, M., Strybulevych, A., & Page, J. H. (2019). A PDMS-based broadband acoustic impedance matched material for underwater applications. *Ultrasonics*, 94, 152-157. doi:https://doi.org/10.1016/j.ultras.2018.10.002

Hartwig, V., Giovannetti, G., Vanello, N., Lombardi, M., Landini, L., & Simi, S. (2009). Biological effects and safety in magnetic resonance imaging: A review. *International Journal of Environmental Research and Public Health,* Retrieved from https://www.mdpi.com/1660-4601/6/6/1778/htm

Hedrick, W. & Hykes, D. (1989). Image and Signal Processing in Diagnostic US Imaging. *Journal of Research in Medical and Dental Science*, 5:231-239.

Hiremath, P. S., Akkasaligar, P. T., & Badiger, S. (2013). Speckle noise reduction in medical US images. Advancements and Breakthroughs in US Imaging, doi:10.5772/56519

Ilakovac, V. (2020). Statistical hypothesis testing and some pitfalls. Retrieved from https://mail.biochemia-medica.com/en/journal/19/1/10.11613/BM.2009.002/fullArticle

Image types in the toolbox. Retrieved from https://www.mathworks.com/help/images/image-types-in-the-toolbox.html

Indik, J., Gimbel, J. R., Abe, H., & Et. al. (2017). 2017 HRS expert consensus statement on magnetic resonance imaging and radiation exposure in patients with cardiovascular implantable electronic devices. *Heart Rhythm,* Retrieved from https://www.heartrhythmjournal.com/article/S1547-5271(17)30453-8/fulltext

Jiang, W., Astheimer, J. P., & Waag, R. C. (2012). Aberration compensation of an US imaging instrument with a reduced number of channels. *IEEE transactions on ultrasonics, ferroelectrics, and frequency control*, *59*(10), 2210–2225. https://doi.org/10.1109/TUFFC.2012.2447

Khoo, V. S., Dearnaley, D. P., Finnigan, D. J., Padhani, A., Tanner, S. F., & Leach, M. O. (1997). Magnetic resonance imaging (MRI): Considerations and applications in radiotherapy treatment planning. Radiotherapy and Oncology, 42(1), 1-15. doi:https://doi.org/10.1016/S0167-8140(96)01866-X

Kruskalwallis. (2021). Retrieved from https://www.mathworks.com/help/stats/kruskalwallis.html

Larsen, R. (1985). Box-and-whisker plots. Journal of Chemical Education, 62(4), 302–. https://doi.org/10.1021/ed062p302

Lee, W., & Roh, Y. (2017). Ultrasonic transducers for medical diagnostic imaging. Biomedical engineering letters, 7(2), 91–97. https://doi.org/10.1007/s13534-017-0021-8

Luewan, S., Srisupundit, K., & Tongsong, T. (2007). A comparison of sonographic image quality between the examinations using gel and olive oil, as sound media. Journal of the Medical Association of Thailand = Chotmaihet thangphaet, 90(4), 624–627.

Martin, D. R., & Semelka, R. C. (2006). Health effects of ionising radiation from diagnostic CT. *The Lancet, 367*(9524), 1712-1714. doi:10.1016/S0140-6736(06)68748-5

Morgan, M. (n.d.). Acoustic impedance: Radiology Reference Article. Retrieved September 21, 2020, from https://radiopaedia.org/articles/acoustic-impedance

NASA Langley's Technology Gateway. (2014). NASA Langley's Floating Ultrasonic Transducer for Non-destructive Evaluation Webinar. Retrieved from https://www.youtube.com/watch?v=CCOY7DDVXW0&t=1552s

Natalja. (n.d). Display Modes. Retrieved from https://sites.google.com/site/nataljasUSphysics/display-modes

Nihon Dempa Kogyo Co., LTD. Ultrasonic probe (Transducer). Retrieved from https://www.ndk.com/en/products/search/ultrasonic/.

PiezoDrive. (n.d.). Introduction to Ultrasonic Drivers. Retrieved October 19, 2020, from https://www.piezodrive.com/ultrasonic-drivers/intro-ultrasonic/

Psnr. (2020). Retrieved from https://www.mathworks.com/help/images/ref/psnr.html

Salmon, M., Salmon, C., Bissinger, A., Muller, M. M., Gebreyesus, A., Geremew, H., Wendel, S. K., Azaza, A., Salumu, M., & Benfield, N. (2015). Alternative US Gel for a Sustainable US Program: Application of Human Centered Design. PloS one, 10(8), e0134332. https://doi.org/10.1371/journal.pone.0134332

Sassaroli, E., Crake, C., Scorza, A., Kim, D. S., & Park, M. A. (2019). Image quality evaluation of US imaging systems: advanced B-modes. *Journal of applied clinical medical physics*, *20*(3), 115–124. https://doi.org/10.1002/acm2.12544

Sassaroli, E., Crake, C., Scorza, A., Kim, D. S., & Park, M. A. (2019). Image quality evaluation of US imaging systems: advanced B-modes. *Journal of applied clinical medical physics*, *20*(3), 115–124. https://doi.org/10.1002/acm2.12544

Szabo, T. (2004). Diagnostic US imaging: Inside out Elsevier Academic Press.

Szabo, T.L. and Lewin, P.A. (2013). US Transducer Selection in Clinical Imaging Practice. Journal of US in Medicine, 32: 573-582. doi:10.7863/jum.2013.32.4.573

Ter Haar G. (2011). Ultrasonic imaging: safety considerations. Interface focus, 1(4), 686–697. https://doi.org/10.1098/rsfs.2011.0029

training phantom. (). Retrieved from http://www.cirsinc.com/wp-content/uploads/2020/07/074-DS-072120.pdf

U.S. Food and Drug Administration. (2019). US Imaging. Retrieved from https://www.fda.gov/radiation-emitting-products/medical-imaging/US-imaging#benefitsrisks.

US. (n.d.). Retrieved September 21, 2020, from https://www.nibib.nih.gov/science-education/science-topics/US

Unictron Technologies Corp. (n.d.). Langevin Piezoelectric Transducer. Retrieved October 19, 2020, from https://www.unictron.com/technology/langevin-piezoelectric-transducer/

Ustuner, K. & Holley, G. (2003). US Imaging System Performance Assessment [PowerPoint Presentation]. Retrieved from https://www.aapm.org/meetings/03AM/pdf/9905-9858.pdf

VISUALSONICS. (n.d). Get High Resolution Anatomical Data with B-Mode US!. Retrieved from https://www.visualsonics.com/product/software/b-mode-imaging

Zagzebski, J. A. (1996). Essentials of US Physics. St. Louis, MO: Mosby-Year Book.

Zalameda, J. N. & Johnston, P. H. (2016). Floating ultrasonic transducer inspection system and method for nondestructive evaluation. *U.S. Patent No. 9,354,206.* Washington, DC: National Aeronautics and Space Administration.

APPENDIX

Appendix A: Gantt Chart of the Project

Project Overview Gantt Chart							
Project Title:	Ultrasound Imaging Without Topical Gel						
Students:	Mary Rego, Julisse Sabater, Kyla Egenberger, Bilguun Duulal						
Advisors:	H. Zhang (RBE/BME), Adam Lammert (BME), Robert Meislin (NYU)						

Term	Objectives	Week 1	Week 2	Week 3	Week 4	Week 5	Week 6	Week 7
A	Literature Review	■	■	■	■	■	■	■
	Project Proposal	■	■					
	Design Development			■	■	■	■	■
	Establish imaging and design parameters					■	■	■
	Establishing and purchasing prototype parts					■	■	■
	Develop A-Term Report					■	■	■
	Begin Final Report						■	■
B	Aquire Testing Materials: tansducer, actuator, materials	■	■					
	Finalize actuator information in collaboration with Dhirajsinh	■	■					
	Purchase all final actuator system components	■	■					
	Develop experimental plan	■	■					
	First data collection: gel vs. no gel on skin and phantom (baseline images)			■	■	■	■	■
	First iterations of PDMS samples			■	■	■	■	■
	Signal Processing Development			■	■	■	■	■
	Develop system design including 3D Print			■	■	■	■	■
	Second data collection: actuation with gel vs. actuation no gel (using Dhirajsinh's system)			■	■	■	■	■
	Assembly of actuator system			■	■	■	■	■
	Signal Processing: processed both sets of data and formulated qualitative and quantitative results			■	■	■	■	■
	Develop B-Term report			■	■	■	■	■
	Continue work on Final Report			■	■	■	■	■
C	Aquire any remaining materials (phantom)	■						
	Finalize experimental procedure	■	■					
	Complete IRB application	■	■	■				
	Worked on 3D print and first print of parts	■	■	■				
	Deveopment of arduino code for actuator system	■	■	■				
	Second iteration of PDMS samples with TiO2	■	■	■				
	Finalize construction of actuator system (developing code and debugging system)			■	■	■	■	■
	Second 3D print			■	■	■	■	■
	Material testing (using Dhirajsinh's actuator system)				■	■	■	■
	Finalized testing gel vs. no gel				■	■	■	■
	Signal Processing: Compare all images aquired and come to a conclusion of final image quality				■	■	■	■
	Finalize C-Term results					■	■	■
	Signal Processing Development	■	■	■	■	■	■	■
	Develop C-Term Report					■	■	■
	Continue work on the Final Report					■	■	■
D	Actuator set-up (functionality testing and load cell calibration)	■	■					
	Finalized gel vs. no gel and materials signal processing	■	■					
	Recieved IRB approval	■	■					
	Material Testing of all materials (using Dhirajsinh's actuator system)	■	■					
	Actuator system final assembly and trouble shooting		■	■				
	Lower concentration PDMS creation			■				
	Imaging of new PDMS samples			■				
	Frequency testing			■				
	Signal Processing of all data collected (material testing and frequency testing)	■	■	■	■			
	Final Report Development	■	■	■	■	■	■	
	Final Presentation Development	■	■	■	■	■	■	

Appendix B: Arduino Codes for Actuated System

Load Cell Calibration Code

```
/*
 Example using the SparkFun HX711 breakout board with a scale
 By: Nathan Seidle
 SparkFun Electronics
 Date: November 19th, 2014
 License: This code is public domain but you buy me a beer if you use this and we meet someday (Beerware license)
.

 This is the calibration sketch. Use it to determine the calibration_factor that the main example uses. It also
 outputs the zero_factor useful for projects that have a permanent mass on the scale in between power cycles.

 Setup your scale and start the sketch WITHOUT a weight on the scale
 Once readings are displayed place the weight on the scale
 Press +/- or a/z to adjust the calibration_factor until the output readings match the known weight
 Use this calibration_factor on the example sketch

 This example assumes pounds (lbs). If you prefer kilograms, change the Serial.print(" lbs"); line to kg. The
 calibration factor will be significantly different but it will be linearly related to lbs (1 lbs = 0.453592 kg).

 Your calibration factor may be very positive or very negative. It all depends on the setup of your scale system
 and the direction the sensors deflect from zero state
 This example code uses bogde's excellent library: https://github.com/bogde/HX711
 bogde's library is released under a GNU GENERAL PUBLIC LICENSE
 Arduino pin 2 -> HX711 CLK
 3 -> DOUT
 5V -> VCC
 GND -> GND

 Most any pin on the Arduino Uno will be compatible with DOUT/CLK.

 The HX711 board can be powered from 2.7V to 5V so the Arduino 5V power should be fine.

*/

#include "HX711.h"

#define DOUT  3
#define CLK   2

HX711 scale;

float calibration_factor = 280; //-7050 worked for my 440lb max scale setup

void setup() {
  Serial.begin(9600);
  Serial.println("HX711 calibration sketch");
  Serial.println("Remove all weight from scale");
  Serial.println("After readings begin, place known weight on scale");
  Serial.println("Press + or a to increase calibration factor");
  Serial.println("Press - or z to decrease calibration factor");

  scale.begin(DOUT, CLK);
  scale.set_scale();
  scale.tare(); //Reset the scale to 0

  long zero_factor = scale.read_average(); //Get a baseline reading
  Serial.print("Zero factor: "); //This can be used to remove the need to tare the scale. Useful in permanent sca
le projects.
  Serial.println(zero_factor);
}

void loop() {

  scale.set_scale(calibration_factor); //Adjust to this calibration factor

  Serial.print("Reading: ");
  Serial.print(scale.get_units(), 1);
```

```
  Serial.print(" g"); //Change this to kg and re-
adjust the calibration factor if you follow SI units like a sane person
  Serial.print(" calibration_factor: ");
  Serial.print(calibration_factor);
  Serial.println();

  if(Serial.available())
  {
    char temp = Serial.read();
    if(temp == '+' || temp == 'a')
      calibration_factor += 10;
    else if(temp == '-' || temp == 'z')
      calibration_factor -= 10;
  }
}
```

Initial Actuation Code for Experimental Testing

```
// Preprocessor for load cell

#define dout 4 \\ dout pin on the load cell
#define clk 5 \\ clk pin on the load cell

// Preprocessor for the stepper motor

#include <AccelStepper.h>  \\  library used to control acceleration/deceleration, credited to Mike McCauley

#define dirPin 2
#define stepPin 3
#define motorInterfaceType 1
#define stepsPerRevolution 1600

AccelStepper stepmotor = AccelStepper(motorInterfaceType, stepPin, dirPin);

// setup

void setup() {
  pinMode(stepPin, OUTPUT);
  pinMode(dirPin, OUTPUT);
}

void loop() {

digitalWrite(dirPin, HIGH);
for(int i = 0; i < 1*stepsPerRevolution; i++)
  {
    digitalWrite(stepPin, HIGH);
    delayMicroseconds(750); \\  longer delays means the rotations are slower
    digitalWrite(stepPin, LOW);
    delayMicroseconds(750);
  }

delay(2000); \\ delay between switching directions of rotation

digitalWrite(dirPin, LOW);
for(int i = 0; i < 1*stepsPerRevolution; i++)
  {
    digitalWrite(stepPin, HIGH);
    delayMicroseconds(750);
    digitalWrite(stepPin, LOW);
    delayMicroseconds(750);
  }
delay(2000);
}
```

Final Actuation Code for Experimental Testing

```
// Preprocessor for load cell

#include <HX711.h>

#define calibration_factor 280 // this is the calibration factor
```

```cpp
#define dout 3 // dout pin on the load cell
#define clk 2 // clk pin on the load cell
HX711 scale;


// Preprocessor for the stepper motor

#include <AccelStepper.h>

#define dirPin 4 // CW+ on stepper motor driver
#define stepPin 5 // CLK+ on stepper motor driver
#define motorInterfaceType 1
#define stepsPerRevolution 1600
#define timeDelay 100 // dont do below 130!!!

#define two_hz 10240
#define six_hz 92160
#define ten_hz 256000
#define fourteen_hz 501760
#define twenty_hz 924000

#define ten_newton 1000.00
#define five_newton 500

AccelStepper stepmotor = AccelStepper(motorInterfaceType, stepPin, dirPin);
int x = 160;

// setup

void setup() {

  Serial.begin(9600);

// init for load cell
  scale.begin(dout,clk);
  scale.set_scale(calibration_factor);
  scale.tare();

  pinMode(stepPin, OUTPUT);
  pinMode(dirPin, OUTPUT);

  stepmotor.setAcceleration(fourteen_hz);
}

void loop() {

//  Serial.print("Reading: ");
//   //scale.get_units() returns a float
//  Serial.print("grams"); //You can change this to kg but you'll need to refactor the calibration_factor
//  Serial.println();

 float forceReading;
 forceReading = scale.get_units();
 Serial.println(forceReading);
 if( forceReading < five_newton ){
    x = x + 50;
    stepmotor.moveTo(x);
    stepmotor.runToPosition();
  }

 else {
  int starttime = millis();
  int endtime = starttime;
  while ((endtime - starttime) <=300) // do this loop for up to 1000mS
  {
    stepmotor.moveTo(x-160);
    stepmotor.runToPosition();

    stepmotor.moveTo(x+160);
    stepmotor.runToPosition();
  }
}
}
```

Appendix C: Measurements of Materials for TiO₂-PDMS Samples

%Volume TiO2	Total Volume (mL)	Density TiO2 (g/mL) 4.26 Volume TiO2 (mL)	Mass TiO2 (g)	Density PDMS (g/mL) 0.982 Volume PDMS (mL)	Mass PDMS (g)	Mass Curing Agent (g)		Ratio
0%	20	0	0	20	19.6	1.0		20.0
1.00%	25	0.25	1	24.75	24.3	1.2		20.1
3.00%	25	0.75	3	24.25	23.8	1.2		20.0
5.00%	25	1.25	5	23.75	23.3	1.2		20.0
7.50%	25	1.88	8	23.13	22.7	1.1		20.0
10%	25	2.50	11	22.50	22.1	1.1		20.0
12.50%	25	3.13	13	21.88	21.5	1.1		20.0
15%	25	3.75	16	21.25	20.9	1.0		20.0
17.50%	25	4.38	19	20.63	20.3	1.0	1.1*	20.0
20.00%	25	5.00	21	20.00	19.6	1.0		20.0
22.50%	25	5.63	24	19.38	19.0	1.0		20.0
25.00%	25	6.25	27	18.75	18.4	0.9		20.0

Appendix D: Signal Processing MATLAB Codes

Image Resizing and Definition of Regions of Interest

```matlab
%% Resizing a Reference Image
%The purpose of this code is to determine the size of the images being used
%for data analysis and then resize the reference image (if it is a
%different size) so that it is the same size. This will allow for matlab to
%read all images and compare them to the reference image.

%% Reading the Reference Image and Experimental Image
% A = reference image
% B = image of interest

pic_of_interest = 'PJ_6.114.png';
ref = 'Thyroid Phantom Reference Image.png';

A = rgb2gray(imread(ref));
B = rgb2gray(imread(pic_of_interest));

%% Determining the Image Sizes

imsize_A = size(A);
imsize_B = size(B);

%this is redundant but is useful to clearly see the values
[imheight_A,imwidth_A] = size(A);
[imheight_B,imwidth_B] = size(B);

%% Resizing the Reference Image

%This resizes the reference image to the size of the experimental image
J = imresize(A,[imsize_B]);

%% Displaying The Images on One Figure For Comparison

figure;
subplot(2,2,1), imshow(J);
title('Industry Standard Thyroid Phantom');
subplot(2,2,2), imshow(B);
title('Phantom With Gel');

%% Region of interest from resized image
%This will identify the regions of the resized image that are of interest.
%This will be useful for future analysis.

% ROI Parameters
m_t = [260 325]; % ROI position, target [height width]
m_b = [350 450]; % ROI position, background [height width]
r = 65; % ROI radius

% ROI Analysis
[mu_b, sigma_b, Rb] = roimanual(J,m_b,r);
[mu_t, sigma_t, Rt] = roimanual(J,m_t,r);

% Shows the Target and Background area in relation to image
figure;
subplot(1,3,1);
imshow(J); %using the resized image
title('original');
subplot(1,3,2);
imshow(Rb);
title('background');
subplot(1,3,3);
imshow(Rt);
title('target');

% Print ROI mean and stdev
fprintf('Background ROI Mean Value:%4.3f\n',mu_b);
fprintf('Target ROI Mean Value:%4.3f\n',mu_t);
fprintf('Background ROI SD Value:%4.3f\n',sigma_b);
fprintf('Target ROI SD Value:%4.3f\n',sigma_t);
```

Vectorizer

```
%% Vectorizing code
listing = dir('./___/*png'); %input folder name into the space denoted with '___'
len = length(listing);
for i = 1:len;
    x = listing(i).name;
    im = rgb2gray(imread(x));
    b(i,:) = reshape(im,[1,size(im,1)*size(im,2)]); %variable b will now be a vectorized matrix of the
entire folder imputed
End
```

Metric Computer

```
%% Metrics Code

%Begin: load both the vectorized dataset matrix that is going to be
%analyzed and the desired reference image into the workspace

% Optimizer and Metric for Registering Images
[optimizer,metric] = imregconfig('multimodal');
optimizer.Epsilon = 5.0e-4;
optimizer.MaximumIterations = 250;
rows = b(:,1); % rows of the matrix --> input variable (in this case b) of the dataset that was used in
the 'Vectorizer' function
len = length(rows); % number of the matrix

for i = 1:len
    im1 = b(i,:); % getting vectorized images one by one --> input variable of the dataset as denoted
above
    reshaped = reshape(im1,480,640); % reshaping vectorized image
    imreshaped = uint8(reshaped); % converting it back from double to its original type uint8
    imref = rgb2gray(imread('___')); % reading reference image rgb to grayscale --> input desired reference
image into '___'(example:'06.282868.png')
    Ireg = imregister(imreshaped,imref,'rigid',optimizer,metric); % registering images

    %Calculating the Mean Squared Error
    MSE(i) = immse(Ireg,imref);

    % Calculating the peak signal to noise ratio
    peaksnr(i) = psnr(Ireg,imref);

    %Calculate the global SSIM value for the image and local SSIM values for each pixel
    ssimval(i) = ssim(Ireg,imref);
end

leng = length(MSE);
length1 = 1:leng;

%Table of all values acquired from metric computation of each image:
Tmetrics=table(length1(:),MSE(:),peaksnr(:),ssimval(:),'VariableNames',{'IM#','MSE','peaksnr','ssimval'});
disp(Tmetrics)

meanMSE = mean(MSE);
meanPSNR = mean(peaksnr);
meanSSIM = mean(ssimval);

%Calculating STD
stdMSE = std(MSE);
stdPSNR = std(peaksnr);
stdSSIM = std(ssimval);


disp('Table for Means (___):') %input dataset being processed in'___'
Tmean = table(meanMSE(:),meanPSNR(:),meanSSIM(:), 'VariableNames',{'MSE','PSNR','SSIM'});
disp(Tmean)
disp('Table for Standard Deviations (___):') %input dataset being processed in'___'
Tstd = table(stdMSE(:),stdPSNR(:),stdSSIM(:), 'VariableNames',{'MSE','PSNR','SSIM'});
disp(Tstd)
```

Hypothesis Testing: T-test and Box Plot

```
%% Hypothesis Testing
```

```matlab
% Input the two datasets that will be compared in the t-test
        %ideally the first inputted dataset (MSE, peaksnr and ssimval) would be the reference
        %second dataset (MSE2, peaksnr2 and ssimval2) would be the dataset being compared to the reference
        %note: make sure all metric datasets are within your workspace before running

[h_mse,p_mse] = ttest2(MSE,MSE2)
[h_pksnr,p_pksnr] = ttest2(peaksnr,peaksnr2)
[h_ssimval,p_ssimval] = ttest2(ssimval,ssimval2)

%Variable Definition
x1 = MSE(:);
x2 = MSE2(:);
y1 = peaksnr(:);
y2 = peaksnr2(:);
z1 = ssimval(:);
z2 = ssimval2(:);

%BOXPLOTS


%MSE PLOT
figure;
boxchart([x1,x2],'Notch','on');
xlabel({'Gel','No Gel'});
ylabel('Distribution');
title('MSE Metrics Distribution');

%PSNR PLOT
figure;
boxchart([y1,y2],'Notch','on');
xlabel({'Gel','No Gel'});
ylabel('Distribution');
title('Peak Signal to Noise Ratio (PSNR) Metrics Distribution');

%SSIM PLOT
figure;
boxchart([z1,z2],'Notch','on');
xlabel({'Gel(1)','No Gel(2)'});
ylabel('Distribution');
title('Structural Similarity Index (SSIM) Metrics Distribution');
```

Hypothesis Testing: Wilcoxon Rank-Sum

```matlab
%% Wilcoxon Rank-Sum
%   [p,h,stats] = ranksum(x,y)
% note: ranksum treats NaNs in x and y as missing values and ignores them
%computing with datasets of the first 100 images collected

% Input the two datasets that will be compared in the Wilcoxon Rank-Sum
    %ideally the first inputted dataset (MSE, peaksnr and ssimval) would be the reference
    %second dataset (MSE2, peaksnr2 and ssimval2) would be the dataset being compared to the reference
    %note: make sure all metric datasets are within your workspace before running


%calculation of p,h,stats with default 5% significance level
[p_MSE,h_MSE,stats_MSE] = ranksum(MSE_R,MSE); %_R indicates the reference dataset
[p_PSNR,h_PSNR,stats_PSNR] = ranksum(peaksnr_R,peaksnr); %_R indicates the reference dataset
[p_SSIM,h_SSIM,stats_SSIM] = ranksum(ssimval_R,ssimval); %_R indicates the reference dataset

%Tables with interpretations
    h = table(h_MSE,h_PSNR,h_SSIM, 'VariableNames',{'h_MSE','h_PSNR','h_SSIM'});
disp(h)
%true means 1 rejection of the null hypothesis at the 100 * alpha% significance level.

    p = table(p_MSE,p_PSNR,p_SSIM, 'VariableNames',{'p_MSE','p_PSNR','p_SSIM'});
disp(p)
    %ranksum computes the two-sided p-value by doubling the most significant one-sided value.

%formatting stats to put into table
a=struct2cell(stats_MSE)
b=struct2cell(stats_PSNR)
c=struct2cell(stats_SSIM)
x=[a,b,c]
```

```
STAT=cell2table(x,'VariableNames',{'MSE','PSNR','SSIM'});
disp(STAT) % the first row is the zval the second row is the ranksum

    %Test statistics, returned as a structure. The test statistics stored in stats are:
        %zval: Value of the z-statistic (computed when 'method' is 'approximate')
        %ranksum : Value of the rank sum test statistic
```

Hypothesis Testing: Kruskal Wallis

```
%% Kruskal Wallis
%load all .mat vectoried files for all datasets you
%want to compare --> in this code it is an example showing all of the
%project's mateirals that were compared

%Run this for each metric computed(mse,psnr,ssim)

%Test the null hypothesis that the sample data from each column in x comes from the same distribution.

%Input all dataset to be compared
    %note: make group one (A) the reference dataset if one is being used
A=transpose(MSE_R); %input dataset of metric to keep track ex: MSEof PDMS_1p
B=transpose(MSE_NG);
C=transpose(MSE_NEOPRENE);
D=transpose(MSE_NITRILE_RUBBER);
E=transpose(MSE_PDMS_1P);
F=transpose(MSE_PDMS_3P);
G=transpose(MSE_PDMS_5P);
H=transpose(MSE_PDMS_75P);
I=transpose(MSE_PDMS_10P);
J=transpose(MSE_PDMS_125P);
K=transpose(MSE_PDMS_15P);
L=transpose(MSE_PDMS_175P);
M=transpose(MSE_PDMS_20P);
N=transpose(MSE_PDMS_20_1_CONTROL);
    %add additional variables if necessary

x=[A,B,C,D,E,F,G,H,I,J,K,L,M,N]; %this variable should reflect all variables a inputted above
[p,tbl,stats] = kruskalwallis(x);
%will produce a kruskalwallis ANOVA table, boxplot and p value
%The returned value of p indicates that kruskalwallis either accepts or rejects the null hypothesis that
all data samples come from the same distribution at a 1% significance level.
%You can use the structure stats to perform additional followup testing. The cell array tbl contains the
same data as the graphical ANOVA table, including column and row labels.
%STOP HERE!!

%RUN THIS PORTION AFTER SAVING ALL THE ABOVE DATA PRODUCED (otherwise the multcompare graph gets produced
over
%the boxplot)
z = multcompare(stats)
%produces the multiple comparisan based on mean rank graph and the
%Zmultcompare values
```

Image Display

```
%% Displaying Four Images On One Figure
% The purpose of this code is to display all images or graphs on the same figure so that they will be
easily comparable
%% Opening And Reading The Images That Are Desired To Be Displayed
A=rgb2gray(imread('___')); %treating A as the reference image if using one (example: put 'PJ_6.114.png'
in '___')
B=rgb2gray(imread('___'));
C=rgb2gray(imread('___'));
D=rgb2gray(imread('___'));

%% Configuring and Plotting Images
[X1,map1]=imread('___'); %input image name from variable 'A' (example: put 'PJ_6.114.png' in '___')
[X2,map2]=imread('___'); %input image name from variable 'B'
[X3,map3]=imread('___'); %input image name from variable 'C'
[X4,map4]=imread('___'); %input image name from variable 'D'

figure;
%the title of each image should change based upon the displayed image
```

```
subplot(2,2,1), imshow(X1,map1);
title('Phantom With Gel 1: Reference Image'); %change '___' to be the title of what is being shown in
variable 'A'
    %Identify this image is being used as a reference depict that in the
    %title
subplot(2,2,2), imshow(X2,map2);
title('Phantom With Gel 2'); %change '___' to be the title of what is being shown in variable 'B'
subplot(2,2,3), imshow(X3,map3);
title('Phantom No Gel Increased Pressure');  %change '___' to be the title of what is being shown in
variable 'C'
subplot(2,2,4), imshow(X3,map4);
title('Phantom No Gel Normal Pressure');  %change '___' to be the title of what is being shown in variable
'D'
```

Appendix E: Non-parametric Data Distribution Example: MSE - No Gel Condition

Nonparametric Distribution No Gel Condition